Multi-Objective Torque Control of Switched Reluctance Machine

Najib Kabir Dankadai

School of Electrical and Electronic Engineering

Newcastle University

A thesis submitted for the degree of

Doctor of Philosophy

2020

Abstract

The recent growing interest in Switched Reluctance Drives (SRD) is due to the electrification of many products in industries including electric/hybrid electric vehicles, more-electric aircrafts, white-goods, and healthcare, in which the Switched Reluctance Machine (SRM) has potential prospects in satisfying the respective requirements of these applications. Its main merits are robust structure, suitability for harsh environments, fault-tolerance, low cost, and ability to operate over a wide speed range. Nevertheless, the SRM has limitations such as large torque ripple, high acoustic noise, and low torque density. This research focuses on the torque control of the SRD with the objectives of achieving zero torque error, minimal torque ripple, high reliability and robustness, and lower size, weight, and cost of implementation.

Direct Torque Control and Direct Instantaneous Torque Control are the most common methods used to obtain desired torque characteristics including optimal torque density and minimized torque ripple in SRD. However, these torque control methods, compared to conventional hysteresis current control, require the use of power devices with a higher rating of about 150% to achieve the desired superior performance. These requirements add extra cost, conduction loss, and stress on the drive's semiconductors and machine winding. To overcome these drawbacks, a simple and intuitive torque control method based on a novel adaptive quasi-sliding mode control is developed in this study. The proposed torque control approach is designed considering the findings of an investigation performed in this thesis of the existing widely used control techniques for SRD based on information flow complexity.

A test rig comprising a magnet assisted SRM driven by an asymmetric converter is constructed to validate the proposed torque control method and to compare its performance with that of direct instantaneous torque control, and current hysteresis control methods. The simulation and experimental results show that the proposed torque control reduces the torque ripple over a wide speed range without demanding a high current and/or a high switching frequency. In addition, It has been shown that the proposed method is superior to current hysteresis control method in the sensorless operation of the machine. Furthermore, the sensorless performance of the proposed method is investigated with the lower component count R-Dump converter. The simulation results have also demonstrated the excellent controller response using the standard

R-Dump converter and also with its novel version developed in this thesis that needs only one current sensor.

Acknowledgement

First, I would like to express my acknowledgement to all those who helped me throughout this research work. Sincere thanks to my first supervisor Dr Mohammed Elgendy for his technical guidance, help and support in this work, and his kind care of my study at Newcastle University. Many thanks to my second supervisor Dr Dave Atkinson for his endless guidance throughout the development and completion of my research. Special thanks to my third supervisor Dr Steve McDonald who provided me with the system model and requirements of the magnet assisted switched reluctance motor drive and guided me throughout the experimental implementation of the control system. Many thanks to all the technicians within the department especially Gordon Marshall who was always ready to assist me. Finally, I would like to say thanks to my wife and parents for their sincere support and endless encouragement during this time.

Table of Contents

List of Figures

List of Tables

List of Symbols and Abbreviations

SRM	Conventional Switched Reluctance Machine
MSSRM	Magnet Assisted Segmental Rotor Switched Reluctance Machine
AQSM	Adaptive Quasi Sliding Mode
HCC	Hysteresis Current Control
DITC	Direct Instantaneous Torque Control
SMO	Sliding Mode Observer
R, L	Phase Resistance and Inductance
Ω,θ	Speed and Rotor Position
V,i	Phase Voltage and Current
Ψ	Flux -Linkage
Θ_{on}, θ_{off},	Turn-on and turn-off angles
T	Electromagnetic torque
T_L	Load Torque
T_{ref}	Torque Reference
IF	Information Flow
$s(k)$	Sliding Variable
$U_m(k)$.	Control Signal

CHAPTER 1

INTRODUCTION

1.1 Research Background

The ever-growing market in electric machine drives in recent years is due to the trend of converting many products like vehicles, planes, manufacturing facilities, etc. to electric. Modern technology can be favoured by electrification and negative environmental factors like high carbon emission can be significantly reduced.

For the past decades, industrial applications are usually served by induction machines, permanent-magnet (PM) machines, synchronous machines, and DC machines depending on the respective requirements. However, switched reluctance machines (SRMs) are less used because of their intrinsic limitations [1, 2]. Yet, some of these applications often require of high performance, robustness to harsh environmental conditions, high reliability, vibration-free operation, and relatively affordable price [3-7]. Favourably, the switched reluctance drives inherently satisfy most of these criteria.

Generally, the investigation of switched reluctance motor based electric drives, their properties, merits, and demerits, as well as versatility of applications has been going on because of their robust structure, fault-tolerance, suitability for harsh environments, lack of rare earth magnets, low cost, and ability to operate over a wide speed range [8-11].

Although there are significant advantages of the SRMs compared to the other electric machines, their application has been relatively limited. The utilization of this machine in many industries can be significantly increased by developing solutions for the improvement of its operational efficiency to compete with highly efficient PM machines [12, 13], significant reduction of its inherent torque ripple, acoustic noise, and vibration [14, 15], creation of parsimonious control drive in terms of size, weight, and cost [16, 17]. The ultimate success in wide adoption of switched reluctance drive technology appears to be strongly attached to how effectively the above solutions are provided. Therefore, this project focuses on improving the machine's performance via a multi-objective control strategy.

1.2 Magnet-Assisted Switched Reluctance Machines

A prototype of Permanent Magnet Assisted Switched Reluctance Motor (MASRM) which produces the same torque density and efficiency as a permanent magnet motor of the same size and mass with the added advantage of SRM inherent fault-tolerance, is used in this study. This new fault tolerant, torque dense, SRM topology depicted in Figure 1.1 was designed and a

prototype machine is built, tested and verified all at Newcastle University [18], While in this study, the static tests of the MASRM were carried out to obtain the torque-flux linkage-angle waveforms and then this information is used to develop a bespoke drive controller for the regulation of the dynamic conditions of the system.

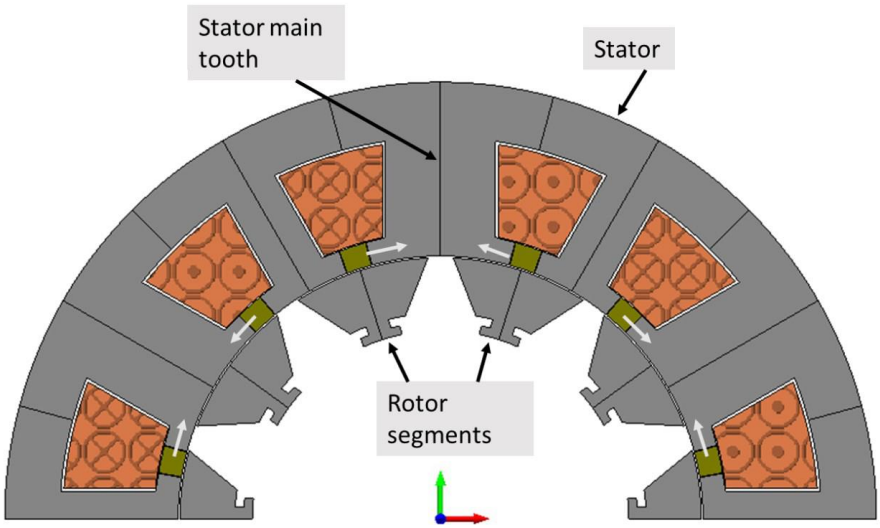

Figure 1.1: Magnet added to conventional SRM with arrows showing polarity of magnets

The operating range of a conventional SRM is limited to only the first quadrant of the B-H curve. By laying magnets at the stator slot opening of SRM extend its operation rang to the third quadrant of the B-H curve, as that is with flux from the magnets opposing the main coil flux, the operating range of the machine can be extended to third quadrant of the B-H curve shown in Figure 1.2. This process reverse magnetises the stator core material of the novel machine which results in it taking longer for the stator core to become saturated (more specifically at the aligned position where inductance is often limited by the saturation of the material). This increases the overall area between the aligned and unaligned inductance of the SRM and consequently results in greater torque generation when compared to the conventional fault tolerant switched reluctance machine.

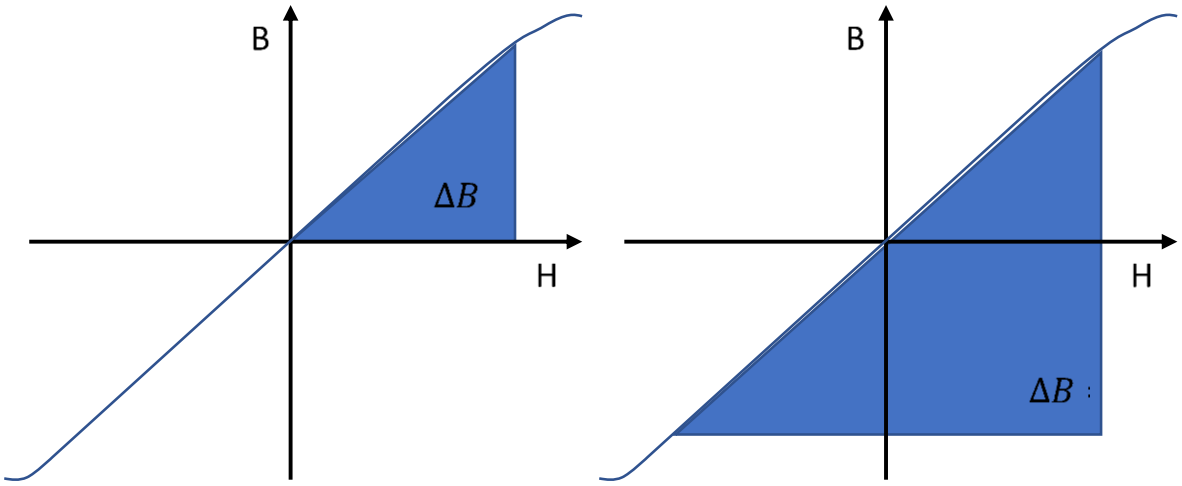

Figure.1.2: Operating range of an SRM standard SRM (left) and PM assisted SRM (right)

1.2.1 High torque density of MASRM

Torque density is generally different across ranges of electric machines subjective to the machine's size, weight, topology, cost, and control method. Most often, PM machines can inherently produce higher torque densities compared to induction machines (IMs) and SRMs due to its magnet field excitation. Nevertheless, magnet-assisted switched reluctance machines with competitive torque density are recently researched and developed. Torque density of an SRM can be significantly enhanced by adding a small quantity of magnetic materials to it while still having the unique properties of the conventional SRM [18-20]. The MASRM used in this research is created by the addition of magnets into the conventional SRM, which results in an increase in the torque density of the machine by reverse-magnetizing the stator core.

1.2.2 Fault-tolerance of MASRM

In many applications especially those with high requirement for Mean Time Between Failure (MTBF), it is importantly needed that the whole system hence the motor drive system has a low failure rate and can continue operation in case of errors/faults in phase windings, transducers and/or drive circuits. The MASRM drive can operate even if losing one or more of its phases because the phases of the machine are excited and operated independently. However, with a reduced output power rating, while other motors may completely fail in such situations [18-20].

1.2.3 High-speed operation of MASRM

MASRMs normally allow high-speed operations compared to other electric motors from a mechanical point of view, because it does not have windings in its rotor. Phase winding and/or magnets attached to the rotor of some other types of motors limits their usages in the applications that require super high-speed operations [18-20].

The inherent simplicity of the MASRM geometry with added magnets on its stator and a suitable control technique can make it offer high efficiency and a very long constant power speed ratio [18-21].

1.3 Problem Statement

One of the main drawbacks of a switched reluctance motor is its inherent large torque ripple alongside its high nonlinearity which then makes it difficult to obtain an accurate and parsimonious model, and difficult to control.

The magnet assisted SRM has steeper mid, and more saturated (flatter) align and unaligned inductance profile compared to conventional SRM because of the added magnets in its stator. Hence, it can increase the computational complexity of the modelling and control, and also increase its sensitivity to measurement errors.

Furthermore, high-performance control systems of SRMs require the use of higher number of power devices with a higher current rating of about 150% because the current demand at the aligned and unaligned rotor position is higher compared to low performance control methods like the hysteresis current control which does not demand the higher peak currents at those position. These requirements add extra complexity, implementation cost, conduction loss, and stress on the drive's semiconductors and also on the machine winding.

1.3.1 Modelling of MASRM

Usually, modelling the behaviour of MASRM depends on the prediction of its flux-linkage. Nevertheless, it is difficult to mathematically express the magnetic characteristics of a MASRM because its flux-linkage has a high nonlinear relationship with respect to both its rotor position, θ and phase current, i. The nonlinear relationship is due to the doubly salient poles of the rotor and stator as shown in Figure 1.3.

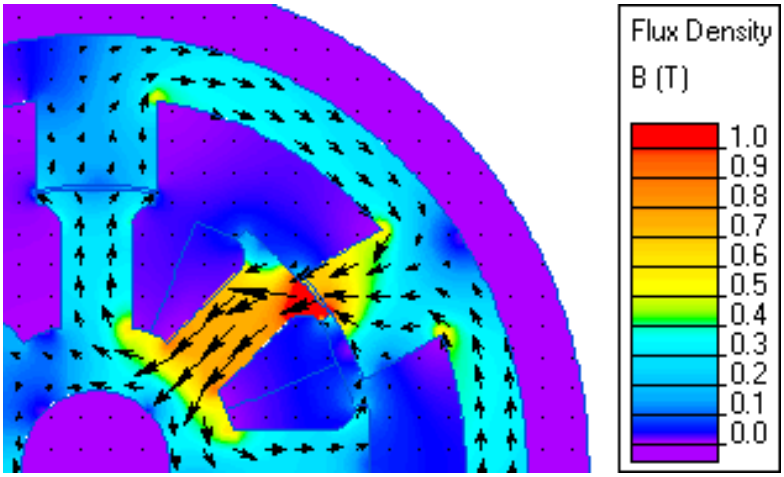

Figure 1.3: Flux-linkage characteristics of MASRM

1.3.2 Control of MASRM

Control of switched reluctance machines has been an interesting research area with diversified objectives such as speed control [22, 23], torque ripple minimization [24, 25], and/or acoustic sound reduction [26, 27]. As mentioned earlier the major disadvantage of SRM is the ripple associated with its generated torque. This triggers the investigation of different control methods.

Conventional SRM control methods such as Hysteresis Current Control (HCC) aim at producing the demanded average torque without focusing on torque ripple reduction however, some strategy in the optimization of turn-on and turn-off angles to minimize the torque ripple in HCC method is deployed in [28-30]. Torque control methods are commonly employed to reduce the torque ripple in SRMs. This includes the use of linear/non-linear Torque Sharing Functions (TSFs) with current hysteresis control [24, 31, 32]. Another popularly used torque control of SRMs is the Direct Torque Control (DTC) method which achieves good torque regulation by simultaneously controlling the rotational speed of the stator flux linkage and the estimated torque of the machine [33-36]. A simpler torque control method that has a faster response and higher robustness is the Direct Instantaneous Torque Control (DITC) [37-40]. In this method, the desired torque and the measured/estimated torque are directly compared without the need to convert it into current or considering the flux-linkage estimation error of the machine.

Also, the inductance gradient of the MASRM is inherently reduced at the aligned and unaligned rotor position. Therefore, the generated torque at these regions is low which causes torque

control techniques like the DTC and DITC methods to demand high current to track the reference torque. This means that the drive semiconductors need to be oversized which increases cost of implementation. An additional inner current control loop can be included to limit the high current demand which usually requires torque to current conversion non-linear model and current regulator for proper torque control [41, 42]. However, this significantly increases the computational burden of the control process. Furthermore, the limitations of DTC and DITC also include the dependency on switching frequency because of the hysteresis regulators involved that its performance depends on how narrow the selected hysteresis band is. Generally, hysteresis torque control methods of SRMs require a high switching frequency of 35kHz or more to keep the output torque within a good hysteresis band which increases losses and cost of implantation [37, 42, 43] compared to the conventional HCC method that commonly requires a maximum of 20kHz.

As mentioned earlier, the magnet addition in the MASRM can significantly improve its torque density and efficiency. However, it can increase the computational complexity of its control mainly because of the increased nonlinearity and sensitivity to measurement. Hence, all these added limitations increase the MASRM difficulty to be controlled using conventional methods especially those that require online computation of its nonlinear dynamic model.

1.3.3 Position estimation of MASRM

Shaft position sensors in motor drives add extra weight, space, and cost, in addition to compromising the system reliability as a potential source of failure [44-48]. Therefore, sensorless control of the MASRM drive becomes important towards the development of a superior system for several applications. However, due to the limitation with regards to computational time especially during high-speed operation of the machine, a geometry-based technique that will require minimum information of the magnetic characteristics of the machine and low computational time should be employed [48].

MASRM drives often involve the employment of several sensors like phase current sensors and phase voltage sensors for each phase and a rotor position sensor. It also involves the use of complex control algorithms that requires high processing power to achieve desired machine torque and speed characteristics. This increases design and implementation complexity making the SRM drive expensive, heavy and bulky.

In this research, a multi-objective torque control of a MASRM drive is proposed.

1.4 Research Objectives and Methodology

This project aims to optimize the torque characteristics of a switched reluctance motor drive taking into consideration multiple parameters including the reliability, robustness, size, weight, and cost of the drive. The proposed multi-objective control of the MASRM is designed taking into considerations the parameters mentioned above.

1.4.1 Research Objectives

The main objectives can be presented as follows**:**

i. To obtain a parsimonious model of the magnet-assisted switched reluctance motor drive for the controller design.

ii. To develop a torque controller with an objective function that will ensure tracking of the desired torque as accurately as possible with low ripples while considering the system's reliability, robustness, and cost of implementation without the requirement of power devices with a higher rating which is common to torque controller compared to current controllers.

iii. To develop a reliable and robust position estimation algorithm to reduce the drive's size, weight, failure rate, and cost of implementation.

iv. To simulate, analyse and compare the performance of the proposed torque control scheme with the existing torque control scheme using MATLAB/Simulink software.

v. To design and construct an experimental rig to validate the effectiveness of the proposed control method.

1.4.2 Research Methodology

In the course of achieving the set goal for the research, the methods introduced in Table I was adopted.

Table 1.1: Research Methodology

OBJECTIVE	METHOD	EQUIPMENT/ SOFTWARE
Mathematical model.	• The MASRM dynamics is obtained from measured input and output data, and prior knowledge of the system. • The chosen inputs are the phase current and rotor position while the chosen outputs are the flux and torque. • The recorded data is used to refine the model.	• Experiment rig • MATLAB/ Simulink software
Torque controller	• .A new dynamic functional torque control algorithm that regulates the torque of the machine and reduces its inherent torque ripple is developed.	• MATLAB/ Simulink software
Position estimation.	• A position estimation algorithm that can produce the rotor position of the machine from the machine's terminal measurement is develop based on a sliding mode observer.	• MATLAB/ • Simulink software
Overall proposed control scheme.	• The complete proposed control scheme is simulated under several conditions of operation using MATLAB/Simulink. .	• MATLAB/ • Simulink software
Experimental validation.	• An experimental setup for validation of the proposed control method is designed and implemented. • The control algorithm is written in C language and and implemented using a Texas Instrument DSP board.	• Experiment rig • Code Composer Studio software

1.5 Contribution to knowledge

The following contributions to knowledge are made in this research:

1. Development of a simple and intuitive dynamic functional torque control method that regulates MASRM torque and minimizes its ripple, despite the steeper mid, and more saturated align and unaligned inductance profile of the particular machine type. The proposed method can handle the limitations of SRM/MASRM torque control methods such as high switching frequency requirement, and high current demand near aligned and

unaligned rotor position, thus enabling reduction of losses and thermal stress on the power devices, their ratings, computational cost and sensitivity to measurement errors. In addition, a PWM based switching strategy is developed and used with the proposed controller instead of the conventional hysteresis switching.

2. Investigation of the reliability and complexity of several widely used control methods of SRM drives is conducted. The effect of common errors associated with a practical SRM drive on its control systems' reliability and robustness is also analysed. Furthermore, an investigation on the relationship between system complexity and reliability of SRM control based on information flow complexity within the control technique is also conducted.
3. Development and analysis of a rotor position estimation technique based on a new sliding mode observer (SMO) that is defined to only use a single current measurement and minimal inductance information of the 3-phase machine are presented, which can be employed on the traditional asymmetric half-bridge converter as well as the switch per phase converters like the R-Dump.
4. Comprehensive analysis and evaluation of the proposed torque control method with encoder-based and sensorless control modes and a detailed comparison with the most common SRM control methods.

Published work

So far, the following publication has originated from this study:

1. N. K. Dankadai, M. A. Elgendy, S. P. Mcdonald, D. J. Atkinson and G. Atkinson, "Dynamic Functional Torque Control of Magnet Assisted Switched Reluctance Motor Drives" submitted to *IEEE Transactions on Energy Conversion.*
2. N. K. Dankadai, M. A. Elgendy, S. P. Mcdonald, D. J. Atkinson and G. Atkinson, "Model-Based Sensorless Torque Control of SRM Drive Using Single Current Sensor ", accepted for publication at *the 10th International Conference on Power Electronics, Machines and Drives (PEMD),* online conference, 15-17 December, 2020.
3. N. K. Dankadai, M. A. Elgendy, S. P. Mcdonald, D. J. Atkinson and G. Atkinson, "Investigation of Reliability and Complexity of Torque Control for Switched Reluctance Drives" *IEEE International Conference on Power Electronics and Renewable Energy (CPERE 2019), Aswan, Egypt, 23-25 October, 2019.*

4. N. K. Dankadai, M. A. Elgendy, S. P. Mcdonald, D. J. Atkinson and G. Atkinson, "Assessment of Sliding Mode Observer in Control of Switched Reluctance Motors" *13th IEEE International Conference on Power Electronics and Drive Systems (PEDS 2019), Toulouse, France, 9-12 July, 2019.*.
5. N. K. Dankadai, S. P. Mcdonald, M. A. Elgendy, D. J. Atkinson, S. Ullah and G. Atkinson, "Direct Instantaneous Torque Control of Switched Reluctance Motor for Aerospace Applications," *53rd IEEE International Universities Power Engineering Conference (UPEC 2018), 1-6, Glasgow, Scotland, 4-7 September 2018.*.

1.6 Thesis Structure

This thesis is organized as follows; The background, problem statement, methodology, and objectives of the research are introduced in Chapter 1. Chapter 2 presents a literature review of related work published in respect of the research. Chapter 3 presents a description of the proposed system including the MASRM, its power converter, and control development with its implementation strategy. Investigation of the reliability and the complexity together with the relationship between both them is presented in Chapter 4, for different torque control methods and a comparison is presented to show the superiority of the proposed control. In Chapter 5 the reference torque tracking and torque-ripple minimization of MASRM by the proposed dynamic functional control method are presented. A new position estimation technique for the MASRM drive based on a sliding mode observer is developed and analyzed in Chapter 6. In Chapter 5, the experimental test rig for the validation of the proposed methods for this research is described and the relevant experimental results are presented and compared. Finally, general conclusions and future work for the research are presented in Chapter 7.

CHAPTER 2

SWITCHED RELUCTANCE MACHINE DRIVES

Switched reluctance machines are gaining popularity in electric drive applications due to its robust structure, fault-tolerance, suitability for harsh environments, lack of rare earth magnets, low cost, and ability to operate over a wide speed range [8-11]. These applications include Electric Vehicle (EV)/Hybrid Electric Vehicle (HEV), more-electric aircraft, white-goods, wind generators, pumps, spindles, superchargers and energy storages. However, the SRM suffers from large torque ripple caused by saturation, nonlinear torque characteristics, and current commutation. It also has lower torque density compared to permanent magnet machines, and it suffers from high acoustic noise due to the inhomogeneous radial flux density distribution in the airgap and the torque generation mechanics. Several studies have focussed on improving the machine design and control to optimize its torque characteristics which were discussed in this project [15, 49].

As discussed in Chapter1, the objectives of this study are focused on modelling, torque control and torque-ripple minimization of the SRM/MASRM with encoder-based and sensorless operation. Several research activities have been done in these fields and the relevant literature reviews presents in this chapter. Following the aims and objectives of this study are discussed in Chapter 1, system modelling, converter topologies, torque ripple minimization, acoustic noise minimization, torque density optimization, and sensorless control of SRM will be discussed.

2.1 Modelling of SRM

Similar to the other research project in the area of drives and control, to test a new SRM drive control system, a simulation model of the system is usually required to be developed, tuned, tested, and analysed. Successful operation of the simulated system minimises the risks associated with the physical implementation of the drive system, especially when a model-based control method is used. Accurate modelling of an SRM drive system is complex because of the machine nonlinearities which are due to its high magnetic saturation during operation and its doubly salient structure [50-52].

Generally, models of electric machines can be evaluated by their accuracy and computational time. The accuracy depends on how similar the predicted behaviours of an electric machine's model is to the actual behaviour of the machine under same operating conditions, while the computational time is scaled by the time the model takes to predict output(s) of the machine behaviour based on a given input(s). Therefore, a compromise between the accuracy and

computational speed of a model should be considered for the design and selection of the appropriate model based on available resources and applications in view. Usually, modelling of SRM machines only emphasizes on capturing the electromagnetic and mechanical behaviour of the machine without a comprehensive inclusion of other physical fields, such as the temperature, to minimise computational cost. This is because the electromagnetic behaviour of an SRM drive is the foundation for optimization and control of its most important parameters including its average torque, torque ripple, acoustic noise, and efficiency.

Usually, modelling the behaviour of SRM depends on the prediction of its flux-linkage which is often obtained by (2.1) given below:

$$v = iR + \frac{d\psi}{dt} \tag{2.1}$$

where v is the applied phase voltage, R is the winding resistance per phase, t is the time and ψ is the flux-linkage due to the phase current and rotor angular-position.

However, it is more difficult to mathematically express the magnetic characteristics of an SRM compared to other traditional electric machines, since its flux-linkage has a high nonlinear relationship with respect to both its rotor position, θ and phase current, i. Figure 1.2 in chapter 1 shows the flux-linkage distribution in an SRM. The nonlinear relationship between the flux-linkage and the rotor position is due to the doubly salient poles of the rotor and stator, which causes a variation of flux paths in the airgap as the gap is unequally distributed in the peripheral direction with the rotor position. While the nonlinear relationship between the flux-linkage and the phase current is due to the requirement of the SRM to operate in the magnetic saturation region to achieve a high torque density, causing flux-linkage nonlinearity with respect to the phase current. Therefore, (2.1) is often expanded as a first-order nonlinear differential equation in (2.2) or (2.3) as follows:

$$v = iR + \frac{\partial\psi(\theta,i)}{\partial i}\frac{di}{dt} + \frac{\partial\psi(\theta,i)}{\partial\theta}\frac{d\theta}{dt} \tag{2.2}$$

$$v = iR + L(\theta,i)\frac{di}{dt} + \frac{d\psi(\theta,i)}{d\theta}\ \omega_m \tag{2.3}$$

where L is the inductance and, ω_m is the angular speed.

Studies on curve fitting method of modelling techniques of the electromagnetic characteristics of SRM have been presented based on experimental data, Finite Element Analysis (FEA) [18, 53-57] and Boundary Element Method (BEM) [14, 58-61]. This study considered the curve fitting modelling method as they achieve a good balance between model accuracy and model complexity [49], which is in line with the research objectives of this study.

Curve fitting methods of modelling an SRM approximate the change of the flux-linkage or inductance profile with the change of both phase current and rotor position into analytical functions using a limited set of data acquired from Finite Element Analysis (FEA), Boundary Element Method (BEM), or Experimental method. These methods are briefly discussed below.

Generally, the main merit of curve-fitting methods for modelling an SRM is that they can approximate its flux-linkage characteristics only based on a few set of data which can be collected either from experiments, BEM or FEAs hence, it provides a reduced computational cost compared to numerical methods which require a full set of data. On the other hand, the main limitations of curve-fitting methods for modelling an SRM include: they are often heuristic and factual, they fit the curves of flux-linkage or inductance of a particular SRM; they still need a set of data obtained from experiments or FEAs.

FEA is the most popular tool for obtaining modelling data for SRMs since it can provide highly accurate electromagnetic characteristics for different machine topologies without the constraints normally imposed by other methods. The FEA analyses a system solution by subdividing its entire domain into smaller and simpler parts known as the finite elements. Then it assembles back the derived equations associated with each finite element into a larger system of algebraic equations. This process allows the FEA to generate approximated values of the unknown parameters at a discrete number of points over the domain [14]. The main advantages of the use of FEA to generate SRM characteristics data include: firstly, the FEA can be applied in analysis of any irregular or complex SRM geometry because the allocation of the finite elements is flexible and covers the overall solution domain. Secondly, the FEA can apply iterative algorithms to generate a highly accurate solution of the magnetic field distribution in the subdomains with nonuniform properties, like the laminated core which often have nonlinear permeability. Thirdly, the FEA can provide faster solution algorithms and permit reduced memory requirement because its system matrix is generally symmetric, thinly dispersed, and diagonal [56, 62, 63]. The main disadvantages of the FEA to generate an SRM characteristics

data include: Firstly, the high computational workload is normally involved to achieve high accuracy of field solution in performing FEAs because the number of elements in the simulations can be significantly large which requires the inversion of a large system matrix. Secondly, the predefined mesh in FEA cannot be considerably modified as the SRM geometry changes because remeshing the solution domain is required for each design. Thirdly, it is required to volume-mesh the entire solution domain when FEA is used for optimization-based design which generally leads to high computational cost, most noticeable when the volume-meshing is applied to machine parts with small dimensions like the airgap region of the SRM which leads to a large number of high-resolution elements, thus demands a substantial refinement of the mesh [49].

BEM is another analysis method, which is gaining interest in the field of electromagnetic analysis of electric machines, that can provide characteristics data of the SRM. It uses a different approach compared to the FEA as it creates a boundary value problem as integral equations with the boundary conditions approximated by simple functions. This is unlike the FEA in which the differential equations with the unknowns parameters are solved across the whole space, and then the integral equations are used to calculate the solution at each point in the solution domain [59]. The main advantage of the BEM over the FEA is its reduced complexity and computational cost because it only requires a surface mesh along with the limits (boundaries) and a volume mesh defined over the whole space, which decreases the dimension of the system matrix as the complexity of meshing the structures like the airgap is reduced. The main disadvantages of the BEM over the FEA is its compacted, asymmetry and non-diagonal dominance in the system matrix [49]. In addition, the lack of diligent consideration of the effect of inhomogeneous properties of material like the nonlinear permeability of stator/rotor steel limits the application BEM in analysis of SRM [60].

In the experimental method, the SRM characteristics data are obtained by energising the machine while recording the needed data at several rotor positions. Commonly, the phase current, the phase flux-linkage, and the phase torque of the machine are recorded by locking the rotor at several angular positions. The main merits of the experimental methods that make it attractive over the FEA and BEM are it does not require several simplified assumptions such as not taking hysteresis saturation, manufacture error, and end effect into consideration. [64, 65].

These analytical functions (models) that can be obtained from the curve fitting of the SRM characteristics data can be represented in the form of an intelligent models, interpolation models or closed-form model as discussed in the subsections below.

2.1.1 Intelligent Models

In intelligent methods of modelling SRM such as an artificial neural network (ANN), the parameters of the derived models that characterise the nonlinear properties of the flux-linkage or inductance of the machine are calculated by training many measured magnetic data obtained from numerical methods or experiments [49]. The accuracy of an intelligent SRM model is strongly related to the size of the data obtained for approximating the model coefficients and the structure type of the model as the number of the neurons in the hidden layer of an ANN [64]. Cao et al proposed a flux-linkage model in a 2-D plane for a planar SRM. The model based on a cascade-forward backpropagation neural network (CFNN) with a sample set obtained from experimental which were divided for training, model validation, and assessment of the generalization performance. The developed CFNN consists of one input layer, two hidden layers, and one output layer which have a maximum relative error of 11.05% and the mean relative error of 0.42% based on the results presented [50]. In [66] an improved generalized regression neural network (GRNN) optimized by a fruit fly optimization algorithm (FOA) is utilised for prediction of the electromagnetic characteristics of SRM. The numerical method was employed to obtain the set of data for training and verification of the FOA-GRNN method. In addition, a comparison of the proposed FOA-GRNN was done with intelligent methods of modelling including; Radial Basis Function Neural Network Back Propagation Neural Network (BPNN); Extreme Learning Machine to validate its superiority. Li et al described a general flux-linkage model for SRMs in [67], which was created by normalising the magnetic structures and magnetic saturation levels of the machine. The flux-linkage nonlinear behaviour of the SRM calculated with data points only at the aligned and unaligned rotor positions. Furthermore, a radial basis function neural network is employed to increase the accuracy of the modelling method. The flux-linkage characteristics of five prototype SRMs were modelled using the proposed methods and each was validated using the FEA method. In [68], a combined modelling method for SRM is presented. The modelling method involved training support vector machine with obtained few samples, and BPNN is used to describe the reconstructed flux-linkage and static torque characteristics.

2.1.2 Interpolation Models

The interpolation models are created by using appropriate piecewise interpolation functions based on the stored magnetic characteristics data of the SRM data to approximate its nonlinear flux linkage or phase inductance. In [69] and [70], Xue et al. presented a 2-D bicubic spline interpolation function and bilinear interpolation-based models to express the nonlinear magnetic characteristics in SRMs. In [71] and [72], a quadratic interpolation technique was employed to interpolate the flux-linkage of SRM with respect to the phase current and rotor position.

2.1.3 Closed-Form Model

A Fourier-series based model is a typical type of closed-form models used to characterise the nonlinear behaviour of SRM flux-linkage or inductance In [73], Shen et al. presented a fast measurement technique of flux-linkages profile. The dc voltage and phase current waveform of an SRM are recorded at the aligned, unaligned, and mid-aligned rotor position to created three flux-linkage curves, and then the curves are used to calculate the coefficients of second-order Fourier series flux-linkage based model. Song et al. proposed a decoupled analytical modelling method of SRM based on similar second-order Fourier series to calculate its electromagnetic behaviour, including flux-linkage and static torque characteristics. Coefficients of the Fourier series were determined from 21 measured data points from five rotor positions to improve model accuracy [74]. Khalil et al created an invertible flux-linkages SRM model based on Fourier series by expressing the coefficients of the Fourier series as flexible terms which were set in terms of machine geometry-dependent flux-linkage at the unaligned and aligned position [75]. Hence, the availability of the inverse models makes the proposed model suitable for real-time implementation. In [76], Chi et al. proposed a simple flux-linkage based analytical model of SRM was developed using Fourier series with few data points (only five data points) which were obtained from FEA. The position dependence of the flux-linkages was expressed as a small number of Fourier series terms while the phase current dependence of the flux-linkage was expressed as an arc-tangent function.

In summary, developing an accurate and parsimonious model of SRM drives is the basis in the design and implementation of the electric drive, and the model type selection depends on the intended application and available resources. Therefore, the Fourier-series based model is selected amongst the other stated methods above to characterise the nonlinear behaviour of the

MASRM inductance because of its ability of simple implementation with less compromise to accuracy. , This modelling is further analysed and described in chapter 3 and chapter 6.

2.2 SRM Drive

In this section, the required considerations in the design and control techniques of SRM drives to achieve optimal performances are described. The main performance parameters include high torque density and efficiency, and low torque ripple and acoustic noise.

2.2.1 SRM Power Converter

An SRM drive requires a power converter with non-conventional topologies because of its unique structure and principle of operation. This is unlike the three-legged converter widely used for electric machines with the same rotating airgap and sinusoidal phase currents. With SRM, a significant DC link voltage fluctuation occurs during the operation of the drive because a large amount of magnetically stored energy is exchanged back and forth between the phase windings of the SRM and the DC Link. Hence, a large DC-Link capacitor which acts as a power balancing buffer is often employed to suppress this fluctuation [77]. Nevertheless, the cost, size, and thermal management of the capacitor is also a limitation of the converters for SRM drives.

The SRM converter topologies are often characterised based on the number of power switches per machine phase. A comparative analyses of several topologies with the different merits and demerits are presented in [78] [79], including the most popular Asymmetric Half-Bridge Converter, the Full-Bridge Synchronous Converter, the Buck-Boost Converter, the C-dump Converter, the R-dump Converter, the Auxiliary Communication Winding Converter, the Quasi Z-Source Converter, the Variable Voltage Converter, and the Integrated Multilevel Converter. These mentioned converters are discussed below.

2.2.1.1 Asymmetric Half-Bridge Converter

An Asymmetrical Half-Bridge Converter (AHBC) is the most commonly employed converter topology for SRM drive because of its advantages mentioned below. It uses 2 switches and two diodes per phase connected to the DC link voltage which is usually provided by a single rectifier or DC power supply as shown in Figure 2.1. The phase voltage of each phase in AHBC is determined in accordance with the functionality of its operational mode which are on-state,

freewheeling-state, and off- state. When the phase current is to be increased, both power switches of the active phase are on (on-state), while both power switches are turned off (off state) happens when the phase current is to be reduced. Furthermore, one power switch is turned on and the other turned off (freewheeling state) for zero current change mode. Figure 2.1 (a)-(c) shows the different switching states of the AHBC.

The main advantages of the AHBC topology include:

- Its ability to independently control the upper and lower switched hence, providing higher drive control flexibility.
- Its capability of having freewheeling mode of operation can allow maximum regenerative braking.
- It has the same mode of operation (performance) during the magnetization and demagnetization process.

The main disadvantages of the AHBC topology include:

- The AHBC has high power devices count per machine phase.
- The on-voltage drop of the two power devices is often significant which can limit low voltage application.
- Its demagnetization speed is reduced at high speeds due to its required fixed voltage supply which is limited by back EMF.
- It needs a large DC-Link capacitor to smooth the voltage ripple related to the magnetization and demagnetization of the machine phase windings.
- A significant power loss during demagnetization in generator mode can occur because of the large voltage drop across the AHBC freewheeling diodes.

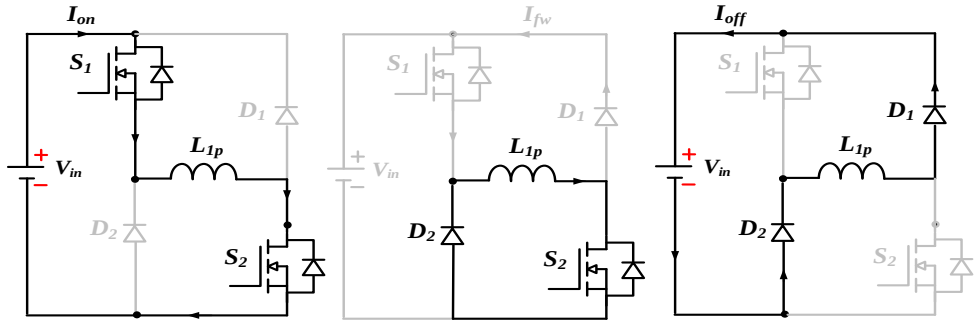

(a) On state (b) Freewheeling state (c) Off state

Figure 2.1: Circuit Diagram of Asymmetric Half-Bridge Converter

2.2.1.2 Full-Bridge Synchronous Converter

The Full-Bridge Synchronous Converter (FBSC) topology is a modification of the asymmetric half-bridge converter by replacing the freewheeling diodes with power switches as depicted in Figure 2.2 improved operational efficiency during demagnetization and freewheeling modes of operations. Its principle of operations is very similar to that of the AHBC.

The main advantages of the FBSC topology include:

- It offers very high flexibility in controlling SRM operations.
- It reduces the conversion losses during demagnetization and the freewheeling mode of operations.

The main disadvantage of the FBSC topology is:

- It has high counts of power switches per phase which increases the cost of the converter whiles the additional switches are underutilised.

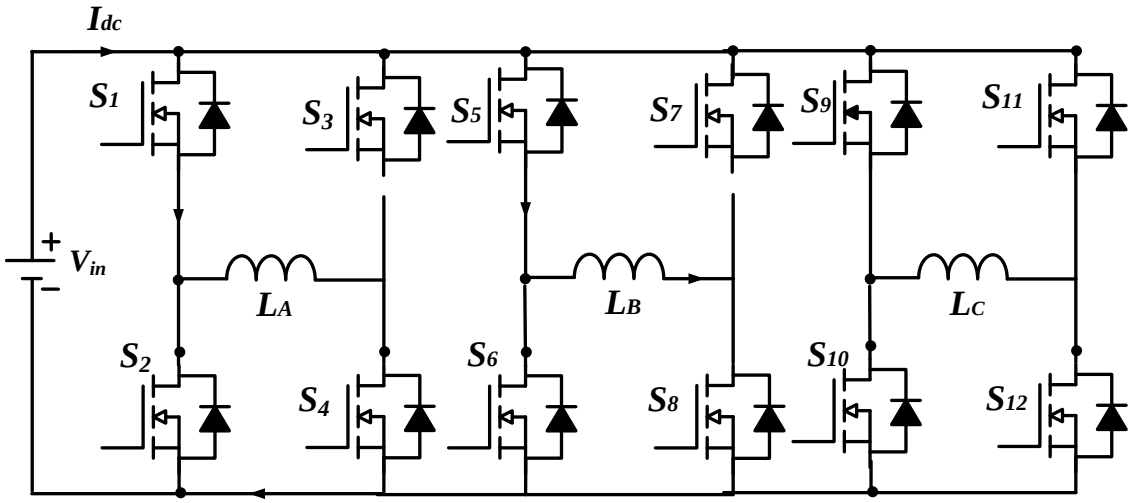

Figure 2.2: Circuit Diagram of Full-Bridge Synchronous Converter

2.2.1.3 Buck-Boost Converter

Buck-Boost Converter for SRM is normally designed to have its output DC voltage to be greater than the input DC voltage. The circuit diagram for the Buck-boost converter for SRM is shown in Figure 2.3 (a) and its four modes of operations are shown in Figure 2.3 (b-e). The switch Q_a, the diode D_a, the inductor L_a, and the output capacitor C_b form the front stage of the converter**.** The dual-rail voltage boosting configuration provides an added control flexibility of

the SRM drive as the magnetization and demagnetization voltage are separated hence, providing a variable supply voltage to the machine winding.

The main advantages of the buck-boost converter include:

- It allows the input voltage to each phase to be greater than the DC supply voltage hence accelerating current build-up, which enables faster demagnetization during motoring operation.
- Each phase can be controlled independently despite its one switch per phase configuration.

The main disadvantages of the buck-boost converter include:

- Added circuitry which increases the complexity of the converter,
- The power devices require a higher voltage rating because the voltage across Q_a is the sum of V_{cs} and V_{cb}.

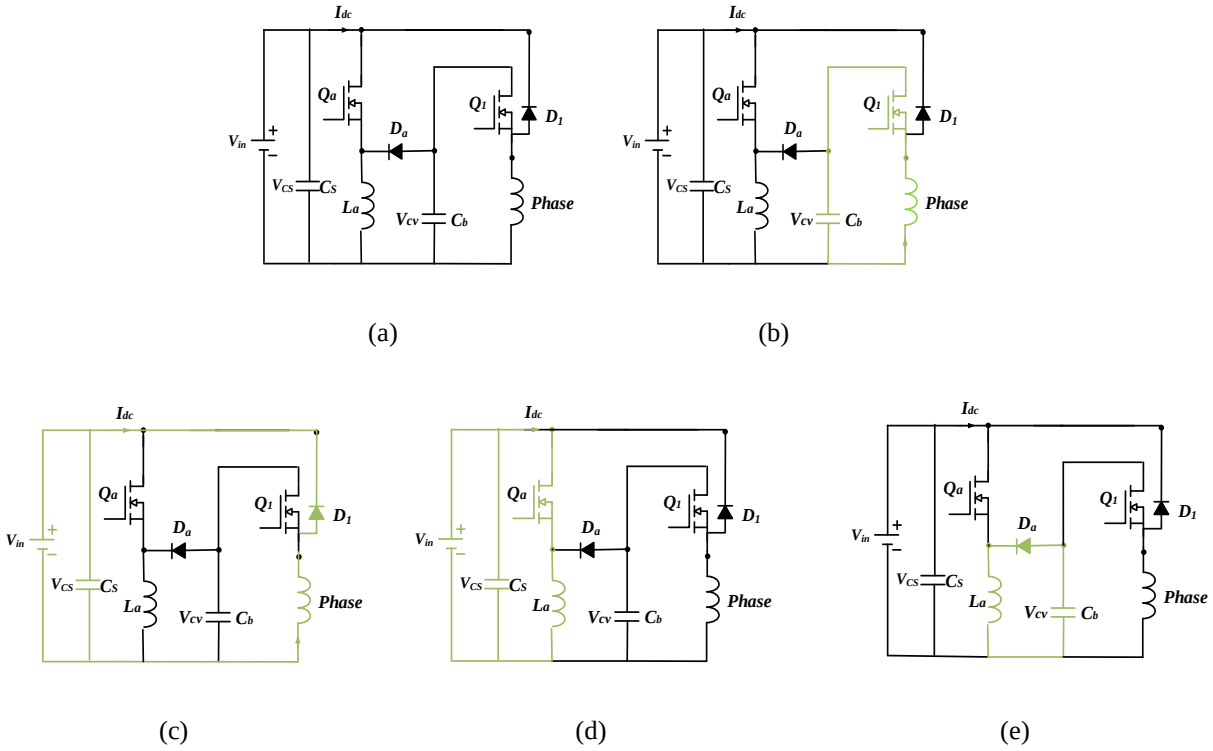

Figure 2.3: Circuit diagram of Buck-Boost Converter (a)static view of the circuit (b) magnetization operation (c) demagnetization operation (d) charging Cb with Qa turned on (e) charging Cb with Qa turned off.

2.2.1.4 Active Boost Converter

An active boost power converter with a variable voltage gain for SRM is proposed in [80] based on an improved buck-boost converter. It has a simple configuration with one power switch and one diode per phase. It provides real-time control of the SRM drive demagnetization voltage which is achieved using demagnetization energy and a power switch. The modes of operation of the proposed converter are shown in Figure 2.4.

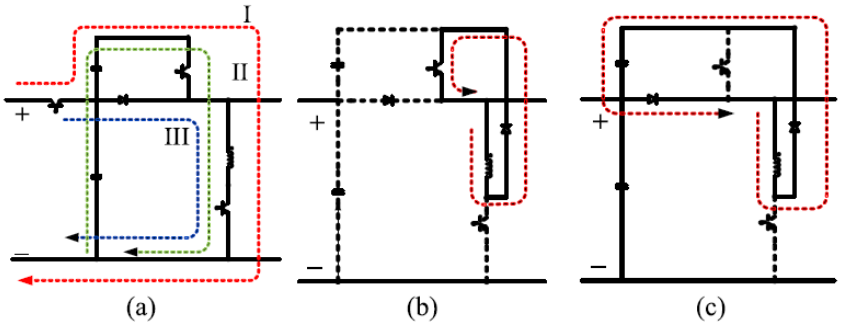

Figure 2.4. Operation modes of the Active Boost Converter (a) Excitation mode (b) Freewheeling mode (c) Demagnetization mode [62].

The main advantages of the active boost converter include:

- It can adjust the demagnetization voltage of SRMs with high flexibility to effectively increase control performance, especially during demagnetization.
- It has a simple structure and low cost

The main disadvantage of the active boost converter is:

- It has added control algorithm complexity because the voltage across an auxiliary capacitor need to be precisely controlled

2.2.1.5 Auxiliary Commutation Winding Converter

As the converter name implies, its topology requires the SRM to include an auxiliary winding. The configuration of this converter has four modes of operations including magnetization and freewheeling of the SRM main winding; demagnetization of the SRM main winding to the auxiliary winding and demagnetization of the surplus energy in the main winding to the energy

supply. Figure 2.5 shows the circuit diagram of the converter. The 2 dots in the figure shows the position where the main winding and the auxiliary winding are aligned.

The main advantages of this configuration are:

- The performance of the system is improved because the system can recover the magnetic energy in the auxiliary winding.
- The stored magnetic energy of the auxiliary winding is utilised to rapidly build-up phase current.
- A soft-switching mode can be employed with this topology.

The main disadvantage of this topology is:

- It has an additional cost of the extra auxiliary winding.

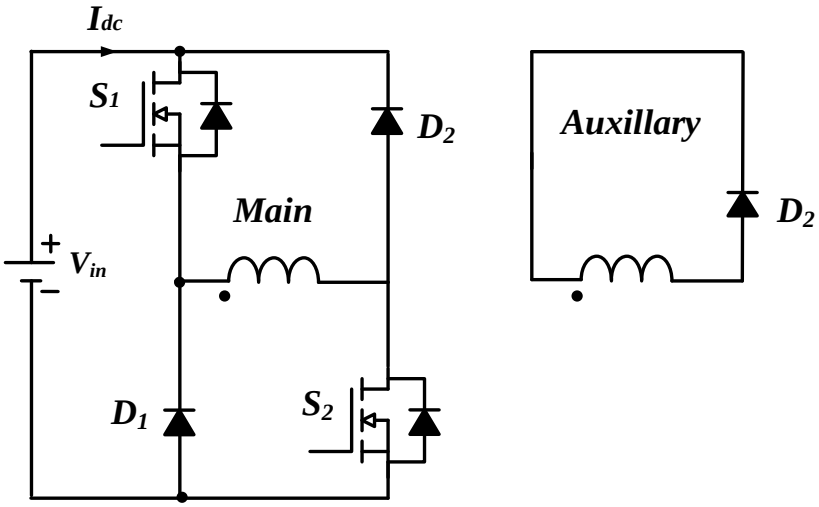

Figure 2.5: Circuit Diagram Integrated Multilevel Converter

2.2.1.6 Integrated Multilevel Converter

An Integrated Multilevel Converter (IMC) for an SRM has a topology with an added modular front-end circuit to the popular AHBC, consisting of switches and diodes as shown in Figure 2.4. The multimode enables the achievement of multilevel voltages through controlling the switching state of the power switches in the front-end module [81].

The main advantages of this configuration are:

- It has rapid magnetization and demagnetization compared to conventional converters.

- It can reduce torque ripple and improve efficiency in SRM drive because of multilevel voltages because of its increases degree of freedom that enables better flexibility in controlling the drive.

The main disadvantages of this configuration are:

- It has added cost of implementation because of the added power devices.
- Its control algorithm also has added complexity because of the added module.

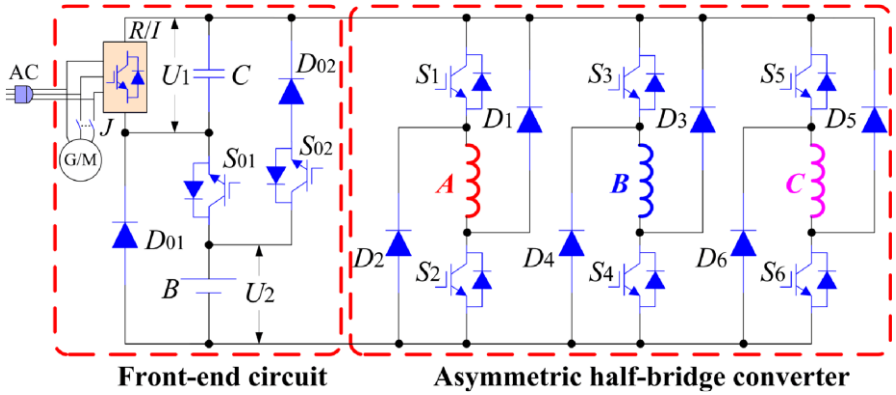

Figure 2.4. Circuit Diagram Integrated Multilevel Converter [63]

2.2.1.7 C-Dump Converter

The C-Dump converter for SRM is a typical (*number of phases* + 1)- switch converter topology [82, 83]. If the chosen control variable rises above the reference setpoint of the controller, the switch S_1 is turned off allowing the diode D_1 to be forward biased, hence the control variable decreases such that the magnetic energy stored in the phase winding is charging the capacitor *C*, then moved to the power supply through the switch *S* (Figure 2.5).

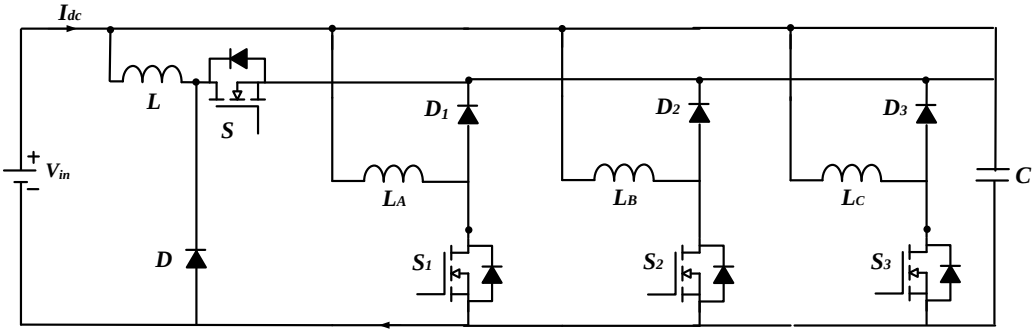

Figure 2.5: Circuit Diagram of C-Dump Converter:

The main advantage of the C-Dump topology is:

- It has a minimum power device count per phase while allowing independent control for each phase.

The main disadvantage of the C-Dump topology is:

- Its current commutation can be slow because the negative voltage across the phase winding is constrained by the difference between the supply voltage and the voltage across the capacitor C.

2.2.1.8 R-Dump Converter

The R-Dump converter for SRM is a one switch, one diode per phase converter with passive components *R* and *C* added to the topology [82, 83]. The operating principle of the R-dump converter is like that of the AHBC as described in Figure 2.6 except during the demagnetization process. Considering phase one, if the control variable (current/torque) increases rises above the reference value, the switch S_1 will be turned off. Furthermore, the control variable is decreased by freewheeling through the diode D_1 such that the magnetic energy stored in the phase winding is charging the capacitor *C* to the DC supply voltage and dissipating in the resistor *R*.

The main advantage of the R-Dump configuration is:

- It has a low power device count per phase which reduces its cost of implementation.

The main disadvantages of the R-Dump configuration are:

- It suffers from reduced power efficiency and control flexibility because it has only two modes of operation.
- The selection of *R* is strongly related to the performance of the converter.

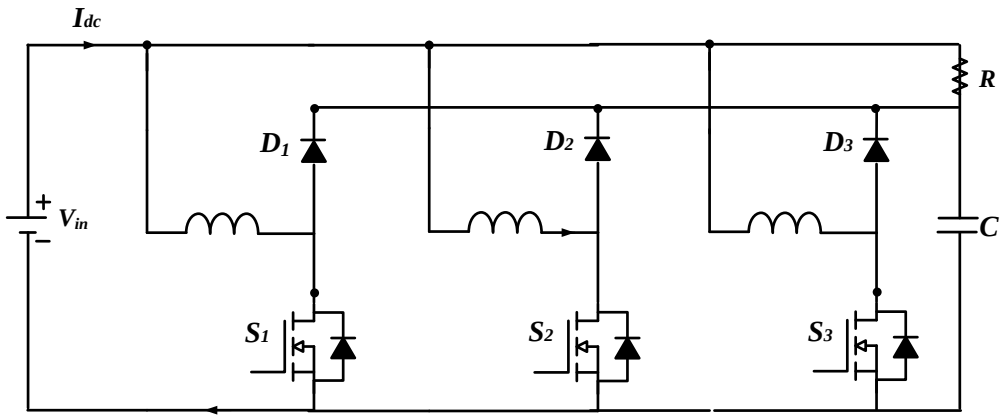

Figure 2.6: Circuit Diagram of R-Dump Converter:

2.2.2 Torque ripple of SRM

As mentioned earlier, the SRM drive is becoming attractive for many applications because of its potential prospect. However, it generally suffers from larger torque ripple compared to the other AC machines and DC machines because of its doubly salient structure, that leads to nonlinear discrete torque production. The torque ripple of the SRM is often caused by saturation, nonlinear torque characteristics, and current commutation [31, 84-87]. The static torque–current–rotor position characteristic profile of an SRM and the phase current waveform of each phase determine the characteristics of its torque during dynamic operation. The high torque ripple drawback of the SRM can be reduced through machine design methods and/or control strategy approaches [15].

Optimizing the geometry of the SRM can have a significant effect on its torque characteristics such as the generated torque density, torque ripple, and vibration. The torque ripple reduction can be realized by choosing an appropriate number of rotor and stator poles and their respective diameters, stack length, and pole arcs/shapes. The optimization of arc angle for rotor and stator pole to minimize the torque ripple of SRM using FEA and neural networks with generalised radial function has been presented in [88]. It involves analysis to establish the relationship between the output torque profile and machine parameters to mainly optimize the rotor and stator pole arc angles for torque ripple minimization. Another torque ripple reduction by optimizing the selection of the rotor/stator pole arcs using progressive quadratic response surface technique in addition to the optimization of the turn-ON/OFF angles in a current controller is achieved in [89]. In [90], a similar approach to the one in [88] is used where a neural network and Lagrange multipliers are employed to model the torque ripple of SRM. The

proposed method enabled the conversion of the constrained optimization problem (the cost function) to an unconstrained problem. The torque ripple of the machine is then minimized through optimizing the tooth width and pitches of its rotor and stator. Another method of employing special geometry in the SRM is the application of notch in its rotor teeth. A notch is applied in the forward rotating direction of the rotor teeth of SRM in [91] and in all rotor teeth [92], all to reduce the generated torque ripple. Moreover, attachment of a pole shoe to the lateral face of the rotor pole of SRM is presented in [93] to minimise torque ripple. Also, a non-uniform air gap structure of an SRM is proposed for torque ripple minimization in [94].

Another way of reducing torque ripple in SRM from its structural development is the Motor topology. Torque ripple can be reduced by employing a large number of rotor poles to flatten the dips in the produced resultant torque, however, with a forfeit in the ratio between the minimum and maximum unsaturated inductances [95, 96].

Conventional SRM control methods like Current Chopping Control (CCC) target at producing the needed average torque without aiming at torque ripple reduction. Many control techniques have been suggested to reduce torque ripple of the SRM. Among the generally used techniques is current profiling, which includes modulation of individual phase currents with predefined profiles. Though this procedure needs more than a few iterations to realize optimal current shapes to decrease the torque ripple subject to the required performance and it often requires a large memory to store the current waveforms [97, 98]. Another common strategy is the optimization of turn-on and turn-off angles to minimise the torque ripple, but the performance of this technique reduces with speed increase, as the advancement angle becomes confined by the limited ability to get the current in and out of the phases [28, 30].

Numerous torque control techniques for the SRM have also been proposed to reduce its torque ripple. These involve the use of linear/non-linear Torque Sharing Functions (TSFs) with current or torque hysteresis control [24, 31, 32]. The torque-current relationship of the SRM is crucial in such approaches to determine the reference for the hysteresis controller. The Direct Torque Control (DTC) technique can achieve good torque regulation by concurrently controlling the rotational speed of the stator flux-linkage and the projected torque of the machine. Nonetheless, the process requires complicated calculations with multiple parameters [33-36]. On the other hand, a simpler torque control scheme that has a faster response and higher robustness known as the Direct Instantaneous Torque Control (DITC) is developed based on the DTC [37-40]. In

this torque control method, the desired torque and the measured phase torque of the SRM are directly compared without the need to convert it into current and the flux-linkage control loop is also not needed. The switching signals in this method are normally generated from a torque hysteresis regulator. Generally, the inductance gradient of SRM is inherently reduced at the aligned and unaligned rotor position. Thus, the produced torque at these regions is low which causes the DTC and DITC methods to demand high current within the regions in order to trace the demanded torque. This necessitates that the drive power devices need to be oversized which increases system cost of implementation. Additionally, the shortcomings of DTC and DITC also include the dependency of its performance on switching frequency. Commonly, hysteresis torque control techniques of SRMs require a high switching frequency of 35kHz or more to keep the output torque within a narrow hysteresis band which increases losses and cost of implantation [37, 42, 43].

2.2.3 Acoustic Noise of SRM

High acoustic noise is also part of the main disadvantages that have restricted the extensive application of SRMs compared to other electric machines, especially in noise-sensitive applications. The noise produced in SRM drive is mainly because of the radial vibrations of the stator which is linked to the inhomogeneous radial flux density distribution in the airgap and the torque generation mechanics [99, 100].

The torque of the SRM is produced from the phase current applied to machine phase windings. As the current is applied, the rotor of the SRM is pulled towards the aligned position with the minimum reluctance generating a substantial radial force that acts upon the stator. However, another force in addition to the tangential torque force which is a radial force pushes the stator along the axis of any excited stator pole(s). this radial force causes the stator to resonate (vibrate) with a damped and subsequently produce acoustic energy (acoustic noise) [101]. Machine topology design [102-110] and control techniques [27, 111-120] are the main approach employed to reduce the acoustic noise of the SRM. Nevertheless, a detailed review of this method is beyond the scope of this study.

2.2.4 Windage Loss of SRM

Generally, losses in SRM drives consist of power electronics loses, winding loses, windage loses and core loses. Characteristics of the materials used for the stator and rotor have a significant effect on the core loses in the SRM. Several kinds of low-loss magnetic steels like

laminated amorphous alloy, general-purpose low-loss silicon steel, high-silicon steel Super E-Core and 6.5% high silicon steel [121-123] can be used to minimise the core losses in SRMs. Moreover, the windage loss in SRMs is not significantly disadvantageous to the whole system in all cases because it depends on individual applications. However, it was described in [124] that the windage losses of SRMs with salient rotor poles are greater than that of those with cylindrical rotor poles. In addition, the large windage loses is specifically far more significant during high-speed applications of the SRM like in drills, vacuum cleaners, and dryers, etc, because the windage loss is proportional to the square of the motor speed. Several control techniques [125-129] and geometric design [130-133] of SRM are important approaches to improve its overall efficiency.

2.2.5 Torque Density of SRM

A unipolar current is applied to each phase of the SRM within the appropriate rotor position while two or more adjacent phases can be exited concurrently to minimise torque ripple. Thus, it is difficult to achieve the desired phase current profile during high-speed operation as the current pulse width is usually wide-spanning into the negative torque zone. This limits the torque-generating ability of the machine and can cause large errors in torque and rotor position estimations [39, 134, 135]

Torque density is generally different across ranges of electric machines subjective to the machine's size, weight, topology, cost, and control method. Most often, PM machines produce higher torque densities compared to induction machines (IMs) and SRMs due to its magnet field excitation. Nevertheless, reluctance machines with competitive torque density are recently researched and developed. Torque density of an SRM can be significantly enhanced by utilizing new materials, optimizing the mechanical geometry and stator-winding distributions [18, 19, 136-149].

2.2.6 Multi-Objective Design and Control Optimization of SRM

SRM drive optimizations are generally focused on a single performance index, as reviewed in the previous sections. Nonetheless, the potential disadvantage with a single objective optimization method is the decrease of other essential performance indices due to comptonization while optimizing the desired one. Several emerging trends in the design and optimization of SRMs, combining the multi-physics features and the control features with the electromagnetic characteristics part is recently gaining more interest in academia and industry.

The design and operation of most practical applications of electric drives require optimization of more than one performance index, which makes the consideration of multi-objective optimization in SRM drives very important. The SRM multi-objective design and optimization approach should consider several performance indices, modelling procedures, control methods, and computational speed.

Mostly, the studies in multi-objective geometry optimization of SRMs make use of some form of stochastic algorithms to make the optimal design exploration, through evaluation of many design prospects based on numerous arbitrarily created unbiased key variables, for the desired application. These key variables normally include the most important SRM design parameters like the rotor and/or stator pole heights/arc, the stack length, the air gap diameter, the number of phases, the number of winding turns, phase resistance, and the current density [28, 89, 130, 150-160].

Multi-objective optimization in the control processes of SRM has also be investigated over the years. Multiple SRM control objectives, like the torque ripple minimization, acoustic noise minimization, efficiency improvement, can be simultaneously achieved through optimal tuning of multiple control parameters and/or controlled variables such as phase current, phase torque and conduction angles [86, 155, 161-164].

2.2.7 Sensorless Control of SRM

One of the SRM drives requirements is accurate and rapid knowledge of its rotor position because of its principle of operation. A position transducer is conventionally employed to detect rotor position in the SRM however, it adds extra size, weight, and cost to the drive system. Additionally, position transducers have a tendency to reduce the reliability of the drive, especially in some specific applications, as they add additional physical connections and can be vulnerable to environmental factors. Hence, an encoder-less control method of the SRM can be developed to estimate its rotor position through the measured machine's terminal current and/or voltage measurements [165, 166]. Though, these measured feedback signals from the machine are often altered by measurement errors and noise within the signal acquisition chain. Consequently, the efficacy of the estimation process depends on the robustness of the estimation procedure employed to cope with these measurement uncertainties.

The estimation of rotor position in SRM drives is generally based on the relationship between the machine's phase flux-linkage, phase current and rotor position. It is often impractical to directly measure the flux-linkage of the machine; as a result, it is normally approximated by integrating the voltage across an excited phase, and this process involves the measurement of the phase voltage and the phase current. The overall accuracy of the estimation process is affected by several error components as summarized in Table 2.1.

Numerous researches have been conducted to minimize errors in flux estimation for encoder-less (sensorless) control of SRMs. In [167] a DSP-based automated error-minimization technique for flux-linkage measurement in SRM drive has been presented, which involves phase resistance estimation in a virtual instrumentation form and an online offset correction. Yan *et' al* suggested a circuit-based flux-linkage measurement scheme with an automated winding-resistance correction technique to remove errors in sensorless control of SRMs. This process needs an additional circuit component [168].

Table 2.1: Sources of Feedback Error in SRMs

Measurement Errors	• Sensor offset error • Sensor scaling error
Measurement Noise	• Capacitive coupling of measuring circuit • Electromagnetic interference from the motor, Power circuit and other electronic devices within its vicinity.
Flux-linkage Calculation Error	• Integration offset error. • Time and amplitude quantization error • Variation of phase resistance due to temperature change

On the other hand, different flux-linkage estimation methods with included error reduction technique but consist of no additional hardware are presented as follows: In [169] Peng et al proposed the use of a third-order Phase-Locked Loop (PLL) to reduce the effect of terminal measurement noise and measurement residual error in SRMs for a numerical method of flux-linkage estimation. An integral flux error correction technique has been designed and developed in [170] to reduce phase-resistance error as a result of temperature variation in SRM drives. A feedback controller is used to correct the resistance of each phase when the phase current is zero. Recently, flux-linkage prediction methods based on Artificial Intelligence (AI) are employed to eliminate the effects of parameter variation, measurement error noise on flux-

linkage estimation were also reported. These methods utilized the phenomenon that the error accumulation in SRM flux-linkage estimation will reset at the end of each electrical cycle of the process [171-173].

In summary, methods used for estimation of SRM rotor position are based on its flux-linkage models, which often requires additional of extra device(s) and or function(s) to correct the flux calculation-errors caused by machine terminal measurement errors and/or noise, increasing real-time computation/implementation cost. In Chapter 6 of this thesis, an inductance model based Sliding Mode Observer (SMO) is employed to estimate SRM position without the requirement of additional functions for flux-linkage calculation and machine-terminal measurement error corrections. The induction model is built from the MASRM data collected by running the machine with a position sensor to get the relationship between its rotor position phase current and inductance. With the built model based sensorless control, the MASRM can then be operated without the position sensor. It uses only operating signals, so no additional sensors or external circuitry are needed. Its computational simplicity and robustness make it a superior choice for sensorless control of MASRM drives.

2.3 Applications of SRM

Switched reluctance machines are recently used in both domestic and industrial applications especially where high robust and low cost are critical. The most widely applications of SRMs include EV/HEVs, more electric aerospace systems, wind generators, pumps, and energy storage systems. SRMs are most suitable for certain applications compared to their counterpart electric machines where the environment of operation is harsh because of its mechanical and thermal robustness, as it does not include permanent magnets and copper bars in its rotor poles. Though, there are various compromises compared to the other electric machines that limit its applications where high torque density, low torque ripple, low acoustic sound, and low vibration is crucial.

2.3.1 Electric Vehicles /Hybrid Electric Vehicles

The current trend in reducing fossil fuel consumption and low toxic gas emission to protect the environment leads to the recent interest in EVs and HEVs. Above all, the regenerative mode of operation available in EV/HEVs, which can absorb most of the energy released during the

braking period of the vehicle, increases the EV/HEVs utilization in the urban areas that are prone to high traffic.

SRMs are suitable for EV/HEV applications because of its lack of PMs in its rotors and are often constructed with silicon steel, which increases its robustness and lowers its cost [2, 145, 174-176]. This is of high advantage because EV/HEV applications normally involve subjection of the traction motor to high temperature and cost reduction is a very important factor in automotive manufacturing. However, SRMs inherent large torque ripple, high acoustic noise, radial vibration, and unconventional power converter thwarted the extensive implementations of SRMs on EV/HEV powertrains. These drawbacks can be overcome by the solutions proposed in this research.

2.3.2 Aerospace Systems

Most of the aircraft operations are done using hydraulic and mechanical systems with few performed with electrical systems usually a wound-field synchronous machine. For the past century, research and development in the name of More Electric Aircraft (MEA) have been done to replace many non-propulsive mechanical and hydraulic systems such as engine starters, flight control actuators, pumps, and brakes with electrical systems [18, 177-180]. The reason for converting to MEA is because electrical systems can offer more advantages project towards improvements in reliability, weight, volume, cost, and maintainability.

The main attraction of SRM towards MEA applications is its superior thermal and mechanical robustness as aerospace applications normally involve unfavourable environmental factors like very high temperatures and pressures [181-184]. Thus, the SRM is ideal for MEA because of the non-existence of any or very small magnets or windings in its rotor. The electric machine used in this study is an example of the SRM designed for MEA application.

2.3.3 Wind Generators

Wind energy is one of the promising sources of clean and renewable of generating large electric power. Hence, there is a growing interest in developing and utilizing electric machines-based natural energy generation systems [185-188]. SRMs have the advantage of robustness to harsh environments compared to the doubly-fed induction generators and PM synchronous generators which are often employed for wind energy harnessing. This is because of its lack of PMs and windings in its rotor [189, 190].

Nevertheless, the inherent torque ripple, radial vibration, acoustic noise, unconventional converter topology, EMF, and large DC-LINK current ripple of SRM drives are needed to be considered when using SRM in wind generators depending on the desired environment of operation. The multi-objective control problem in this research is an example to this kind of multi-objective problems

2.3.4 Pumps, Spindles, and Superchargers

High-speed and low-torque electric drives are normally used in and heat pumps, generators, and starters for portable gas turbines, turbo compressor systems, machining spindles, and circuit board drillers. PM machines are the most common electric machines employed in the current ultra-high-speed application above 50,000 rpm [191, 192]. SRMs are also good candidates for high-speed applications with the added advantage of having a high tolerance to a harsh environmental condition like very high or low temperature, and high pressure [193]. The topology of high-speed SRMs is often designed to have a lower number of rotor/stator poles such as to reduce the switching frequency of the power converter. Nonetheless, the drawback of SRM in this application is the inherent large torque ripple and high acoustic sound. Furthermore, it has additional limitations during high-speed operations such as increased windage loss due to rotor saliency, and increased iron loss due to the large amplitude of flux-linkage variations (caused by the high-speed operation).

2.3.5 Energy Storage Systems

Flywheels are the commonly used energy storage systems because they have comparatively low size, have a high mean time between failure, have high robustness and it can be used for long term energy storage because of its low idle losses [194] An SRM has the merit of high robustness, compactness, and it is simple to cool, compared to other electric machines, which makes it promising for this application. However, the PM machine shows higher efficiency compared to SRM and synchronous machines used as generators for the flywheel energy storage systems [195].

2.4 Summary

In this chapter, a comprehensive review of the modelling, the limitations, the performance improvement, and the applications of SRM were presented. Applications of SRMs in several industries are mainly challenged by its inherent drawbacks including its large torque ripple,

high acoustic noise, high radial vibration, low torque density, and low efficiency over the entire operating range. Fortunately, there is an increasing interest in the academic industry to improve the abovementioned limitations through revising, analysing, designing, and developing numerous new SRM geometries and control techniques. The theories and the properties of the numerical and analytical methods are reviewed and compared based on their accuracy and computational cost. The previous and present methodologies aiming to minimize the torque ripple, acoustic noise, and radial vibration, and enhance the torque density and efficiency of the SRM drives are discussed. In addition, the performances of various multi-objective optimization methods are discussed and compared. Lastly, the summary of trending applications of SRM drives such as HEVs/EVs, aerospace systems, wind power energy systems, pump systems, and energy storage systems are presented.

CHAPTER 3

SYSTEM DESCRIPTION AND MODELLING

This chapter describes the permanent magnet-assisted switched reluctance machine drive employed in this study. The machine drive is designed to produce higher torque density and efficiency like a permanent magnet motor drive of the same size and mass with the added advantage of been fault tolerant. Its torque is increased by increasing non-saturation region of the stator lamination. This is achieved by laying magnets at the stator slot opening of SRM to extend its operation rang to the third quadrant of the B-H curve such that the flux from the magnets opposing the main coil flux, hence, the operating range of the machine can be extended to third quadrant of the B-H. This process reverse magnetises the stator core material of the novel machine which results in it taking longer for the stator core to become saturated

The operating range of a conventional SRM is limited to only the first quadrant of the B-H curve. By laying magnets at the stator tooth tip, the operation range of the MASRM is extended to the third quadrant of the B-H curve as discussed in Chapter 1 (Figure 1.1). The process reverses the magnetics of the stator core material which results in it taking longer to become saturated (peculiarly at the aligned position) increasing the overall area between aligned and unaligned inductance [18] [196]. This modification of the conventional SRM improves its torque density but it also increases its nonlinearity and torque ripple hence, increasing its difficulty to control. The motor is developed for an airplane nose wheel application [196].

Figure 3.1 shows the inductance profile of the MASRM used in this project. As shown, the inductance at the aligned and unaligned positions is flat while it has a high rate of change in between. Compared to the conventional SRM, the MASRM has steeper mid, and more saturated (flatter) aligned and unaligned inductance profile. These high rate of change and nonlinearity increase the computational complexity of the modelling and control, and also the sensitivity to measurement errors. Moreover, it can increase the MASRM torque ripple because of added cogging torque due to the flux from the added magnet. Hence, all these added limitations increase the MASRM difficulty to be controlled using conventional methods especially those that require online computation of its nonlinear dynamic model.

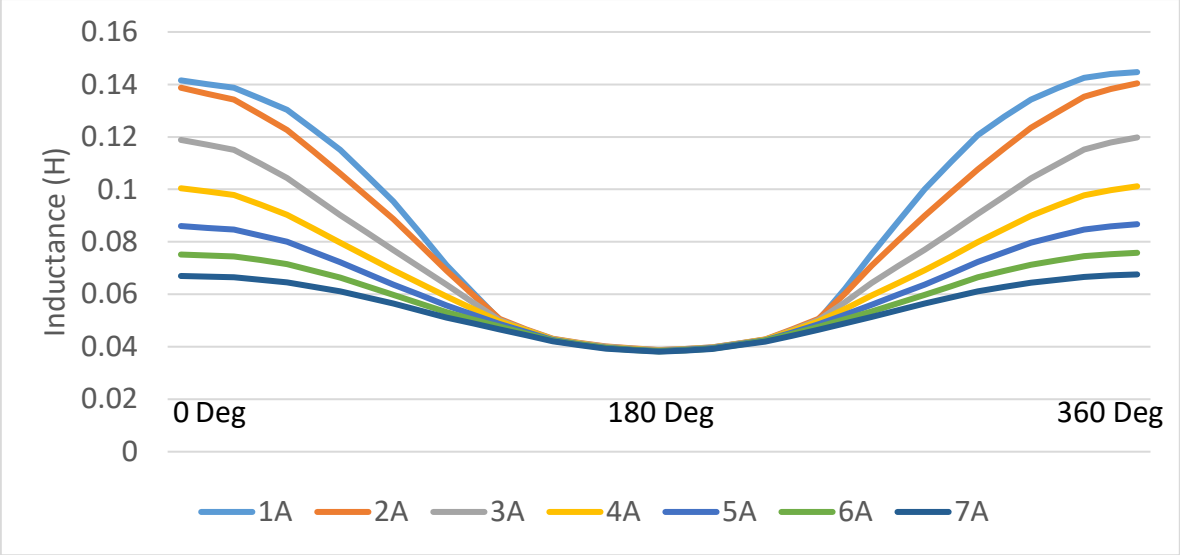

Figure 3.1: Estimated Inductance Profile of MASRM for Simulation and Sensorless control

3.1 Static Test of MASRM

There are two sets of data that are needed for the test of the MASRM, which are the torque, current and rotor position relationship data, and the flux-linkage, current, rotor position data which will be used for modelling and control design of the drive. The test data can be obtained from what is called a standstill (static) test. The basic procedure of standstill test is to apply a short voltage pulse to the phase winding of the machine with the rotor blocked at several predefined specific positions.

During the testing process, the rotor of the MASRM is blocked at a rotor position from 0 degree to 360 degrees in an interval of 10 degrees using an absolute encoder (an R35i-8192/0-8mm-LD/0-5/0-1-R-H unit from Hiedenhan/Renco). A Texas Instrument F28377D DSP-based controller board is used to generate the gating signals to an asymmetric half-bridge converter to apply an appropriate voltage pulse to that test winding. The rotor position, phase current, phase torque (estimated from phase current and rotor position) and phase flux-linkage are recoded at these different rotor positions. Data sets obtained from performing this test can be used to establish the relationship between magnetic and torque characteristics of the MASRM as it will be explained in the coming sections. Figure 3.2 shows the experimental setup for the static test of the MASRM.

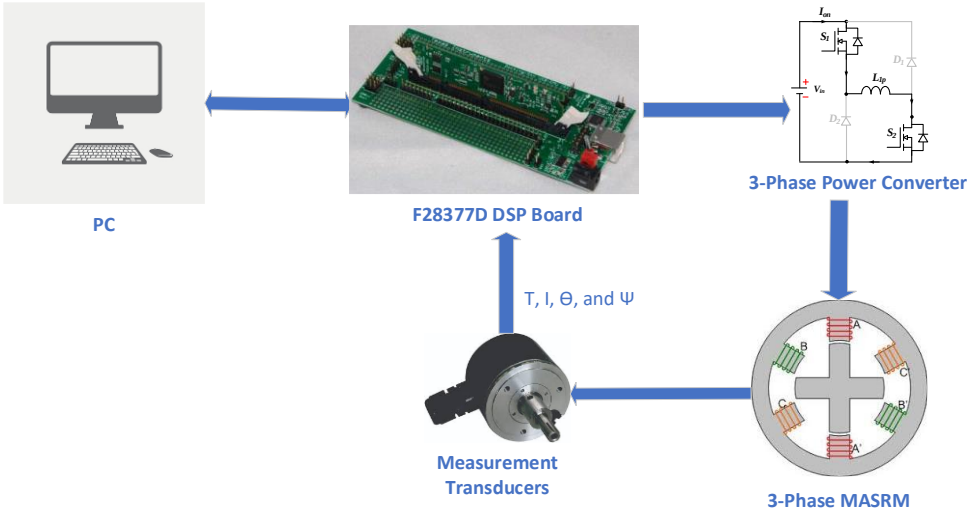

Figure 3.2 Experimental setup for the test of MASRM drive

3.2 Model of MASRM

The characteristic modelling and analysis for the behaviour of MASRM can be done using its derived torque and voltage mathematical equations.

3.2.1 Torque Characteristics of MASRM

MASRMs are structured to have both salient rotor and stator poles, therefore, the flux-path reluctance for the phase windings changes with change in rotor position of the machine. Consequently, torque generation in SRMs is as a result of the rotor pole movement to align with the excited stator pole so as to minimise the flux-path reluctance. This principle of torque production can be mathematically explained by using the phenomenon of electromechanical energy conversion.

Magnetic flux ψ is generated in MASRM when the stator poles are excited with current *i*. the relationship between the flux and the magnetomotive force (MMF) is depicted in Figure 3.3. It can be observed that the flux-MMF characteristic for the aligned position ($\theta = \theta 2$) is nonlinear because the flux-path reluctance suffers from magnetic saturation. While that of the unaligned position ($\theta = \theta 1$) is almost linear because the air-gap reluctance is large in this region.

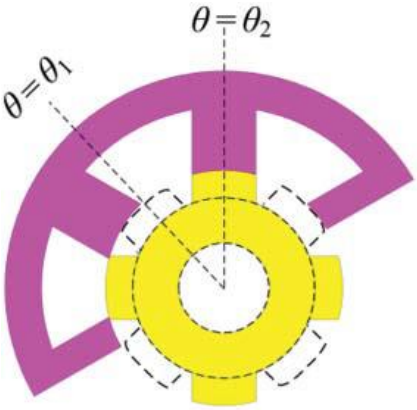

(a)

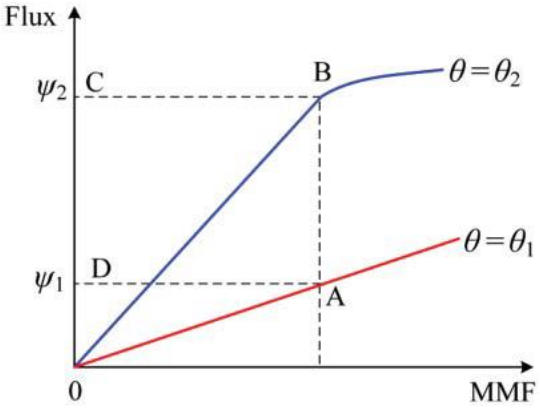

(b)

Figure 3.3: Principle of SR machine torque production: (a) rotor positions and (b) flux characteristics [197].

The input energy W_i can be expressed as in (3.1) upon energizing the phase windings of the machine.

$$W_i = \int e\, i\, dt \tag{3.1}$$

Where e is the induced electromotive force (EMF) which is given as:

$$e = \frac{dN\psi}{dt} \tag{3.2}$$

Hence the input energy can be written as:

$$W_i = \int F_i d\psi \tag{3.3}$$

Where $F_i = N\, i$ is the magnetomotive force (MMF) excited in the phase windings and N is the number of turns of the phase windings.

Consider the input energy to be equal to the sum of the magnetic energy field stored in the phase winding W_f and the output energy converted to motion W_o. So, the expression for incremental changed can be written as below:

$$\delta W_i = \delta W_f + \delta W_o \tag{3.4}$$

Furthermore, by considering the flux-MMF relationship depicted in Figure 3.3,

$$\delta W_i = \int_{\psi_1}^{\psi_2} F_i d\psi = area\ (ABCD) \tag{3.5}$$

$$\delta W_f = area\ (OBC) - area\ (OAD) \tag{3.6}$$

Hence,

$$\delta W_o = \delta W_i + \delta W_f = area(OAB) \tag{3.7}$$

which is the area between the two characteristics for a given MMF. Therefore, the torque T can be expressed as incremental output with respect to variation in rotor position as follows:

$$T = \frac{\delta W_o}{\delta \theta} \tag{3.8}$$

δW_o is generally equal to the change of co-energy W_f' between the unaligned and aligned rotor positions, which can be expressed as the complement of the magnetic field energy in the following form:

$$W_f' = \int \psi F_i dF_i = \int N\psi di = \int L(\theta, i) i\ di \tag{3.9}$$

where L is the inductance which is the ratio of flux-linkage to phase current. Hence, the produced torque can be written as:

$$T = \frac{\delta W_f'(\theta, i)}{\delta \theta} \quad , \ i = \text{constant} \tag{3.10}$$

The inductance L changes linearly with the current for a given rotor position under no magnetic saturation, but the linearity cannot be guaranteed under magnetic saturation. The torque under the conditions can be expressed as (3.11) and (3.12), respectively.

$$T = \frac{1}{2} i^2 \frac{dL(\theta)}{d\theta} \tag{3.11}$$

$$T = \int_0^i \frac{dL(\theta,i)}{d\theta}\, idi \tag{3.12}$$

Finally, the resultant output torque, *Te* is the summation of torques developed at various phases:

$$Te = \sum_1^3 T(i,\theta) \tag{3.13}$$

which can also be represented in the equation of motion of the motor

$$T_e = J\frac{d\omega}{dt} + Bw + T_L \tag{3.14}$$

where *J* is the moment of inertia, *B* is the coefficient of viscous friction, T_L is the load torque, and ω is the rotor speed.

3.2.2 Magnetic Characteristics of MASRM

The voltage equation of the MASRM can be expressed as (3.15) by neglecting the mutual inductance between the phases:

$$v = iR + \frac{d\psi}{di} \tag{3.15}$$

$$v = iR + \frac{d}{dt}(L(\theta,i)i) \tag{3.16}$$

$$v = iR + L(\theta,i)\frac{di}{dt} + \frac{dL(\theta,i)}{d\theta}\, i\, \omega_m \tag{3.17}$$

where v is the applied phase voltage, *R* is the winding resistance per phase, and $N\psi$ is the flux linkage due to the phase current *i*. The inductance *L* is defined as the flux linkage over current. The three terms on the right-hand side represent the resistive voltage drop, inductive voltage drop, and back EMF of the SR machine, respectively.

In conventional switched reluctance motor, the flux-linkage varies linearly with phase current under the unsaturated condition at any rotor position while under saturation condition, the SRM has the same saturation point as the current remains constant and the flux linkage.[198, 199]. On the other hand, the magnet-assisted switched reluctance motor as it has a different saturation point for different rotor position. Considering Figure 3.4 it can be observed that the flux-linkage changes linearly with phase current at lower current values. It can also be seen that at lower angles (unaligned region), the linearity of the flux with respect to current has a larger linear

region and it decreases as the rotor approaches the aligned position. In summary, the MASRM flux-linkage characteristics have higher non-linear characteristics than conventional SRM which makes it more difficult to model and control. The flux- linkage and torque characteristics nonlinearity of the MASRM can be analysed at a given operating point with respect to phase current and rotor position in the coming sub-sections.

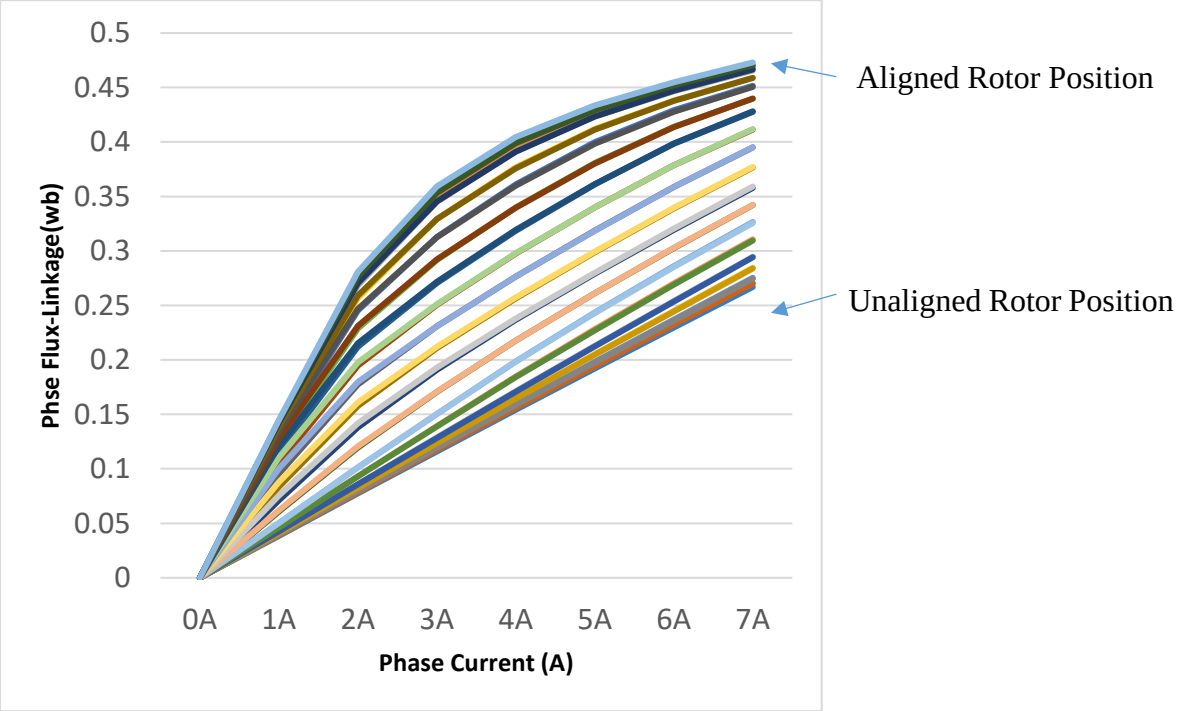

Figure 3.4: Measured Flux-linkage characteristics of MASRM.

3.2.3 Analysis of Flux-linkage characteristics in the Unsaturated Condition

It can be observed from Figure. 3.4 that the flux linkage varies linearly with current for any rotor position under unsaturation condition up to a certain value of current $i(\theta) = c$. Therefore, the flux-linkage can be formulated as follows:

$$\psi \approx L_1(\theta) i, \qquad i(\theta) \leq c \tag{3.18}$$

where $L_1(\theta)$ is the unsaturated inductance, which varies with rotor position θ. Expressions for flux-linkage in unsaturated condition are:

$$\frac{\partial \psi}{\partial i} = L_1(\theta) \tag{3.19}$$

$$\frac{\partial \psi}{\partial \theta} = \frac{dL_1}{d\theta} i \tag{3.20}$$

Based on equations (3.15), (3.19) and (3.20), the dynamics in the phase current under unsaturated condition can be represented as:

$$v = (R + \frac{dL_1}{d\theta}\omega_m)i + L_1 \frac{di}{dt} \tag{3.21}$$

Note fron Figure 3.1 that L_1 is minimum at $\theta = 180^0$ (unaligned rotor position) and is maximum at $\theta = 360^0$ (aligned rotor position). Similarly, $\frac{dL_1}{d\theta}$ is maximum close to $\theta = 270^{\circ}$.

3.2.4 Analysis of Flux-linkage characteristics in the Saturated Condition

The flux-linkage curves can also be approximated as a straight line under saturation condition but with a different value of incremental inductance. As seen in Figure. 3.1, the saturated incremental inductance L_2 is strongly dependent on θ. Hence, each ψ–I curve can be approximated as shown below, where $c(\theta)$ represents the knee of the ψ–I curve at θ:

$$\Psi(i,\theta) \approx L_2(\theta)i + [L_1(\theta) - L_2(\theta)]c(\theta), \qquad i > c. \tag{3.22}$$

L_2 varies with position, and its change is significant where incremental inductance is least. The MASRM used in this study is strongly saturated beyond a critical position ($\theta = 290^{\circ}$). The partial derivatives and the phase voltage under saturated condition can be expressed as follows:

$$\frac{\partial \psi}{\partial i} = L_2(\theta) \tag{3.23}$$

$$\frac{\partial \psi}{\partial \theta} = c\frac{dL_2}{d\theta} + L_2\frac{dC}{d\theta} - c\frac{dL_{21}}{d\theta} - L_1\frac{dC}{d\theta} \tag{3.24}$$

$$v = iR + L_2\frac{di}{dt} + (c\frac{dL_2}{d\theta} + L_2\frac{dC}{d\theta} - c\frac{dL_{21}}{d\theta} - L_1\frac{dC}{d\theta})\omega_m \tag{3.25}$$

The last term in the right-hand side of (3.25) is the back-EMF term.

3.2.5 Analysis of the instantaneous torque

Figure 3.5 depict the non-linearity of the MASRM torque characteristics. As explained in section 3.2, the nonlinear instantaneous torque of the machine can be found from the co-energy principle. By considering (3.11) and (3.12) the total phase torque can be expressed as:

$$T \approx \frac{\partial \psi(i,\theta)}{\partial \theta}\, i \tag{3.26}$$

The incremental inductance of an SRM has larger value therefore, its phase current and rotor speed can be assumed constant in a single sampling interval [200]. With this assumption (3.17) can be reduced to:

$$v \approx iR + \frac{\partial \psi(i,\theta)}{\partial \theta}\, i\, \omega_m \tag{3.27}$$

Therefore,

$$T \approx \frac{v - i\,R}{\omega_m} \tag{3.28}$$

And for negligible resistive drop, equation (3.29) shows that phase voltage can be an effective control variable for torque control, nevertheless, with low accuracy.

$$T \approx \frac{v}{\omega_m} \tag{3.29}$$

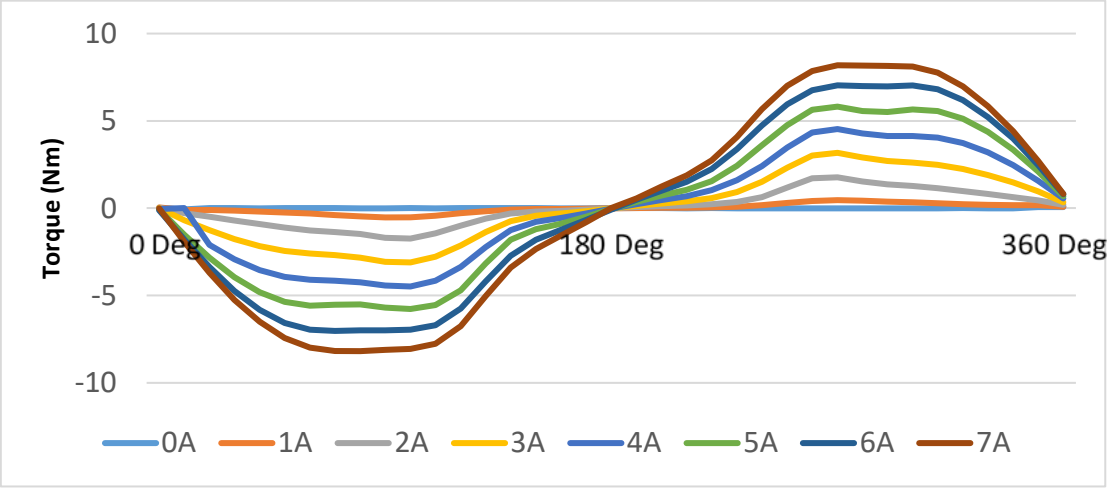

Figure 3.5: Estimated Torque Characteristics of MASRM at different current level

3.3 System Simulation

Simulation is generally performed first to ensure the successful controller development. The parameters of the real system will be identified at this stage of control system development. Hence, the simulation of the MASRM drive is discussed in this section.

As explained in Chapter 2, there are two main categories of SRM control which are the current control and the torque control. In this study, the focus will be on torque control of the MASRM

drive. Firstly, a simulation model of the three-phase MASRM used in this study is developed in MATLAB Simulink for analysis and controller design. Secondly, the asymmetric power converter employed in the drive is also simulated. Lastly, the conventional hysteresis current controller is also simulated to be used as a benchmark for the considered torque control methods.

3.3.1 Dynamic model of the MASRM

The static parameters obtained through experiment depicted in Figures 3.3 and 3.4 are used in the creation of a dynamic model using MATLAB/Simulink software. The dynamic model consists of (3.17) and two lookup tables (Flux LUT and Torque LUT) as shown in Figure 3.5. The dynamic model is used to simulate the transient and steady states response of the drive.

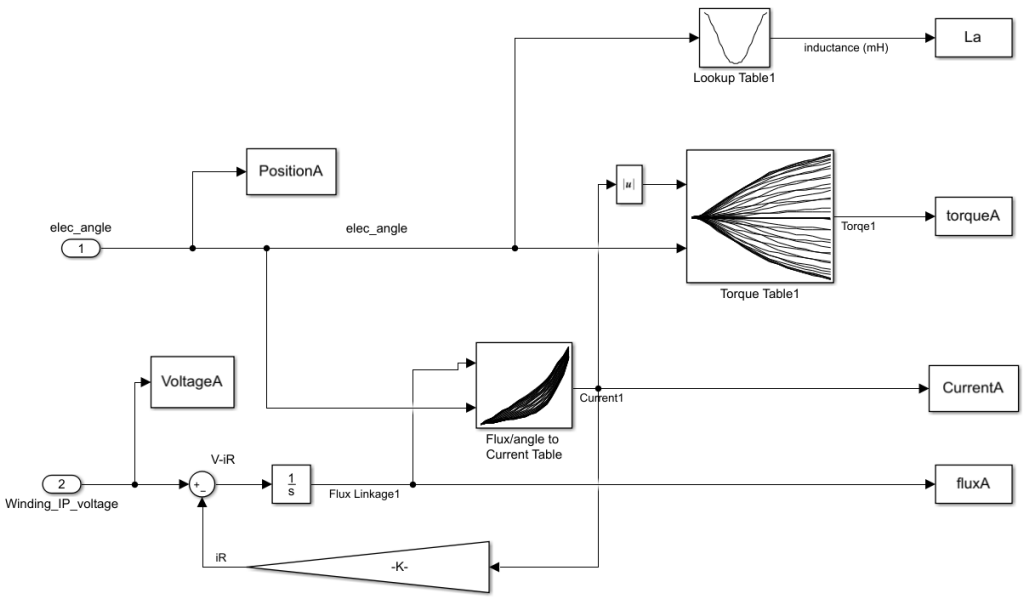

Figure 3.5. Phase A simulation of MASRM dynamic model

3.3.2 Modelling of MASRM Converter

A standard IGBT based asymmetric half-bridge converter is employed to energise the MASRM drive considered in this study because of its good efficiency and control flexibility as explained in Chapter 3. Figure. 3.6 shows the three-phase MATLAB/Simulink simulation model of asymmetric half-bridge converter for the MASRM drive. The unique operations of this converter with respect to this study will be explained in detail in Chapter 5.

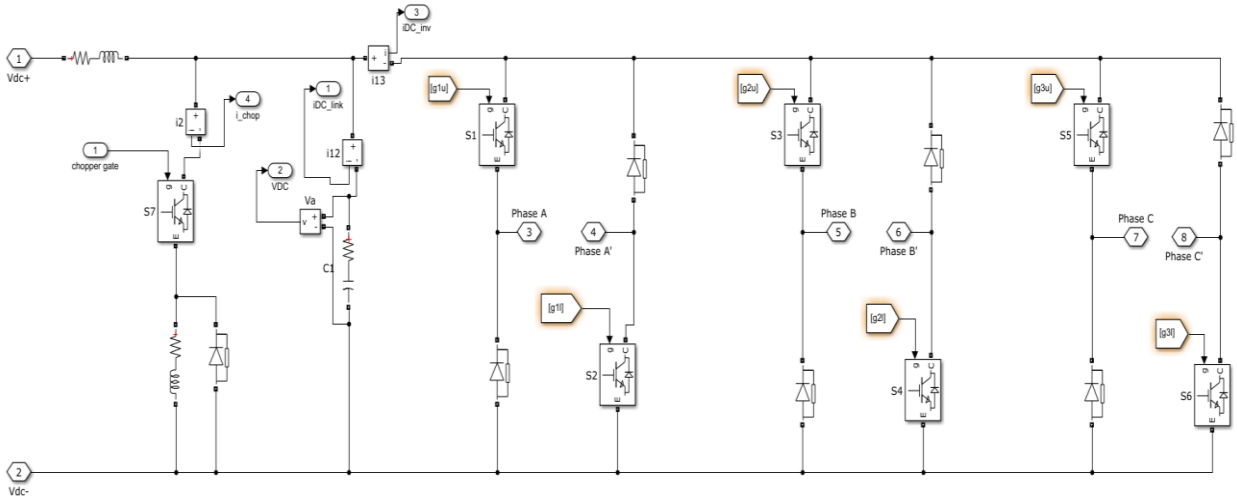

Figure 3.6: Simulation Model of Asymmetric Half-Bridge Converter

3.4 MASRM Model for estimation of rotor position

The preferred online dynamic model for this study is the curve fitting model in the closed form because of its merits as stated in Chapter 2. There are two main types of SRM closed-form models are suitable for online implementations as suggested by several researchers; inductance-based model [201, 202] and flux-linkage based model [203-206]. Following a review of the two online dynamic models, the inductance-based model has been selected for the MASRM system, because it provides a flexible and simple method for taking the unique shaped inductance profile of the MASRM into consideration when estimating its rotor position. Below is the discussion of the two modelling methods and a detailed explanation of the rotor position estimation procedure is given in Chapter 6.

3.4.1 Flux-linkage based model

The flux-linkage based model of SRM uses the nonlinear relationship between the phase flux-linkage, phase current and rotor position of the machine. The mathematical expression of this relationship is presented in equation (3.30). From this relationship, the rotor position of SRM can be deduced from the known value of phase flux-linkage and phase current [204].

$$\psi = \psi_s(1 - e^{-f(\theta)i}) \tag{3.30}$$

where

$$f(\theta) = a + b \cdot cos(\theta) + c \cdot \cos(2\theta) + d \cdot \sin(\theta) + e \cdot \sin(2\theta) \tag{3.31}$$

ψ_s is a saturated flux-linkage and $a,\ b,\ c,\ d$ and e are the coefficients of the series.

In an SRM control systems, the flux-linkage ψ can be computed by equation (3.32) as the phase resistance R is assumed to be known and constant, and phase voltage *V* and phase current *i* can be measured.

$$\psi = \int (V - R\ i) dt \tag{3.32}$$

The basic principle of flux-linkage based estimation of rotor position in SRM is based on the fact that the rotor position θ can be calculated from the $\psi - \theta - i$ relationship, because ψ and i are known.

It is normally required for MASRM to run for its full range of speed in most applications, from very low speed (near zero) to very high speed at steady state. Given That the flux-linkage based method of estimating rotor position utilizes the integration in (3.32) to estimate the flux-linkage. Errors in values of parameter such as the phase resistance, and measurements V and i can accumulate during conduction of the active phases, which can only reset when a phase is not conducting [39, 178, 207]. However, same problems do not exist in inductance-based method of estimating of rotor position. This makes the inductance-based model a better choice for applications of SRMs that require full range of speed. An inductance based model that can be used for accurate estimation of rotor position for wide range of speed is proposed in [201]. Nevertheless, considering different signals, devices used and intended application, the inductance model-based method of estimating rotor position can require modifications which depends on computational cost and accuracy. The inductance-based model developed for this study is discussed in the next section.

3.4.2 Inductance model of MASRM

Generally, the phase inductance of SRMs changes periodically with its rotor position 'θ'. Therefore, it can be expressed as a Fourier series function of the rotor position. The inductance '$L(\theta, i)$' in the MASRM online model for this study can be derived from finite terms of the Fourier series as explained in Chapter 2, with the coefficients of the series representing the non-linear change of the inductance with the phase current.

For simplification of the expression for the inductance function, the origin of the rotor position is chosen to be at the aligned position. For 3-phase switched reluctance machines, the number

of rotor poles N_r = 6. By considering Figure 3.1, 'θ = 0 ^{o}' can be selected at the aligned rotor position of phase A, and 'θ = 180 ^{o}' can be selected at the unaligned position of phase A. Therefore, the individual phase inductance can be expressed as in (3.32)

$$L(\theta, i) = \sum_{n=0}^{\infty} A_n(i) \cdot \cos(nN_r\theta + \varphi_n). \tag{3.32}$$

where φ_n is the phase shift between the machine phases, and A_n represents the coefficients of the series whose values are generally obtained through curve fitting method.

The coefficients $A_n(i)$ in the Fourier series can be obtained using the inductances at different specific rotor positions. Let the phase inductance at a rotor position be expressed as in (3.33), which is a function of phase current 'i'.

$$L_\theta(i) = \sum_{n=0}^{q} a_{\theta,n} i^n \tag{3.33}$$

Where '$a_{\theta,n}$' and 'q' are the coefficients and the order of the polynomial, respectively. A value of 'q = 5' and the first Four terms of the Fourier series are selected in this study as to ensure a balance between good approximation and computational cost, after comparing the fitting results (q = 3, 4, 5 and 6, and Fourier series terms of 3, 4 and 5) using the algorithm presented in Appendix A,

The four coefficients of the Fourier series can be computed as A_0, A_1, A_2, and A_3 from the MASRM phase inductance at four rotor positions: L_{0^o} (aligned rotor position), L_{60^o} (lower mid-aligned rotor position), L_{120^o} (upper mid-aligned rotor position), and L_{180^o} (unaligned rotor position), which can therefore be represented in (3.34).

$$\begin{bmatrix} L_{0^o} \\ L_{60^o} \\ L_{120^o} \\ L_{180^o} \end{bmatrix} = \begin{bmatrix} 1 & 1 & 1 & 1 \\ 1 & \cos(60^o) & \cos(120^o) & \cos(180^o) \\ 1 & \cos(120^o) & \cos(240^o) & \cos(360^o) \\ 1 & \cos(180^o) & \cos(360^o) & \cos(540^o) \end{bmatrix} \begin{bmatrix} A_0 \\ A_1 \\ A_2 \\ A_3 \end{bmatrix} \tag{3.34}$$

Therefore, we have:

$$\begin{bmatrix} A_0 \\ A_1 \\ A_2 \\ A_3 \end{bmatrix} = \begin{bmatrix} 1/6 & 1/3 & 1/3 & 1/6 \\ 1/3 & 1/3 & -1/3 & -1/3 \\ 1/3 & -1/3 & -1/3 & 1/3 \\ 1/6 & -1/3 & 1/3 & -1/6 \end{bmatrix} \begin{bmatrix} L_{0^o} \\ L_{60^o} \\ L_{120^o} \\ L_{180^o} \end{bmatrix} \tag{3.35}$$

Which can further be expanded as follows for better representation:

$$\left.\begin{aligned} A_0 &= \frac{1}{3}\left[\frac{1}{2}(L_{0^o} + L_{180^o}) + (L_{60^o} + L_{120^o})\right] \\ A_1 &= \frac{1}{3}(L_{0^o} + L_{60^o} - L_{120^o} - L_{180^o}) \\ A_2 &= \frac{1}{3}(L_{0^o} - L_{60^o} - L_{120^o} + L_{180^o}) \\ A_3 &= \frac{1}{3}\left[\frac{1}{2}(L_{0^o} - L_{180^o}) - (L_{60^o} - L_{120^o})\right] \end{aligned}\right\} \quad (3.36)$$

These four coefficients generated as polynomial functions from inductance profiles of the MASRM are shown in Figure 3.7.

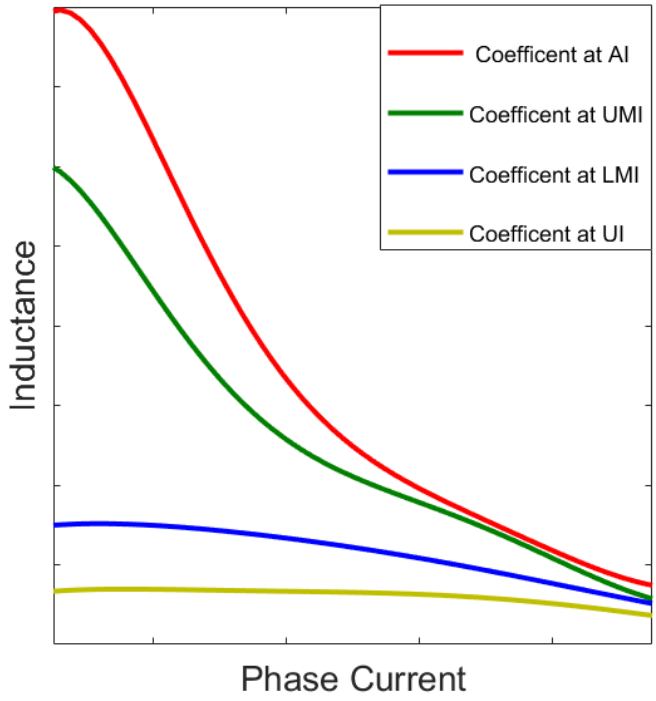

Figure 3.7. Curve fitted coefficients for Fourier series based inductance approximation of MASRM

Where the lebel in Figure 3.7 are AI is the aligned inductance, UMI is the upper mid-aligned inductance, LMI is the lower mid-aligned inductance, and UI is the un aligned inductance. Now, the dynamics of the MASRM can be modelled from its differential equations which include the electromagnetic equations, the electromechanical equations, and the mechanical equations by using the inductance estimation method above.

The voltage equation (electromagnetic equations) is a nonlinear differential equation in (3.37):

$$V_j = i_j \cdot R + L_j(\theta, i)\frac{di_j}{dt} + i_j\frac{\partial L_j(\theta,i)}{\partial \theta}\cdot\omega + i_j\frac{\partial L_j(\theta,i)}{\partial i_j}\frac{di_j}{dt}. \quad (3.37)$$

with j = 1…m, where m is the number of phases.

To reduce the weight and size of the motor drive system in this study, the individual terminal voltages are not measured using separate sensors instead, each phase voltage is approximated using the bus voltage and the calculated PWM duty cycle as expressed in (3.38) [208].

$$V_j = V_{bus} \cdot d_j - V_{igbt}(i_j) - V_{diode}(i_j) \tag{3.38}$$

where V_{bus} is the bus voltage, d_j, the phase duty cycle, V_{igbt}, the voltage drop across the power transistor, and V_{diode} the diode voltage drop. By substituting (3.38) in (3.37) we get (3.39).

$$V_{bus} \cdot d_j - V_{igbt}(i_j) - V_{diode}(i_j) = i_j \cdot R + L_j(\theta, i)\frac{di_j}{dt} + i_j \frac{\partial L_j(\theta,i)}{\partial \theta} \cdot \omega + i_j \frac{\partial L_j(\theta,i)}{\partial i_j}\frac{di_j}{dt} \tag{3.39}$$

For simplicity, the voltage drops across the winding resistor, power transistor and power diode are summed up into a single term, V_{loss}. then substituted in (3.39) and rearranged to the standard format of the differential equation of MASRM as presented in (3.40).

$$\frac{di_j}{dt} = \frac{V_{bus} \cdot d_j - V_{loss}(i_j) - i_j \frac{\partial L_j(\theta,i)}{\partial \theta} \cdot \omega}{L_j(\theta,i) + i_j \frac{\partial L_{j(\theta,i)}}{\partial i_j}} = \frac{X(\theta,i,\omega)}{Y(\theta,i)} \tag{3.40}$$

The torque-speed equation (electromechanical equations) can be expressed as:

$$J\frac{d\omega}{dt} = \sum_{j=1}^{m} T_{e\,j} - T_L \tag{3.41}$$

where $T_{e\,j}$ and T_L are phase torque and load torque, respectively.

The resultant torque can be obtained by the summing up the individual phase torques as expressed below:

$$T_e = \sum_{j=1}^{m} \frac{\partial W_{cj}}{\partial \theta} = \quad \sum_{j=1}^{m} \frac{\partial \int L_j(\theta,i) i_j di}{\partial \theta} \tag{3.42}$$

Therefore, the angular acceleration of the machine can be expressed as:

$$\frac{d\omega}{dt} = \frac{\sum_{j=1}^{m} T_{e\,j} - T_L}{J} = Z(\theta, i) \tag{3.43}$$

The mechanical equation can be expressed as:

$$\frac{d\theta}{dt} = \omega \tag{3.44}$$

Finally, the online differential equation for the MASRM can be solved based on the inductance model derived in (3.40). Where the required expressions are expressed in (3.45). This derived inductance model is employed in the sliding mode-based estimation of rotor position of the MASRM.

$$\left.\begin{aligned} \omega &= \frac{d\theta}{dt} \\ \frac{\partial L_j(\theta,i)}{\partial \theta} &= -\sum_{n=1}^{m} A_{k,j}(i) n N_r \sin(nN_r\theta) \\ \frac{\partial L_j(\theta,i)}{\partial i_j} &= \sum_{n=0}^{m} \frac{\partial A_{k,j}(i)}{\partial i_j} \cos(nN_r\theta) \\ L(\theta,i) &= \sum_{n=0}^{m} A_n(i) \cdot \cos(nN_r\theta + \varphi_n) . \end{aligned}\right\} \tag{3.45}$$

A model of the MASRM has been designed, simulated, and analysed. A new torque controller and position sensorless control algorithm for the MASRM drive has been designed simulated and analysed and presented in the coming chapters. In next section, the setup and implementation of an experimental test rig for testing and validation of the proposed control system is explained.

3.5 Experimental Test Rig

An MASRM drive test rig was designed and constructed to test and validate the better performance of the proposed torque controller in real-time. The three-phase MASRM was coupled to an induction machine as a load. The test rig consists of two sets of electric motor drives. One is based on the magnet assisted switched reluctance machine, which is the servomotor system for investigation of the proposed control system. The other one is for an induction machine, which serves as the load to the MASRM. A torque sensor is shaft coupled in between the two electric machines. Both motor drives are DSP based, with power converters, position encoders, and voltage and current sensors. A block diagram of the test rig is presented in Figure 3.7.

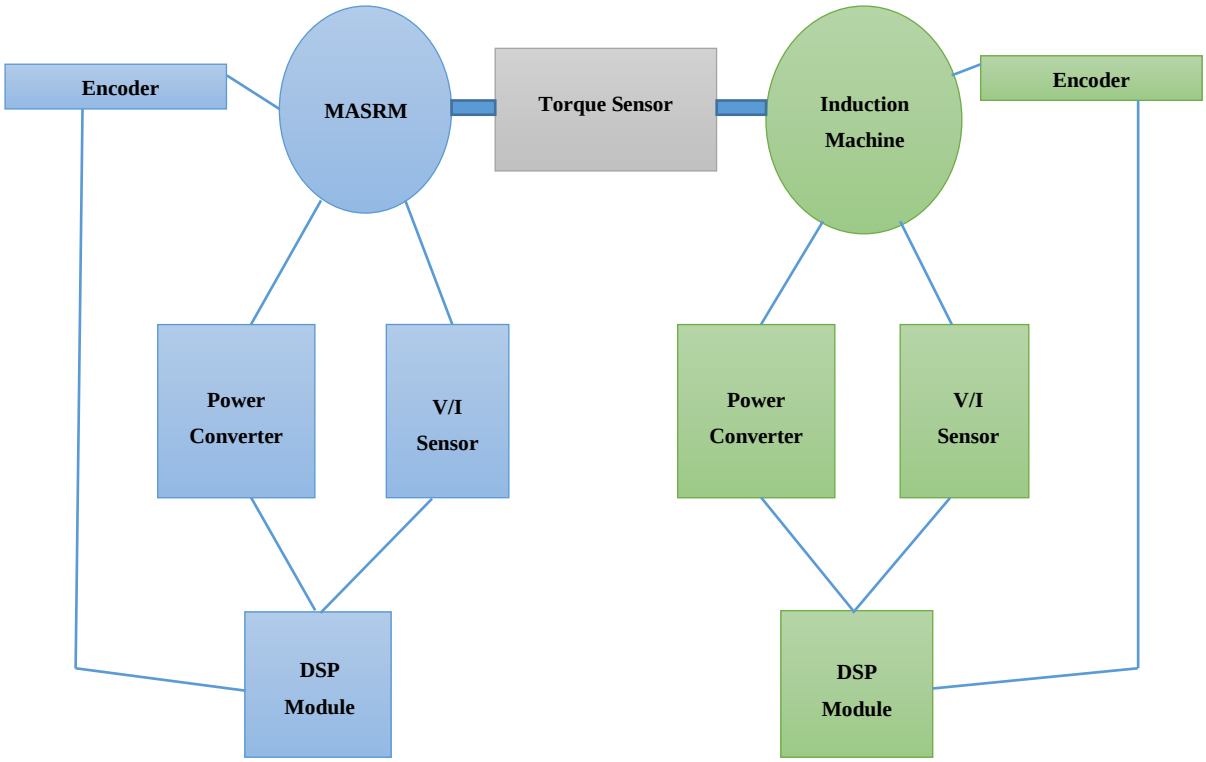

Figure 3.7: Block Diagram of Experimental Test Rig Setup.

The experimental test rig is used for data collection for modelling the MASRM, as described in section 3.1and also for implementation and performance evaluation of control algorithms. The induction machine drive used for loading the MASRM is based on the ABB ACSM1 drive. An IGBT based three-phase asymmetric bridge converter is used to energize the windings of the MASRM with main component as stated in Table 3.1. A Texas instrument F28377D DSP-based control board is used to implement the HCC, DITC, and proposed AQSM control algorithms. The DSP contains a dual CPU and provides a reliable interface that links with MATLAB/Simulink to access the hardware and software system of the controller board, which is a very convenient tool for control system development. For feedback, an absolute encoder (an R35i-8192/0-8mm-LD/0-5/0-1-R-H unit from Hiedenhan/Renco) and a current transducer for each phase were employed for a fair comparison, the optimum turn-on and turn-off angles are calculated at different speeds and used in a lookup table within the three compared control algorithms. The motor and power converter setups are shown in Figure 3.8.

Table 3.1: Components of the power converter

Gate Drive	A Seven pack IGBT Driver (SKHI 71) from Semikron
IGBT	A 12 pack IGBT (SKiiP 23Acc12T4V10) from Semikron
DC-Link Capacitor	2 Polypropylene, DC Link Capacitors (220uF 800V dc capacitor 944U221K8)

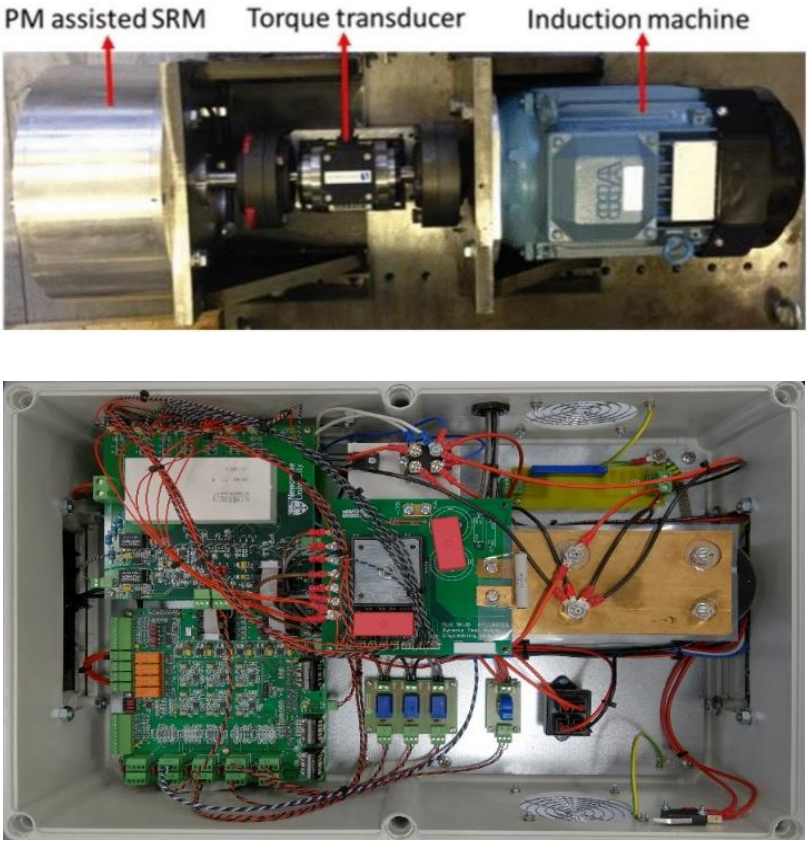

Figure 3.8: Test Rig Setup.

3.5.1 Texas Instrument F28377D based General Control Board

The control and interface board used in this project for the MASRM drive's power converter control is a copy of a general control board (GCB) that has been designed at Newcastle University and used in many research projects. The board is designed to provide an interface between the Texas Instrument F28377D microcontroller and power converter hardware. The functions included on the board are discussed presented in Appendix B. The GCB includes large number of general-purpose input/output (GPIO), ADC and PWM channels which are more than adequate for this project. It also includes RS232, Isolated USB, Encoder, Resolver and CAN bus interfaces. It can be connected to a host computer via an external XDS100v2 JTAG emulator.

The board is designed to be flexible, catering for a wide range of power electronic control applications. It is usually important that sensors and gate drive circuits are physically close the power hardware. For this reason, the sensors and gate drive circuits are not included on the general interface board. The on-board interfaces have been designed to cater for a range of different external sensors and gate drive circuits.

To create a converter, separate sensors and gate drive circuits must be provided in addition to the power circuit hardware. The gate drive interfaces of the GCB can be connected to a purpose designed gate drive circuits or to boards containing commercial gate driver modules as is the case in this project.

3.5.2 IGBT and gate driver boards

A Semidriver SKHI 71 unit from Semikron is used as the core of the gate driver board in this project. Each device caters for six IGBT outputs (high and low devices). This gate drive PCB also provide a facility for monitoring the DC link voltage, over-voltage trip, device temperature indication and over-temperature trip facility.

For this project, an IGBT module (Skiip 24ACC12T4V10) with six input devices, a thermistor and six output devices has been selected. This is designed to be used as a controlled input rectifier and output inverter but in this application, it has been used as a three-phase MASRM converter (Asymmetric half-bridge). For the MASRM application, two devices in each phase are never switched and only their antiparallel diodes are used.

The use of a one leg from the input bridge and one leg from the output bridge of the 24ACC12T4V10 enables us to optimise the usage of the on-board devices as the devices in the input and output bridges of the 24ACC12T4V10 module are not the same. Figure 3.6 (a) show the default device arrangement in the IGBT module and Figure 3.6 (b) shows the device arrangement for the 3-phase asymmetric half-bridge converter. The simplified layout of the gate drive board and its main functions are included in Appendix B.

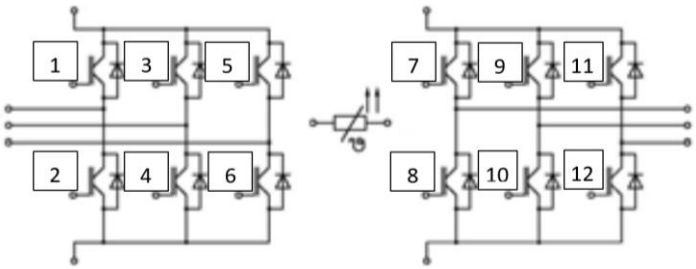

(a)

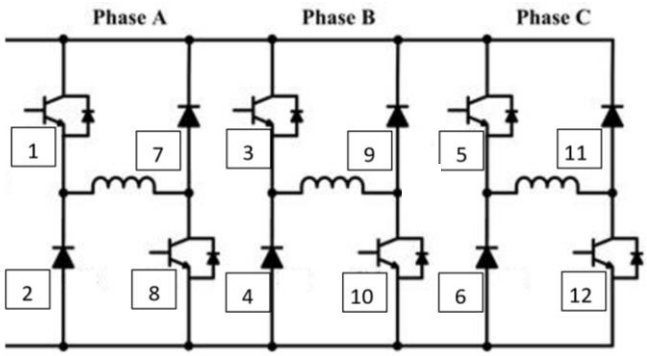

(b)

Figure 3.6: Device arrangements for (a) Skiip24ACC12T4V10 (b) Three - Phase ASHB

3.5.3 F28377D General Control Board

The multi-core processors are useful in this project because control of the MASRM drive have several concurrent tasks. It involves phase current, phase voltage, temperature, device faults and rotor position feedback sensing, fault detection, phase windings energization signals, control algorithm and GUI. Different tasks can be assigned to different cores. Although the F28377D is described as a dual-core processor, it has four processing units on the chip. Each of the two CPUs has an associated Control Law Accelerator (CLA). The CLA is a 32-bit, floating-point processing unit with the same clock frequency as the CPU. So, in terms of computational capability it is equal to the CPU. In addition, each CPU within the F28377D also contains another two computational accelerators in the TMU (Trigonometric Maths Unit) and the VCU (Viterbi, Complex Maths Unit). These units speed up various numerical calculations. The speed enhancements provided by these accelerators are invoked automatically by the C compiler and so do not require any consideration when writing code. In this project, control software is developed to distribute computational load between the two cores of the F28377D DSP of the GCB. A MATLAB based graphical user interface (GUI) is developed for this project which runs simultaneously with the proposed toque control algorithm software.

3.5.4 MATLAB based GUI code

MATLAB software has pre-defined functions to support the creation of a GUI. In this project a MATLAB GUI interface that has been developed at Newcastle University for the GCB is modified and used for monitoring algorithm execution and providing continuous communications with the target hardware (GCB). The developed GUI interface is shown in

Appendix A. The GUI contains a number of widgets (e.g. pushbutton, popup menu, text box, axis, and slider). On the left there are 3 identical graphical axes which are used to display the data collected in the 8 data store arrays s1 – s8. Each graphical axis has 3 popup menus (coloured red, blue and yellow) which are used to select up to 3 data arrays for simultaneous display on the associated axis.

At the top right there are 4 pushbuttons 'PWM ON' (green), 'PWM OFF' (red), STORE' (yellow), and 'PLOT' (blue) to activate/deactivate the target PWM and store and plot the selected set of acquired data. The GUI interface allows monitoring parameters in real time and also adjusting parameter reference values with the sliders located at the bottom right of the GUI.

The MATLAB GUI communicates with the target (i.e. F28377D GCB) via an RS232 serial interface. As most modern PCs/laptops only have USB serial ports, the target control board has an RS232 to USB converter.

3.6 Summary

Static experimental data and mathematical formulation were used to develop a motor model of the 3-phase magnet assisted switched reluctance drive in this chapter. Furthermore, the methods for creating the simulation and online implementation of the overall MASRM drive have been described in this chapter. Since the MASRM used and the multi-objective control proposed in this research differs from the conventional SRM and control objective, proposed by others, the relative algorithms on torque control, torque-ripple minimization, and sensorless control are different too. This will be described in detail in the following chapters.

CHAPTER 4

RELIABILITY AND COMPLEXITY OF MASRM DRIVE CONTROL

Reliability is of great concern in safety-critical applications like automotive, aerospace, medical and home appliances in which switched reluctance machines are getting more acceptance. Thus, the overall reliability of the machine drive hardware and control software should be ensured. The reliability of hardware has been investigated by many researchers working on the areas of Machine Design and Power Electronic Converter design and, therefore, will not be investigated in this thesis. Although the use of unreliable control could be destructive to the drive system, the reliability of control algorithm, however, has not been paid a lot of attention in the literature. In this chapter, the relationship between, reliability, complexity, and performance of several widely used SRM drive control methods are investigated using theoretical and analytical methods. Experimental verification of the results in this chapter is included in Chapter 5.

The effect of common errors associated with a practical MASRM drive on its control systems' reliability is analyzed. In addition, an examination on the relationship between control system complexity and reliability of MASRM control based on the matric of information flow complexity within the control technique is also presented. Three common SRM control methods namely Hysteresis Current Control, Direct Torque Control, and Torque Sharing based Direct Instantaneous Torque Control are considered and compared.

4.1 Introduction

In the DTC method, the desired resultant torque output is obtained by selecting a stator voltage space vector according to calculated errors of the instantaneous torque and stator flux. DITC method is created by simplifying the DTC method in which only the instantaneous phase torque is directly regulated with no consideration of the stator flux error. A comparison of DITC and DTC is presented in [209]. Linear, cubic, and exponential Torque Sharing Functions (TSFs) are also commonly employed to reduce the torque ripple in SRM drives. This technique predefines online or off-line torque waveform to distribute the desired resultant torque among the phase torques of the SRM first before employing torque control for the phase torques. The merits and limitations of these commonly used methods to control SRM drive are depicted in Table 4.1. This considers the functional structures of a three-phase HCC, a three-phase DTC, and a three-phase TSF-DITC of a MASRM shown in Figure 4.1. As shown in the figure, a conventional HCC has two functional blocks that maintain the resultant current at a specified reference with no consideration of reducing torque ripple [210]. A conventional DTC consists

of seven functions to ensure good torque characteristics over a wide range of operation while in TSF-DITC, the functional modules in DTC are reduced to four with compromising torque ripple reduction performance across the speed range of the machine.

Table 4.1. Comparison of MASRM Control Methods

Technique	**Methodology**	**Advantage**	**Disadvantage**
CCC	The current is controlled by using a hysteresis current controller.	• Simple control structure • Robustness to measurement errors.	• High torque ripple • Poor closed-loop dynamics because only the phase current is regulated
DTC	The desired torque is obtained by using torque and flux estimation with hysteresis controller.	• Low torque ripple • Good performance over a wide range of speed.	• Prior knowledge of machine characteristics is required • Requires multiple control calculations. • Requires high switching frequency
TSF-DITC	A linear or non-linear torque sharing function (online or offline) is designed and used to obtain a desired resultant torque.	• Low torque ripple • Accurate reference torque tracking because torque is following the torque sharing technique.	• Offline design of torque profile is required. • Prior knowledge of machine characteristics is required • Requires high switching frequency

Generally, MASRM drives should ensure a good torque characteristic with high reliability both from hardware and software perspectives. Despite the development of several control methods, SRM drives over the last decade, especially for applications that require a high level of reliability and robustness, the technique of evaluating the reliability and robustness of the control methods remains largely undetermined. Feedback measurement error and system complexity can be the main factors that may result in a fault that leads to failure of the system by studying the reliability of the electric drive's control system. A fault, in this case, can be defined as a defect with an open loop or closed-loop control of the electric drive that has the potential of causing its failure. So, the MASRM drive's control system failure can be defined as the inability of the control system or any of its components to perform a required function according to its specification. Therefore, the objective of this investigation is to study the effect

of errors and structural complexity on reliability and robustness of torque control techniques for MASRM.

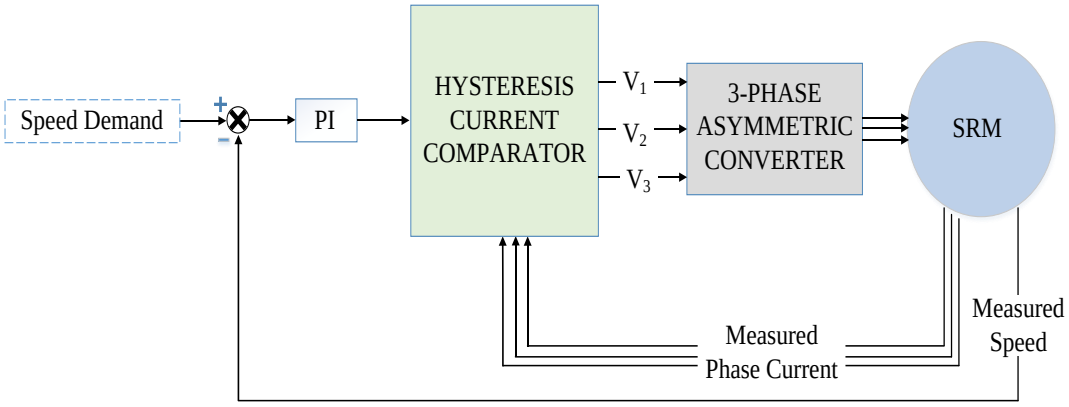

(a) HCC

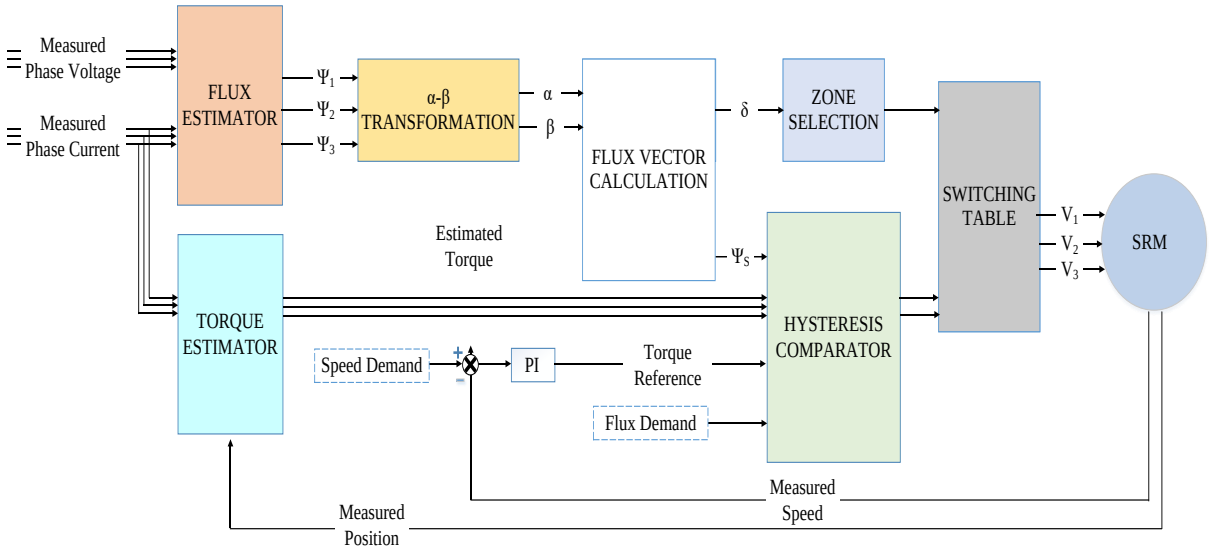

(b) DTC

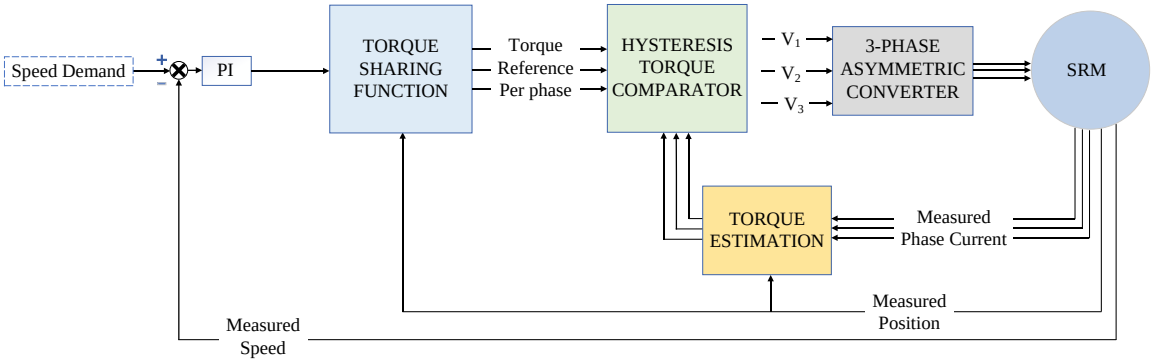

(c) TSF-DITC

Figure 4.1: Control methods of MASRM

4.2 Reliability Analysis of MASRM Control

Having a standard method of quantifying the reliability of electric drive control systems has been an unresolved issue for decades because their failures are time and environment dependent. Nevertheless, factors that can be proportional or inversely proportional to the reliability of control algorithms have been presented by researchers. These factors include Mean Time Between Failure, Flexibility, Accuracy, Robustness, Error Tolerance, Fault Tolerance, Device Dependence, Recoverability, Usability, and Simplicity [211-214]. Control algorithm failures often occur if its functionality differs from the desired one because of errors in the system.

Error-prone systems have a high probability of failure. Furthermore, systems that are error-prone and complex will have a significantly higher probability of failure, thus reducing the overall system reliability.

4.2.1 Error and Noise in SRM Control

As mentioned in Section 4.1, the errors in the control algorithm are key factors that increase its failure rate and make it unreliable. Error components can be introduced into the control algorithm from different factors and the number and magnitude of these error components are proportional to the failure rate of the system [173]. Most errors in the control of MASRM drive are often because of measurement noise, measurement errors and parameter variation within the drive system. These errors affect the torque and flux estimations required in present high-performance SRM control method that can be employed on the MASRM drive. Instantaneous expressions showing the common error components in current measurement, voltage

measurement, rotor position measurement, flux-linkage estimation and torque estimation are as follows:

$$E_i(n) = E_{iO}(k) + E_{iS}(k) + E_{iN}(k) \tag{4.1}$$

$$E_v(k) = E_{vO}(k) + E_{vS}(k) + E_{vN}(k) \tag{4.2}$$

$$E_\theta(k) = E_\omega(k) = E_{TQ}(k) + E_{AQ} \tag{4.3}$$

$$E_\psi(k) = E_i(k) + E_v(k) + E_{TQ}(k) + E_{AQ} + E_R(k) \tag{4.4}$$

where E_i, E_v, E_θ, E_ω, and E_ψ, are the total measurement error in measuring current, voltage, rotor position, and angular speed, and the total flux-linkage error, respectively. E_{iO} and E_{vO} are the current and voltage offset error. E_{iS} and E_{vS} are the current and voltage scaling error. E_{iN} and E_{vN} are the current and voltage signal noise error. E_{TQ} and E_{AQ} are the time and amplitude quantization error. E_R is the error in resistance variation.

Ideally, the instantaneous torque produced by MASRM drive is often estimated from a lookup table $T(\theta, i)$ generated from a static-torque test. Therefore, the effect of both current and rotor position measurement should be considered when analysing the error involved in the torque estimation. Error in the measured current and/or rotor position will impose corresponding error in estimated torque. The following relationship can be used to calculate the resultant error in toque estimation at a given instance 'k':

$$E_T(k) = E_\theta(k)\frac{\partial T(\theta(k),i(k))}{\partial \theta} + E_i(k)\frac{\partial T(\theta(k),i(k))}{\partial i} \tag{4.5}$$

where $E_T(k)$, $\theta(k)$, $i(k)$ and $T(\theta(k), i(k))$ are resultant torque estimation error, actual rotor position, actual phase current and instantaneous torque, respectively. For a given error in current and position measurement, the torque error will be proportional to the sum of the partial derivative of torque with the current and partial derivative of torque with the position.

For the errors mentioned above, it is difficult to quantify the instantaneous error components of the current, voltage, and flux-linkage because their causal factors are system type dependent and time-varying. Hence, random error signal with predefined maximum magnitude can be assumed to represent the total error in these quantities for analysis reasons.

4.2.2 Reliability of SRM Control from the Complexity Perspective

As explained in section 4.1, the complexity of a control technique is one of the key factors that can significantly affect the reliability of MASRM drive. Errors can be introduced into the control algorithm from different factors especially via modules in the system that are depended on measured signals and the effect of the measured signal can be increased as the number of modules in the system that required those signals to function increases thus, the failure rate of the system also increases. Therefore, the less complicated the system, the more reliable it can be [214].

An important metric of structural complexity known as Information flow metric is employed in this study to analyse the effect of system complexity of the MASRM control methods. Henry et al. defined structural complexity in terms of the amount of information flow (IF) between modules in software algorithms [215]. It is proven that it is a suitable and practical basis for measuring the complexity of large systems [215-219]. Thus, the complexity of the MASRM control system can be measured by observing the number of modules and the patterns of communication between the system them. Consequently, an information flow complexity that considers a functional block structure as a module and the interconnection between the modules is proposed and used in this study. The expression for calculating the information flow complexity is defined as:

$$IF = \sum_1^n (fan\_in(n) * fan\_out(n))^2 \quad (4.6)$$

where *n*, *fan_in*, and *fan_out* are defined as the number of modules in a system, the number of input variables passed into the module, and the number of output variables returned from the module, respectively.

The product of *fan_in(n)* and *fan_out(n)* in (4.6) represent the number of possible combinations of the input variables to the output variables of a sub-function (module). While the power of two in the equation as it employed by Belady *et al* in system partitioning is used to represent the non-linear relationship between a specific sub-function and other sub-functions interacting with it [220]. Finally, the measure of the total complexity of the system is obtained by summing up all the sub-functions' '*IFs*'. For example, considering the calculated '*IF*' of HCC, the speed control module has an '*IF(speed) = (2x1)^2 = 4'*, the hysteresis comparator module has an

'*IF(hysteresis) = (4x3)^2 = 144'* therefore, the IF complexity of HCC is *'IF(HCC) = 4 + 144 = 148'*.

The information flow complexity of the three methods is calculated based on the system structures in Figure 4.1 and IF formula expressed in (4.6) to determine the differences in complexity between the control methods, and the results are presented in Table 4.2. It can be observed that the complexity of the control methods is proportional to the number of error component involved in the system. HCC has less complexity hence less prone to error followed by TSF-DITC and finally DTC having the highest complexity and error components. This method of analysis can help to directly reduce the complexity and failure-rate of control algorithms by finding dispensable functions like in the case of reducing DTC to DITC and finding functions affected by measurement errors. Therefore, minimizing computational time and improving reliability.

Table 4.2: Complexity and error components in MASRM drive control methods

METHOD	MODULE	MODULE IF	SYSTEM IF	SOURCES OF ERROR
HCC	SPEED CONTROL	4	148	$E_{CCC}(k) = E_i(k) + E_\omega(k)$ $= E_{iO}(k) + E_{iS}(k) + E_{iN}(k)$ $+ E_{TQ}(k) + E_{AQ}$
	HYSTERESIS COMPARATOR	144		
TSF-DITC	SPEED CONTROL	4	508	$E_{TSF}(k) = E_T(k) + E_\omega(k)$ $= E_{iO}(k) + E_{iS}(k) + E_{iN}(k)$ $+2E_{TQ}(k) + 2E_{AQ}$
	TORQUE SHARING	36		
	HYSTERESIS COMPARATOR	324		
	TORQUE ESTIMATOR	144		
DTC	SPEED CONTROL	4	613	$E_{DTC}(k) = E_\psi(k) + E_T(k) + E_\omega(k)$ $= 2E_{iO}(k) + 2E_{iS}(k) + 2E_{iN}(k)$ $+E_{vO}(k) + E_{vS}(k) + E_{vN}(k)$ $+3E_{TQ}(k) + 3E_{AQ}$
	HYSTERESIS COMPARATOR	64		
	TORQUE ESTIMATION	144		
	FLUX ESTIMATOR	324		
	α-β TRANSFORMATION	36		
	FLUX-VECTOR CALCULATION	4		
	ZONE SELECTION	1		
	SWITCHING TABLE	36		

It can be decided from this findings that complexity and measurement error have a significant negative effect on the reliability of MASRM drive control, and therefore, consideration of reliability and complexity should be involved in the development of torque control algorithms of the MASRM.

4.3 Simulation Analysis of MASRM Control Methods

To analyse the real-time effect of the measurement uncertainties on the control methods, a simulation model of the MASRM drive with the three control algorithms is employed. It is difficult to accurately calculate the measurement uncertainties because it is time and environment dependent. Therefore, white noise with a maximum amplitude of 10% of the terminal measurement is generated as shown in Figure 4.2, to represent the measurement uncertainties common to an electric drive. This error signal is injected to the phase current feedback signals and its effect on the HCC, TSF-DITC and DTC method is shown in Figure 4.3-4.5, respectively. Furthermore, the DTC method requires phase voltage for flux estimation module therefore, the effect of error signals on the measured phase voltage is also shown in Figure 4.6. The significant deviation in the current and voltage can be observed in these figures.

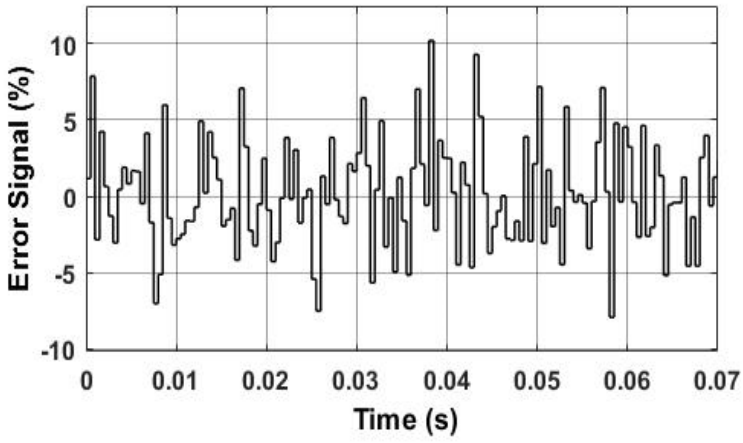

Figure 4.2: 10% error signal injected to measurement terminals

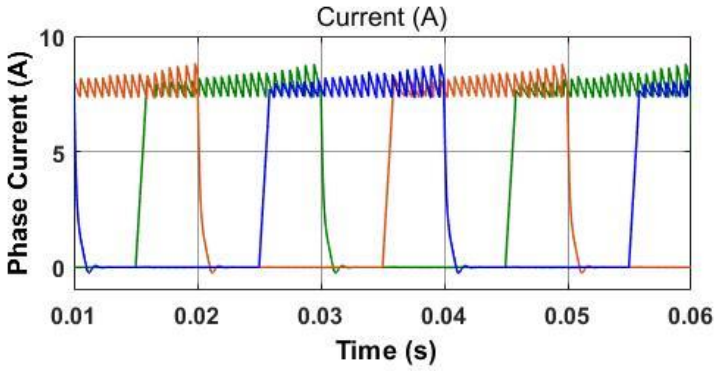

(a)

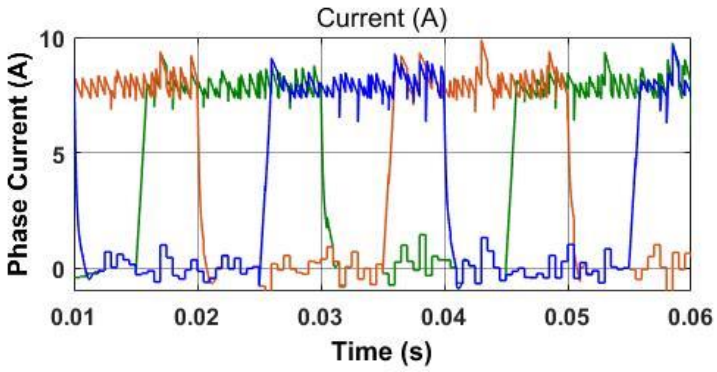

(b)

Figure 4.3: Phase current of HCC method (a) without error (additional noise) (b) with error (additional noise)

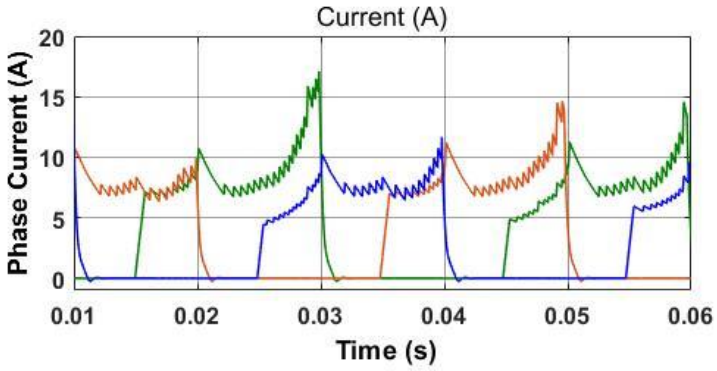

(a)

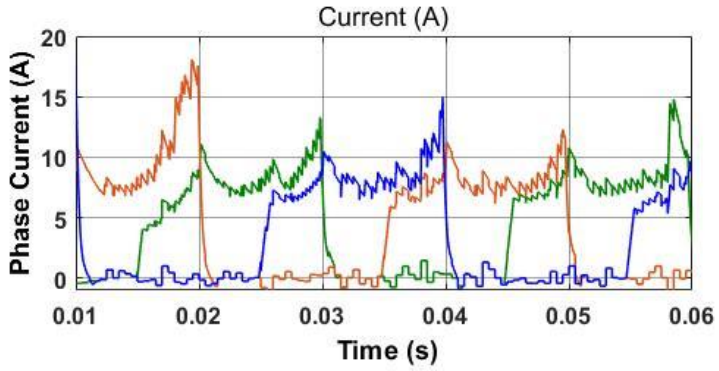

(b)

Figure 4.4: Phase current of TSF-DITC method (a) without error (additional noise) (b) with error (additional noise)

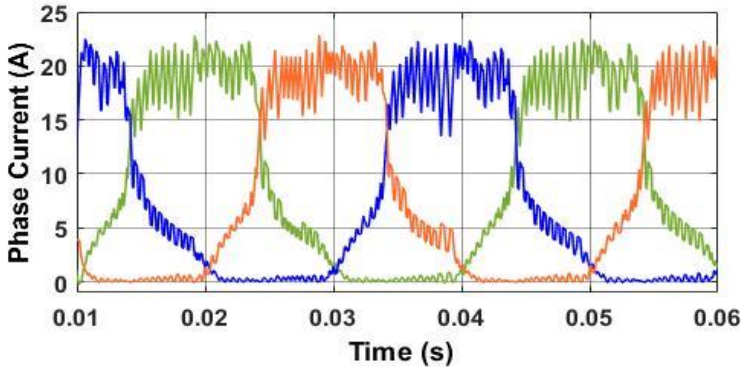

(a)

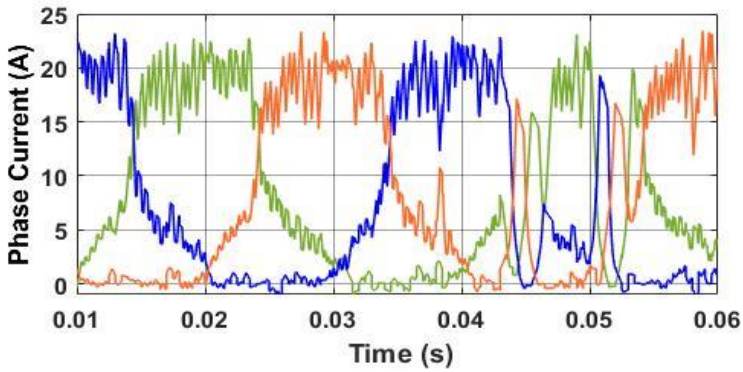

(b)

Figure 4.5: Phase current of DTC method (a) without error (additional noise) (b) with error (additional noise)

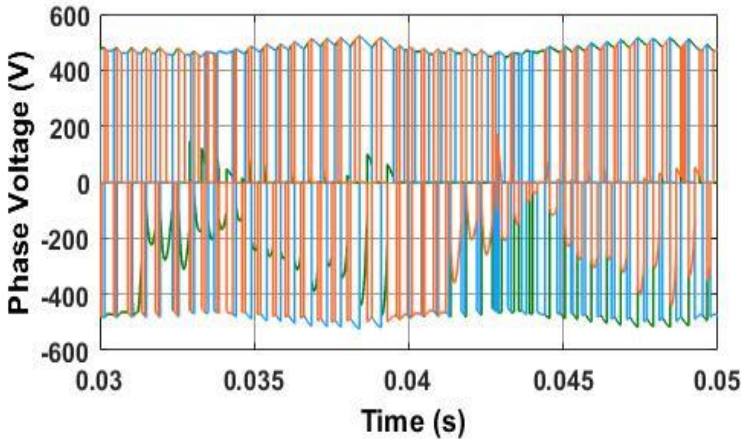

(a)

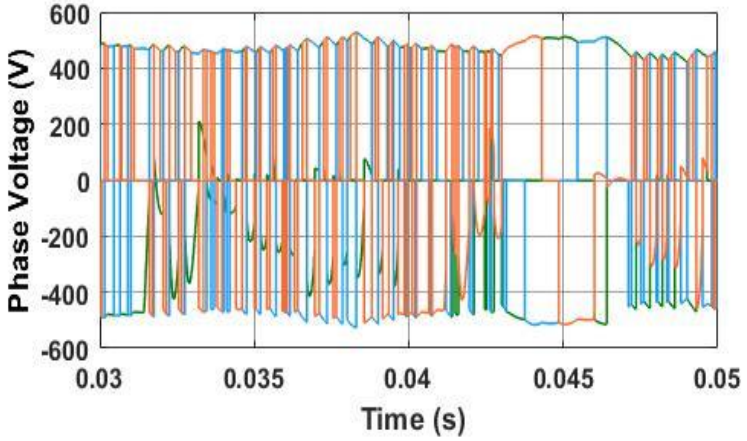

(b)

Figure 4.6: Phase voltage of DTC method (a) without error (additional noise) (b) with error (additional noise)

The comparison of the resultant torque with and without measurement uncertainties of the three control methods for the MASRM drive running at low speed (hysteresis mode) and high speed (pulse mode) are presented in Figures 4.7-4.9. The effect of the introduced simulated error can be observed for the reason that the performance of all the methods is affected at both speed levels. Though, a reliable control system should have a reasonable accuracy under a certain level of uncertainties like the 10% deviation employed in this study. From these results obtained, the HCC method shows better robustness to injected measurement error because the measured feedback is only used by the current hysteresis comparator. By observing the TSF-DITC and DTC results the deviation is high because the feedback signal is used by more than one component of the control methods which increased the effect of the error.

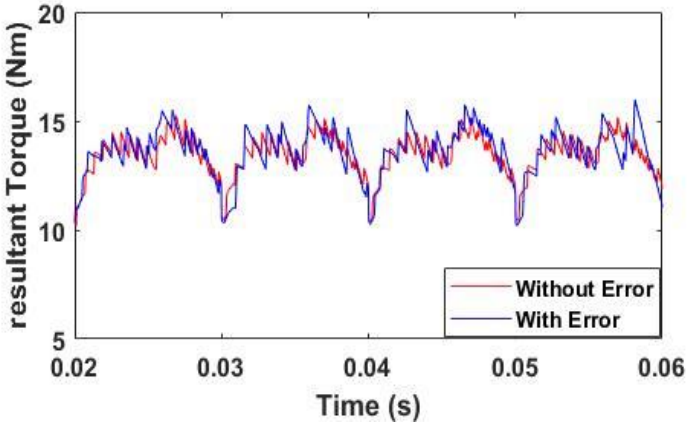

(a)

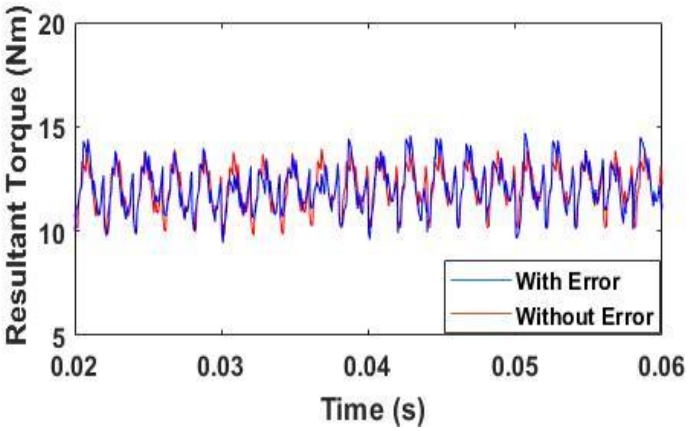

(b)

Figure 4.7: Resultant torque of CCC method at (a)100rpm (b) 500rpm

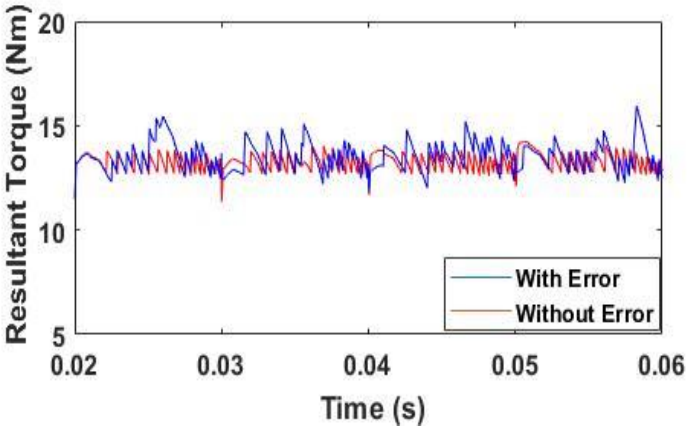

(a)

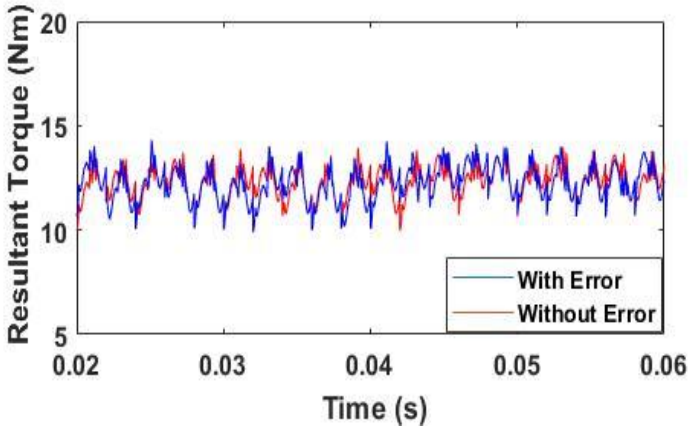

(b)

Figure 4.8: Resultant torque of TSF-DITC method at (a)100rpm (b) 500rpm

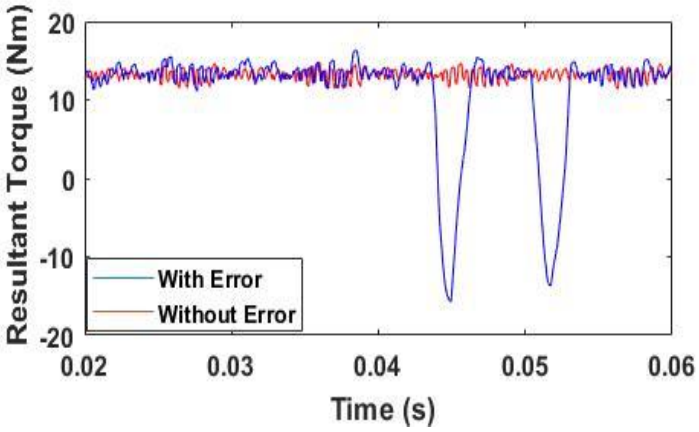

(a)

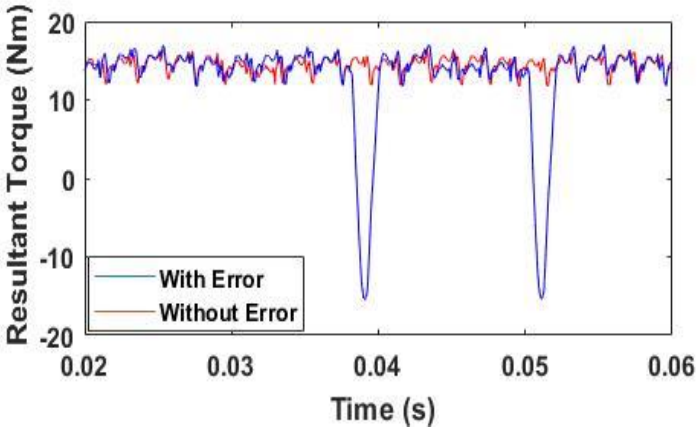

(b)

Figure 4.9: Resultant torque of DTC method at (a)100rpm (b) 500rpm

Table 4.3 summarised the comparison of the normalised peak to peak torque between the HCC method, the TSF-DITC and the DTC method with and without measurement error. Both the TSF-DITC and the DTC methods showed less peak to peak torque as compared to the HCC method at low and base speeds of the electric drive without the error signal injected into the measurement terminals. Nevertheless, injecting the error signal to phase current measurement of the HCC method caused 4% and 8% increase in peak-to-peak torque at100rpm and 500rpm, respectively. For the TSF-DITC method, the injected error caused 12% and 3% increase in peak-to-peak torque at 100rpm and 500rpm, respectively. Moreover, results for the DTC method showed 257% and 216% increase in peak-to-peak torque at100rpm and 500rpm, respectively, which is very large compared to the other two control methods. This is because the DTC algorithm depends on both phase-current and phase-voltage measurements and with the error signal added to each, the flux and torque estimations produced erroneous values, hence, the zone selector can select a wrong switching sequence which can cause torque spikes as depicted in Figure 4.9.

Table 4.3: Normalised Peak to Peak Torque (%)

Methods	**Speed**	**Without Error**	**With Error**
CCC	**100 rpm**	0.38	0.42
	500 rpm	0.35	0.43
TSF-DITC	**100 rpm**	0.21	0.33
	500 rpm	0.33	0.36
DTC	**100 rpm**	0.26	2.83
	500 rpm	0.33	2.49

In summary, the HCC method shows the highest robustness to measurement error in the set of results depicted above. However, the TSF-DITC method achieved superior torque characteristics while maintaining high robustness and reliability. Comparing these three methods, it is clear that increasing the functionality (complexity) of the control method, to improve its torque characteristics, in the case of DTC and TSF-DITC can increases the dependency of the method on the feedback signal hence, reducing its accuracy in the presence of significant measurement uncertainty which can compromise its reliability.

Based on these findings, the Adaptive Quasi Sliding Mode (AQSM) control proposed in this thesis for SRM/MASRM is designed in the next chapter to have the same modular structure as

the TSF-DITC to have similar information flow complexity and error components however, to have improved robustness and reliability.

4.4 Summary

In this chapter, an analysis of the relationship between system structural complexity and reliability of different SRM control methods are presented based on information flow complexity within the control techniques. The results obtained showed that the HCC method has the highest robustness to measurement error followed by the TSF-DITC method then the DTC method. The HCC method can provide high robustness to measurement errors, but it has poor torque ripple reduction capability compared to torque control methods. Consequently, the torque control methods such as TSF-DITC method and DTC method can provide a superior torque ripple reduction. On the other hand, the DTC was found to have less robustness to measurement noise and errors compared to the other two. This is because it has higher structural complexity with more feedback signal dependency, which increased the dependency of its accuracy of the control system to the accuracy of the feedback signal.

CHAPTER 5

ADAPTIVE QUASI-SLIDING MODE CONTROL OF SRM DRIVE

Generally, torque control of switched reluctance drives aims to consistently produce right control action so that the resultant torque generated can track the desired torque as accurate as possible with less ripple.

In this chapter, a novel torque control that is based on a new Adaptive- type of a Quasi-Sliding Mode (AQSM) is developed and implemented to control the torque of magnet-assisted switched reluctance motor drive. The control technique is designed to eliminate the high switching frequency, and high peak current requirements of torque control techniques like the commonly used conventional DITC and DTC methods, which leads to an increase in losses, thermal effects, and sensitivity to measurement errors, in the power devices and also increases the cost of the drive. It is a torque characteristics regulator with included magnitude and rate of change constraints on the control action to reduce the high peak current demand that imposes current stress on the power devices. It also reduces the higher switching frequency commonly required by torque control methods of SRMs. Thus, it reduced the over-rating of the drive components, the energy losses, the thermal effects, and the computational cost. Comparison of the proposed control method with the current chopping control method and conventional DITC with current limiter methods is presented.

Figure 5.1 shows the structure of the proposed AQSM torque control. It involves a torque estimator, a simple torque distributor, and an adaptive- quasi-sliding mode-based torque regulator. The phase voltage, v is the controlled input to the MASRM while the total torque is the output.

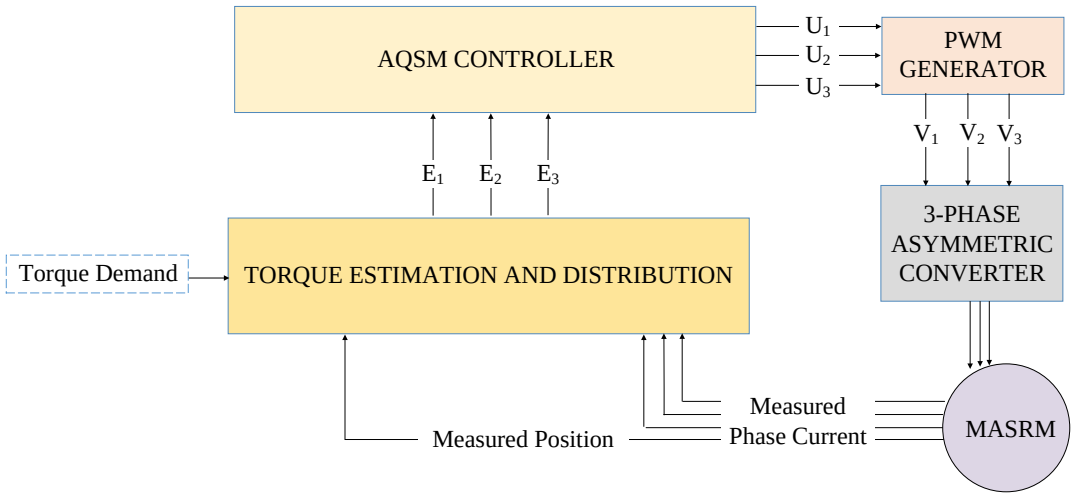

Figure 5.1 Proposed ASQSM based torque control method

5.1 Reliability and Complexity of AQSM Control of MARSM

As mention in Chapter 4, the structural design of the proposed AQSM based torque control method is done taking into consideration the finding on the effect of complexity and measurement error on the control system. It is structured to be as simple as possible with less prone to measurement error without compromise to performance. The reliability of this proposed AQSM based torque controller can be estimated based on the information flow complexity method proposed in Chapter 4 by considering the structure in Figure 5.1 and the findings are presented in Table 5.1.

Table 5.1: Comparison of SRM Control

METHOD	MODULE	MODULE IF	SYSTEM IF	SOURCES OF ERROR
AQSM TORQUE CONTROLLER	SPEED CONTROL	4	458	$E_{AQSM}(k) = E_T(k) + E_\omega(k) = E_{iO}(k) + E_{iS}(k) + E_{iN}(k) + 2E_{TQ}(k) + 2E_{AQ}$
	TORQUE ESTIMATION	144		
	TORQUE DISTRIBUTOR	225		
	AQSM CONTROLLER	81		

As shown in Table 5.1, the proposed AQSM control offers significantly smaller value (better) of information flow complexity compared to the commonly used torque control methods considered in Chapter 4. The calculated value (IF = 458) is lower than that of the TSF-DITC which was found to be the best (IF = 508) from the three analysed control methods in Chapter 4, in spite the improved torque control performance offered by the proposed AQSM control, which will be explained in detail in this Chapter.

5.2 Torque Distribution

It is difficult to directly measure the instantaneous torque produced by an SRM during operation, therefore, it is often estimated from a lookup table $T(i, \theta)$ that can be generated by an experimental or a finite element static test of the machine [221, 222]. A look-up table generated from an experiment is employed in this project because it is more accurate and less computational demanding compared to analytical (equation-based) torque estimation methods. Figure 5.2 shows the static torque characteristics of the MASRM. The phase-currents of the motor are measured together with its rotor position to instantaneously estimate the

corresponding torque of each phase. Linear interpolation is then implemented on the parameters read from the look-up table to improve estimation accuracy.

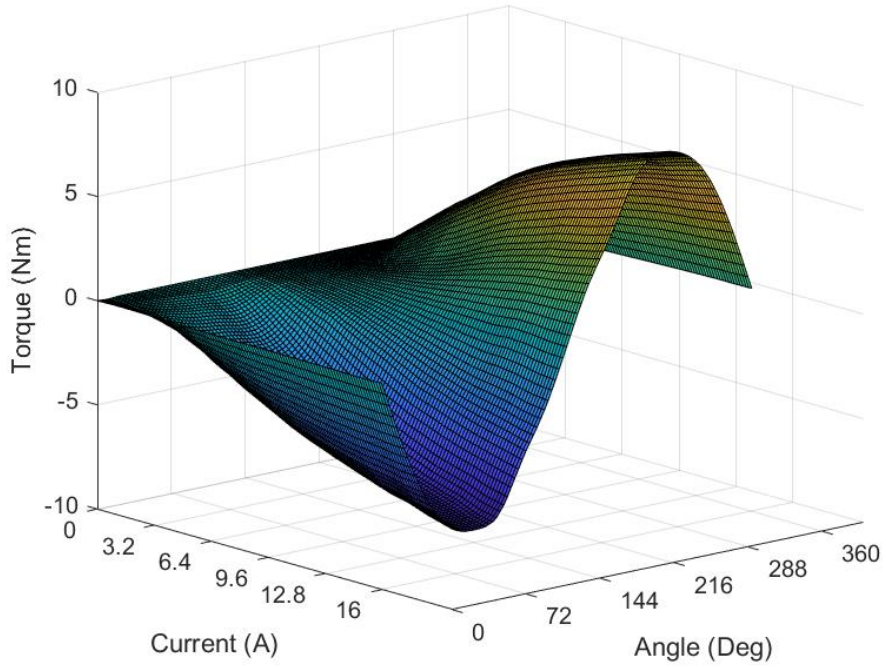

Figure 5.2: Static torque measurement for different levels of current in each phase of MASRM

Several methods can be employed to ensure desired torque tracking in SRM drive with minimized ripple by ensuring right coordination of the individual phase torques during overlapped commutation. Therefore, a phase torque distribution function that needs no off-line torque sharing profile or complex online torque sharing calculation is proposed in this project to reduce computational cost. The following equations are used to obtain a distributed torque reference for each phase by comparing the overlapping phase torques.

$$T_1^*(kt) = \begin{cases} T^*(k) - T_2(k) - T_3(k) & for \ \ \theta_{on} \leq \ \theta_1 \ \leq \ \theta_{off} \\ 0 & for \ \ \theta_{on} > \ \theta_1 > \ \theta_{off} \end{cases} \quad (5.1)$$

$$T_2^*(kt) = \begin{cases} T^*(k) - T_1(k) - T_3(k) & for \ \ \theta_{on} \leq \ \theta_2 \ \leq \ \theta_{off} \\ 0 & for \ \ \theta_{on} > \ \theta_2 \ > \ \theta_{off} \end{cases} \quad (5.2)$$

$$T_3^*(kt) = \begin{cases} T^*(k) - T_1(k) - T_3(k) & for \ \ \theta_{on} \leq \ \theta_3 \ \leq \ \theta_{off} \\ 0 & for \ \ \theta_{on} > \ \theta_3 \ > \ \theta_{off} \end{cases} \quad (5.3)$$

Where T^* is the motor desired resultant torque, T_m is the phase instantaneous torque and T^*_m is the phase reference torque θ_m is the electrical position, m is the phase number, θ_{on} is the turn-on angle, θ_{off} is the conduction angle and t denotes the sampling time the controller. Each phase is compared with the adjacent phases to produce the appropriate reference that will ensure smoothed resultant torque. For example, to obtain an appropriate torque reference for phase 1 at a given instance, the instantaneous torque of phase 2 and phase 3 are subtracted from the desired resultant torque.

5.3 Quasi-Sliding Mode Control

A traditional torque controller uses a hysteresis torque regulator to maintain the output torque within the reference torque. One of the limitations of this method is the generation of large phase-current ripple that produces phase-torque ripple. This limitation can be reduced by reducing the hysteresis band, hence, increasing the switching frequency requirement of the controller which often increases switching losses, thermal effects, and rating of the power devices. Another limitation of traditional torque control method is its tendency to demand high current at aligned and unaligned rotor position of SRMs. This is due to the inherent low inductance gradient (high saturation) of SRMs within these regions. The high current demand requires over-rating of the power devices or it will impose current stress on the phase windings and power electronics of the drive if not limited thus compromising the system reliability.

Use of conventional sliding mode control to reduce torque ripple in switched reluctance motor have been recently studied. A flux-linkage controller based on a sliding mode method with integral compensation (SM-I) is proposed in [223] to minimize the torque ripple of an SRM. A proportion–integration is added to the conventional sliding mode control to compensate for its chattering at steady state. The proportion–integration control properties are utilised at steady-state and that of conventional sliding mode control at the transient state of the nonlinear SRM. However, the fixed parameters of the proportion–integration control and high saturation of the MSSRM can limit the performance of the method to a certain range or condition of operation for this. Furthermore, the flux estimation method employed in this method can be vulnerable to measurement errors because the high inductance of the MASRM explained in Chapter 3. A fixed-switching-frequency model-based sliding mode current controller with an integral switching surface for switched reluctance motor drives is proposed in [224]. The controller

developed required a complex model of switched reluctance motor, considering the effects of magnetic saturation and mutual coupling.

A discrete sliding mode control, which is also known as Quasi Sliding Mode (QSM) control, is a promising digital control method for regulating uncertain, nonlinear, time-varying systems like a MASRM. Its main concept is to select a correct hyperspace in the state space to confine the motion of the representative point (the system' state) within it. The position, direction and outline of the hyperspace determine the dynamic behaviour of the control system. A sliding variable '*x(t)'* analogous to a sliding hyperplane in the space is used to determine the control action at every instance. Its value is either zero, positive or negative if the representative point is on, below or above the selected sliding hyperplane, respectively. Furthermore, its magnitude is relative to its position from the hyperplane [225]. Generally. a sliding mode controller is designed based on the following:

i. Reaching phase: The controller will ensure the representative point will eventually reach the sliding hyperplane in a finite time.

ii. Sliding phase: The controller will maintain the representative point within the sliding hyperplane.

Figure 5.3 depicts the concept of sliding mode control. An appropriate reaching law for a specific control problem that will ensure convergence of the '*x(t)'* to zero is developed. The reaching law calculates the next desired value of the '*x(t)'* based on its present value.

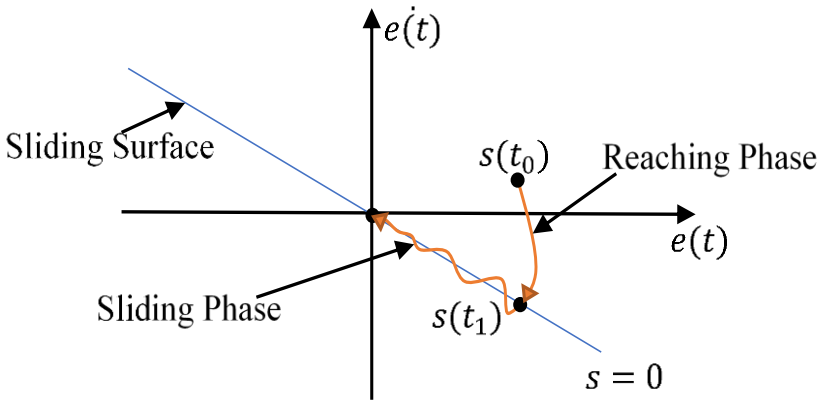

Figure 5.3: Concept of the sliding mode control

The reaching law based technique is one of the most employed methods for design sliding mode control because there is no need to prove the sliding mode is ensured and the convergence of the state to the hypersurface is directly taking into account in the design of the reaching law. The two reaching law-based sliding mode control design for the discrete-time control systems named switching and non-switching reaching type reaching laws are described in the following sections.

5.3.1 Switching Type Reaching Law for QSM Control

Let the reference (demand) state vector x_r and the closed-loop error can be represented as $e(k) = x_r - x(k)$. Therefore, the sliding variable can be expressed as:

$$\mathrm{s}(k) = \delta e(k) \tag{5.4}$$

where δ is a pre-calculated 1xn vector which ensures the desired performance of the closed-loop system.

The reaching law can be defined as in [226]:

$$s(k+1) = (1 - Q)s(k) - \varepsilon(\mathrm{sgn[s(k)]}) \tag{5.5}$$

where $Q \in (0, 1)$ and $\varepsilon > 0$ are constant real numbers. sgn[s(k)] is negative if $s(k) \leq 0$ and positive if $s(k) > 0$ The first terms in (5.5) is used to reduce the inherent chattering of sliding mode while the second term is used to set the rate of change of the sliding variable in proportion to the variable, hence, as the sliding variable significantly increases, its rate of change tends to infinity. This is a disadvantage to the reaching law presented in [226] that makes it impractical to implement in systems with limited input and limited rate of change of output, because the control signal and state variable can easily reach unacceptable values at the start of the control process or when the sliding variable is small.

Improvement have been acheived by modifying the first term of the reaching law as shown below [227]:

$$s(k+1) = (1 - Q[s(k)])s(k) - \varepsilon(sgn[s(k)]) \tag{5.6}$$

where,

$$Q[s(k)] = \frac{s_0}{|s(k)|+s_0} \tag{5.7}$$

The value of $Q[s(k)]$ increases as $|s(k)|$ decreases and the term s_0 is a positive real number. This specifies the rate of change of the sliding variable scaled by a non-linear term of choice with this, a maximum rate of change of sliding variable that results in bounded input and state variables can be imposed on the control process.

Now considering a perturbed discrete-time system in [226]:

$$x(k+1) = Ax(k) + \emptyset[x(k)] + Bu(k) + \alpha(k) \tag{5.8}$$

where $x(k)$ the state vector, A is the state matrix, B is the input matrix, $u(k)$ is the input, $\emptyset[x(k)]$ is a non-linear function denoting the model uncertainties and $\alpha(k)$ represent an external disturbance.

Equation (5.4) and (5.8) are used to calculate (5.9) which will ensure the input signal $u(k)$ satisfies (5.6).

$$u(k+1) = (1 - Q[s(k)])s(k) - \varepsilon(sgn[s(k)])$$

$$-\tilde{S}(k) - \tilde{F}(k) + S_1 + F_1 - (S_2 + F_2)sgn[s(k)] \tag{5.9}$$

where $\tilde{S}(k)$ and $\tilde{F}(k)$ represent the total effect of model uncertainty and external disturbance on the evolution of the switching variable, respectively. This variable can be defined as follows:

$$\tilde{S}(k) = \widetilde{S}[x(k)] = \delta(\emptyset[x(k)]) \tag{5.10}$$

$$\tilde{F}(k) = \delta[\alpha(k)] \tag{5.11}$$

S_1 and F_1 are the mean values of $\tilde{S}(k)$ and $\tilde{F}(k)$ while S_2 and F_2 are the maximum deviation of $\tilde{S}(k)$ and $\tilde{F}(k)$ from nominal values, respectively, and are expressed as follows:

$$\begin{aligned} S_1 &= \frac{(S_U+S_L)}{2}, \quad F_1 = \frac{(F_U+F_L)}{2} \\ S_2 &= \frac{(S_U-S_L)}{2}, \quad F_2 = \frac{(F_U-F_L)}{2} \end{aligned} \tag{5.12}$$

where S_U and S_L are upper and lower bounds of $\tilde{S}$, and F_U and F_L are upper and lower bounds of $\tilde{F}$.

Now, the control signal $u(k)$ at any instance, k can be calculated from (5.8) and (5.9) as follows:

$$u(k) = -(\delta B)^{-1}\{\{1 - Q[s(k)]\}s(k) - \varepsilon(sgn[s(k)])$$

$$+\delta Ax(k) - \delta x_r + S_1 + F_1 - (S_2 + F_2)sgn[s(k)] \quad (5.13)$$

The above equation (5.13) can be directly applied to control a discrete-time perturbed system by properly selecting the controllers' variables.

5.3.2 Non-Switching Type Reaching Law for QSM Control

Another quasi-sliding mode technique known as non-switching type reaching law for discrete-time sliding mode control that describes discrete-time sliding mode as a motion of a system was derived in [228], such that its states always remains within a specified band around the sliding hyperplane. In the non-switching reaching law, the system trajectory is only required to stay within the predefined band without the need for it to cross the sliding hyperplane in each control cycle as it is the case in the switching reaching law. The non-switching reaching law for a perturbed system stated in (5.8) can be expressed as follows:

$$s(k+1) = (1 - Q[s(k)])s(k) - \varepsilon([s(k)]) - \tilde{S}(k) - \tilde{F}(k) + S_1 + F_1 \quad (5.14)$$

where $Q[s(k)]$ is defined as in (5.7) and $s_0 > S_2 + F_2$ is a constant which should be chosen to balance the magnitude of the input signal produced by the controller and the robustness of the closed-loop system. The main advantage of this reaching law is that it generates no chattering because it does not have discontinues terms. It can also ensure faster convergence and better robustness because it has a variable decrease rate of change of sliding variable with the same limitations of the rate of change of the output. Hence, it provides more efficient use of the system's input within an imposed constraint.

The non-switching reaching law results in a control signal as expressed below:

$$u(k) = -(\delta B)^{-1}\{1 - Q[s(k)]\}s(k) + \delta Ax(k) - \delta x_r + S_1 + F_1 \quad (5.15)$$

It can be observed from (5.7) and (5.15) that the derived non-switching reaching law has a limited rate of change of the sliding variable which is always smaller than $s_0 + S_2 + F_2$.

5.4 Proposed Adaptive Quasi-Sliding Mode Torque Control

As defined above, a non-switching based QSM control is described as a motion of the system that ensures asymptotical convergence of the control error to a given vicinity of the sliding hyperplane by eliminating the requirement of crossing the hypersurface in every successive sample time of the controller, assuming the uncertainties of model parameters and external disturbances satisfied the matching conditions. The non-switching law has the advantage of not generating chattering in control action which can reduce current ripples hence reduce torque ripple compared to the conventional sliding mode and hysteresis torque controls. While a switching reaching law based QSM control was also defined as the one which once its representative point has crossed the switching hyperplane the first time, it crosses it again in every successive sampling period with the size of each successive zigzagging step being fixed. However, both methods require highly complex model computation of the system, especially with the high nonlinearity of the MASRM.

In this approach, a new adaptive quasi-sliding mode control is derived based on the principles of non-switching QSM control and proportional control to improve the torque characteristics of MASRM drive while reducing the limitations of the commonly employed torque control methods such as high current and high switching frequency demands. Another consideration of the controller design is to significantly reduce the computational cost and the errors due to approximations from the highly nonlinear analytical model of MASRM compared to other nonlinear control methods. The main ideas of AQSM can be discussed in the following sub-sections.

5.4.1 Base Function

A control variable (input signal) '$u(k)$'at an instance 'k', is required to be generated such that the process variable (output) of the system '*PV(k)'* tracks the setpoint (demanded output) '*SP*(k)', that is the difference between them asymptotically converges to zero. Let the dynamic difference be defined as a dynamic error represented in (1).

$$E(k) = SP(\mathrm{k}) - PV(k) \tag{5.16}$$

Then the future control variable is expressed as a prespecified proportional function as shown in (2) below.

$$u(k+1) = \beta(\mathrm{E(k)}) \tag{5.17}$$

where β is a proportional gain that that should be chosen to apply the right error correction signal as fast as practicable but avoids instability. The value of '$u(k)$' is either zero, positive or negative if its representative point is within, below or above the desired setpoint, respectively. Whilst its magnitude is relative to its position from the set point.

5.4.2 Constraint Handling

A nonlinear control function based on the concept of the non-switching quasi-sliding mode is incorporated to the control law in (5.17) to avoid unacceptable values of the control signal and state variable during the control process. Hence, the future manipulated variable can be restructured as the prespecified nonlinear function as shown in (5.18), such that the system trajectory is only required to stay within a predefined band.

$$u(k+1) = \mathrm{P[E(k)]}(\delta[E(k)]) \tag{5.18}$$

'$P[E(k)]$' is a non-linear term defined in (5.19) which specifies the rate of change of the control action to ensure that the maximum rate of change of the control action keeps the system state variables within desired limits. That is, it leads to the variable decrease rate of the control input and the state variable.

$$P[E(k)] = \left(\frac{e_0}{|\delta[\mathrm{E(k)}]| + e_0}\right) \tag{5.19}$$

where, '$e_0 > 0$' is a constant chosen to optimize the closed-loop control system. It enables obtaining a satisfactory compromise between the magnitude of the input signal generated by the controller and the robustness of the system designed according to (5.18) which is always smaller than e_0 as shown in Figure 5.4. This improved control law can provide more efficient use of the system's input within an imposed constraint.

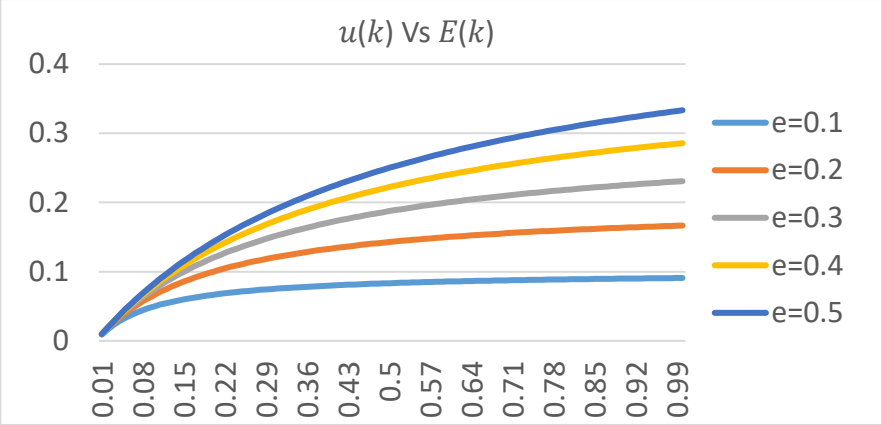

Figure 5.4. Change of control signal $u(k)$ with the change in error $E(k)$ for different values of e_0 .

5.4.3 Design of AQSM Torque Controller

The new ASQM developed in the previous section is proposed for the torque control of MASRM mainly because of its simplicity, and robustness in handling system nonlinearity and constraints.

The control input '$u(k)$' is required to be generated such that the output torque of each phase '$T_m(k)$' tracks its reference torque '$T^*{}_m$(k)'. Considering (5.16), let the torque dynamic error be defined as follows:

$$e_{T_m}(k) = T^*{}_m(\mathrm{k}) - T_m(k) \tag{5.20}$$

The value of the error can be normalized is in (5.21) to make the control signal be within -1 to 1 to simplify the of the PWM control that will be explained in the next section.

$$E_{T_m}(k) = e_{T_m}(k)/T_r \quad . \tag{5.21}$$

where T_r denotes the rated torque of the MASRM.

Therefore, the future control variables can be expressed as a prespecified proportional function as shown in (5.22) based on (5.19). Where '$P\left[E_{T_m}(k)\right]$' is calculated as in (5.18).

$$U(k+1)_m = P\left[E_{T_m}(k)\right](\beta[E_{T_m}(k)]) \tag{5.22}.$$

The control law proposed in (5.22) for the MASRM torque regulation utilizes the benefits from the proposed non-switching QSM advantages. It dynamically specifies the control signal rate of change based on the non-linear term $P\left[E_{T_m}(k)\right]$ from (5.19) which decreases when the

absolute value of $E_{T_m}(k)$ increases. Hence, the desired rate of change of the control signal that leads to a bounded switching frequency requirement and bounded phase current of the MASRM drive can be achieved. Specifically, around the aligned and unaligned inductance of the MASRM machine because both rapidly increase due inherent inductance profile of the SRM which was discussed in Chapter 3.

The new torque control proposed in this study for the MASRM is an adaptive quasi-sliding mode controller that dynamically utilizes both the proportional functional control and non-switching quasi-sliding mode control.

The torque regulator operates according to (5.22) if the phase current $i_m(k)$ is not within a selected allowable band 'ε' and it operates as a proportional controller if $i_m(k)$ is within the band. Figure 5.5 depicts the operation of the AQSM controller. The value of ε identifies whether the controller should maintain its operation in the proportional function type or switch to the nonlinear function type (non-switching QSM) to reduce the rapid input signal (control variable) rate of change that leads to high phase current (state variable of the system) and switching frequency in the drive. Therefore, to produce desired torque characteristics with mentioned constraints, the following control law is proposed.

$$U_m(k+1) = \begin{cases} \delta[E_{T_m}(k)] & |i_m(k)| \leq \varepsilon \\ P\left[E_{T_m}(k)\right](\delta[E_{T_m}(k)]) & |i_m(k)| > \varepsilon \end{cases} \tag{5.23}$$

Where the values of β, e_0 and ε are needed to be appropriately selected to achieve the desired control action.

In brief, the AQSM torque control technique results in a control action that is not aggressive because of large absolute values of $E_T(k)$ but can still provide enough control effort to track the demanded torque and reduce the torque ripple as well. β, e_0 and ε are chosen (using trial and error) to be 1.5, 1.1, and 5.4, respectively to ensure the desired performance of the closed-loop system.

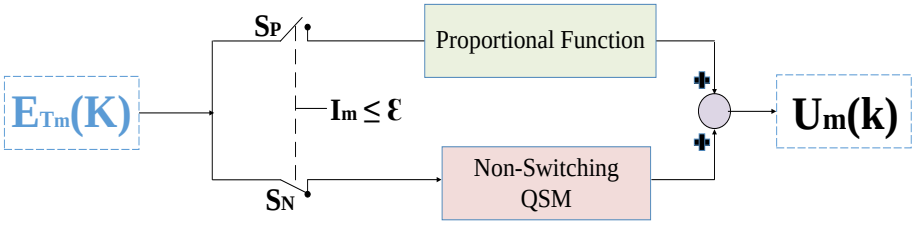

Figure 5.5. Schematic of adaptive control.

5.5 Converter Switching Condition

Asymmetric half-bridge converters are commonly used for SRM drives because of its high control flexibility and low switching loses. Figure 5.6 shows the three switching states of the converter which are on-state, freewheeling-state and off- state. The switching condition for the direct instantaneous torque controller is developed to operate at soft chopping and hard chopping depending on the value of the control variable, with approximately an 80% soft chopping operation to reduce loses and stress in the converter. To handle the required degree of freedom of the QSM, a PWM control is combined with the AQSM based torque control. Each phase of the machine is energized at a carrier frequency of 20 kHz.

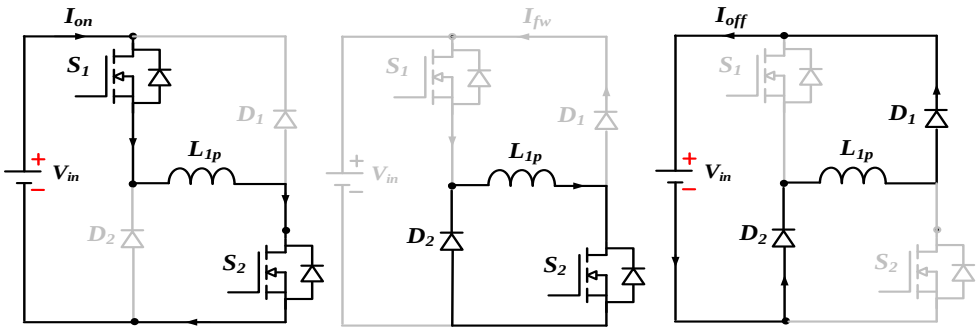

Figure 5.6 Switching state of asymmetric half-bridge converter. (a) on-state. (b) freewheeling State. (c) off-state.

These three operational states can be realized with hard chopping or soft chopping. In hard chopping, a PWM signal with duty cycle D_m is simultaneously applied on both converter switches (S_1 and S_2) of phase m. It is normally used when a high rate of change of phase current is required. However, in soft chopping, one of the switches (say S_1) is controlled by a PWM signal with duty cycle D_m ($D_{m1} = D_m$) while the other switch is kept "on" (D_{m2} =1) or "off" (D_{m2} =0) to limit the rate of change of current and the switching losses. Figure 5.7 shows a simplified flowchart of the converter switching based on the control signal $U_m(k)$. As shown,

soft chopping is utilized when the magnitude of $U_m(k)$ is less than unity while the hard shopping is used when the magnitude of $U_m(k)$ is greater than or equals to unity.

Table 5.2 shows how the effective phase voltage is calculated per switching cycle based on the value $D_m(k)$ obtained from Fig. 6. Where, V_m, V_{on}, V_{fw}, and V_{off} are the effective phase voltage, on-state voltage, freewheeling-state voltage, and off-state voltage, respectively. To increase a phase torque (if $U_m(k) > 0$), the phase is set to on-state with a duty cycle equals to $|U_m(k)|$ (or $D_m(k)$) and then turned into the freewheeling-state for the remaining part of the switching cycle. To decrease a phase torque (if $U_m(k) < 0$), the phase is set to off-state for a period proportional to $|U_m(k)|$ (or 1-$D_m(k)$) and then turned into the freewheeling-state. That is the polarity of $U_m(k)$ determines the polarity phase voltage while its magnitude determines the duty cycle.

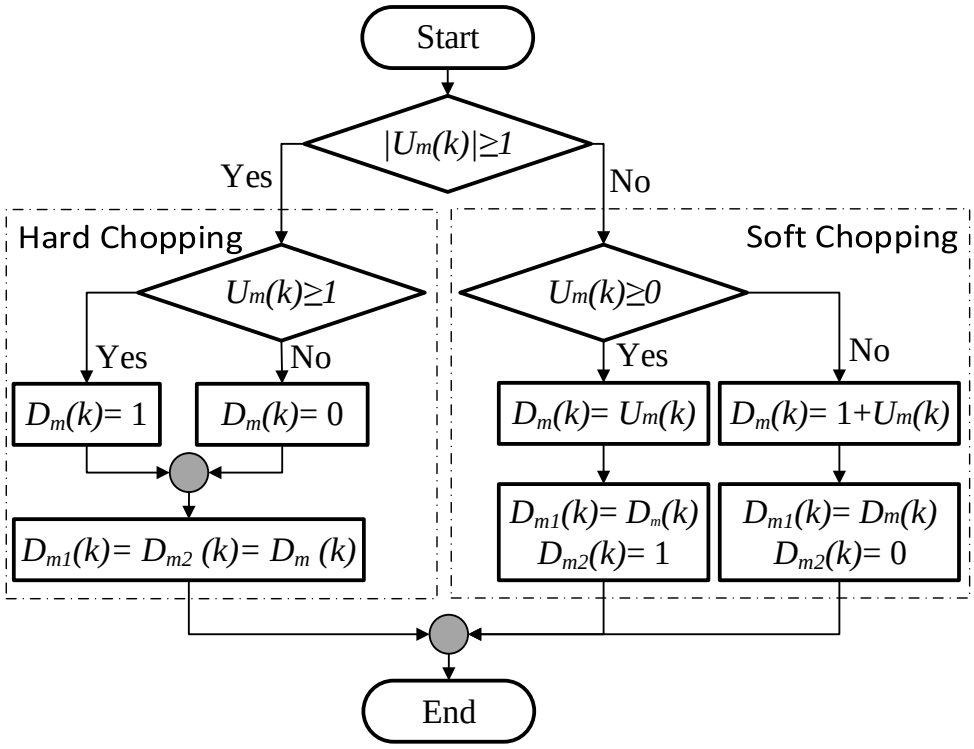

Figure 5.7. Flowchart of voltage demand

Table 5.2: Converter Switching Condition

Control Demand	**D_{m1}**	**D_{m2}**	**Chopping**	**Phase Voltage Per Cycle (V_m)**
($U_m(k) \geq +1$)	1	1	Hard	V_{on}
($0 < U_m(k) < +1$)	D_m	1	Soft	$D_m(k)\ V_{on} + (1 - D_m(k))\ V_{fw}$
($U_m(k) = 0$)	D_m	1	Soft	V_{fw}
($0 > U_m(k) > -1$)	D_m	0	Soft	$(1 - D_m(k))\ V_{off} + D_m(k)\ V_{fw}$
($U_m(k) \leq -1$)	0	0	Hard	V_{off}

5.6 Simulation Results

Analysis and comparison of the proposed method with other commonly employed control method is done in this section. A closed-loop Simulink model of the MASRM drive has been developed to investigate the performance of the proposed controller as described in Chapter 3. Simulations at several operation conditions were carried out. The phase current, phase torque and resultant torque of the MASRM drive controlled by an HCC method, a DITC method, and the proposed adaptive quasi-sliding mode method operated at constant torque speed region, constant power speed region and natural speed region of the test MASRM under a different load torque are presented in Figure 5.8 to Figure 5.10.

For these tests, the DC link voltage and the maximum allowable current for the test MASRM drive are set at 240Vdc and 7A respectively. As mentioned earlier, one of the limitations of the DITC method is that it generates a current spike and use high switching frequency at the beginning and end of every phase conduction period. Therefore, an inner current limiting control loop is added to the DITC control with the peak value of the phase limited to 6.5A with a hysteresis band of 0.4Nm. It worth mentioning this added current limiter loop to the DITC method increases its computation cost and limits its capability of torque regulation but it is necessary for overcurrent protection. For the HCC, the current demand is set at 5A with a hysteresis band of 0.2A. A constant switching frequency of 20 kHz is considered in all the methods for a fair comparison.

It can be noticed from the comparison of the results, that all the three control methods produced good results in tracking the desired reference. A smoother torque is achieved by the proposed method (Figure 5.10) at a reference torque of 8 Nm. Which is due to the absence of torque ripple arisen from the hysteresis type switching in HCC and DITC methods, which can be noticed in Figures 5.8 and 5.9. The torque ripples generated from phase commutation is significantly reduced in the two torque two control methods. Figure 5.11 shows the comparison of the resultant torque of the three control techniques at different speed.

In the traditional DITC and DTC techniques, the control signal needs to change very fast when the dynamic error '$E_{T_m}(k)$' is equal to the upper or lower limits of the hysteresis, and the narrower the hysteresis band of the torque controller the better its torque ripple reduction. However, if a very narrow band is selected for better performance, the control drive needs to switch very fast to cope, especially in region where '$E_{T_m}(k)$' is very large Switching frequency

can reach up to a maximum of 500kHz, which is almost impractical to implement with regards to computational cost and thermal effects on the drive [229]. Commonly a switching frequency of 35kHz and above is employed for reasonable performance because lower than that can have a significant effect on the controller performance and robustness. As mentioned earlier, for a fair comparison in this study, the same switching frequency of 20kHz and the same peak current limit of 6.5A is employed in all the three methods. It was observed that the switching frequency limitation together with the added current limiter control loop in the DITC leads to its irregular current shapes and less performance compared to the proposed AQSM based method, which can be seen in the simulation and experimental results.

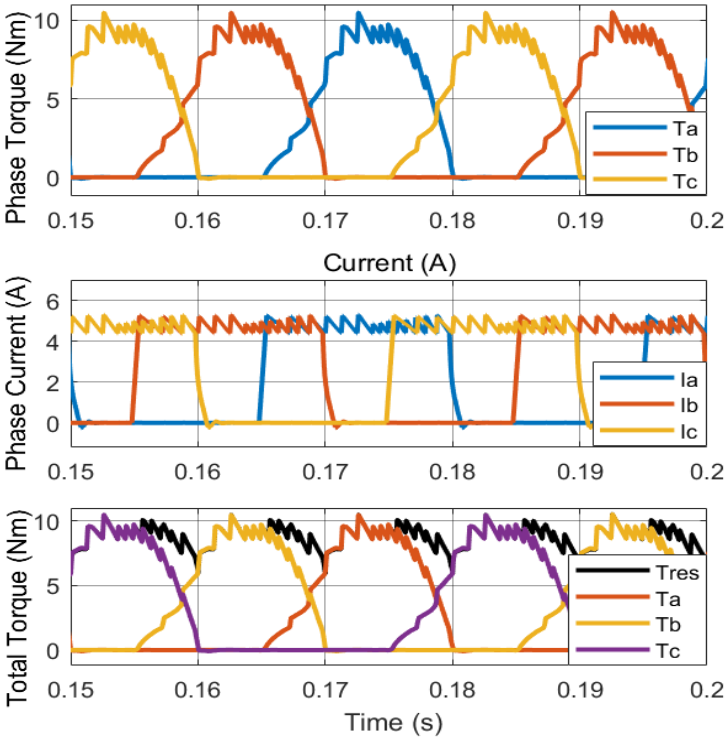

(a)

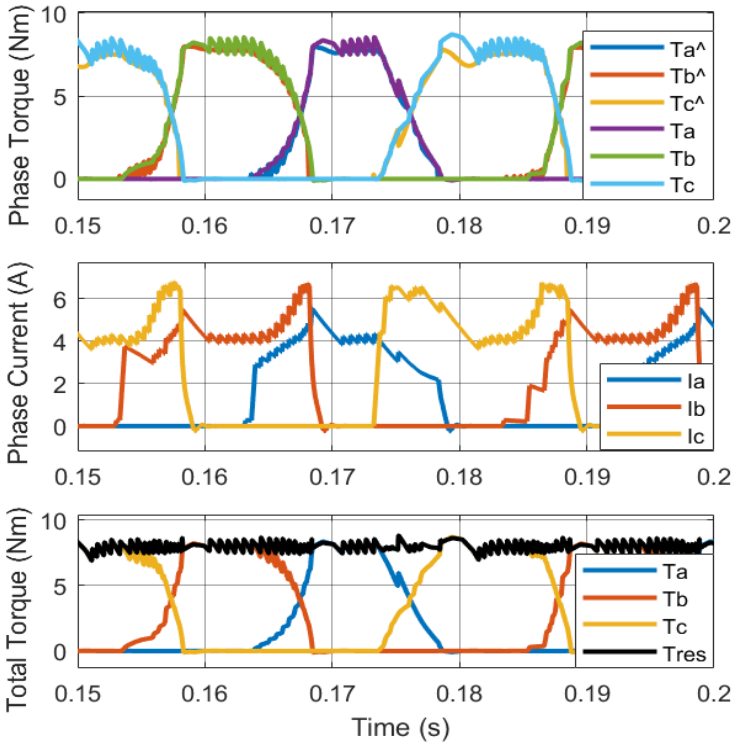

(b)

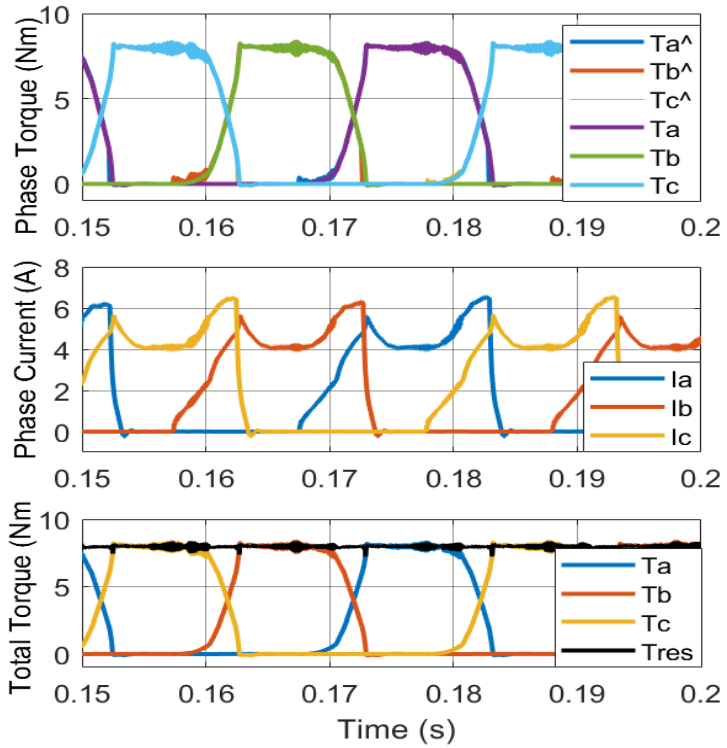

(c)

Figure 5.8 Phase current, phase torque and resultant torque of the methods a at 100 rpm with 8Nm load torque (a) HCC (b) DITC (c) AQSM

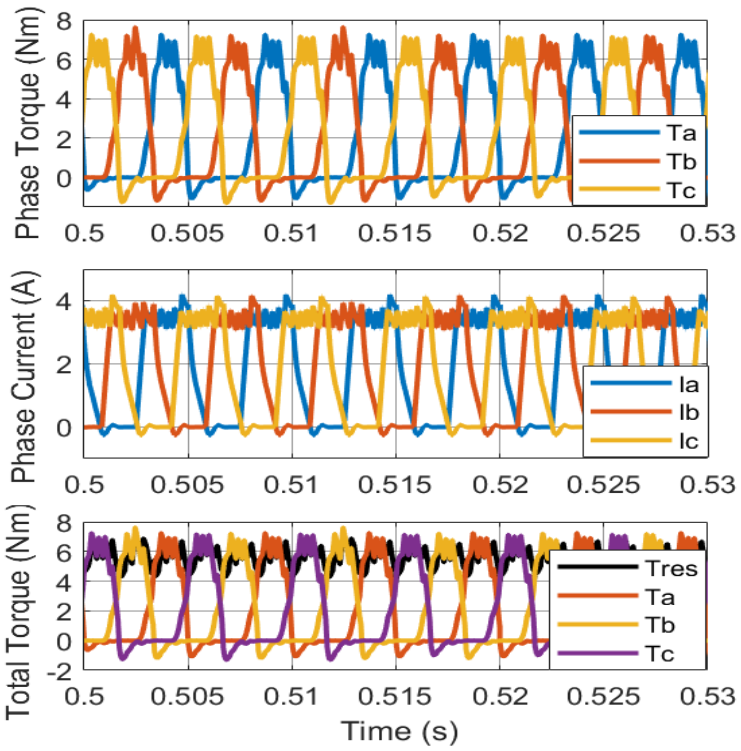
Phase Torque (Nm)
Ta
Tb
Tc
Phase Current (A)
Ia
Ib
Ic
Total Torque (Nm)
Tres
Ta
Tb
Tc
Time (s)

(a)

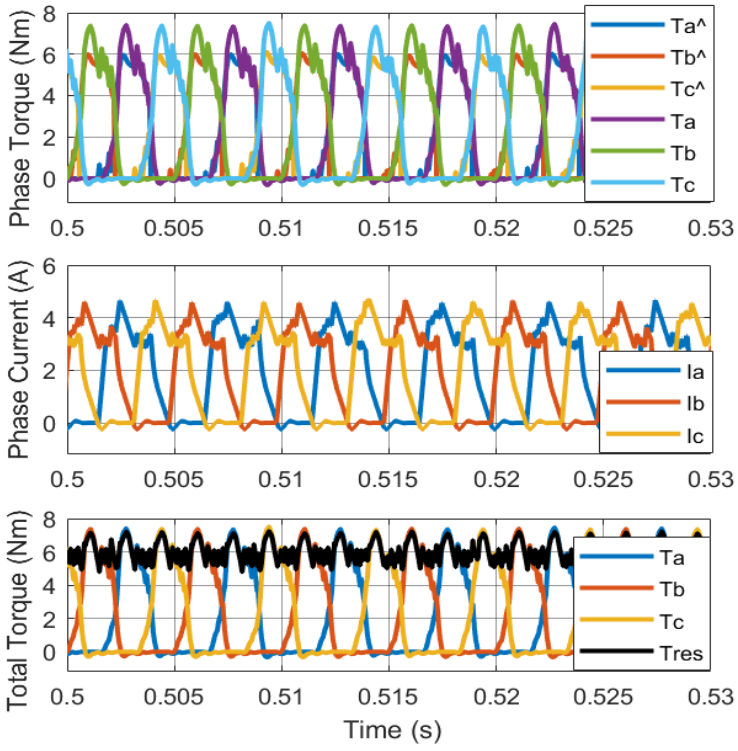
Phase Torque (Nm)
Ta^
Tb^
Tc^
Ta
Tb
Tc
Phase Current (A)
Ia
Ib
Ic
Total Torque (Nm)
Ta
Tb
Tc
Tres
Time (s)

(b)

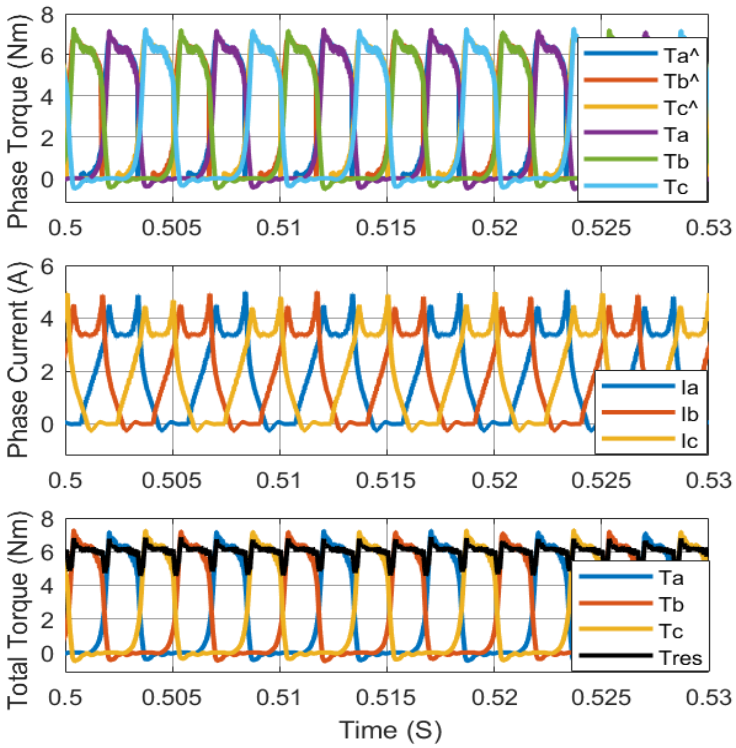

(c)

Figure 5.9 Phase current, phase torque and resultant torque of the methods a at 600 rpm with 6Nm load torque (a) HCC (b) DITC (c) AQSM

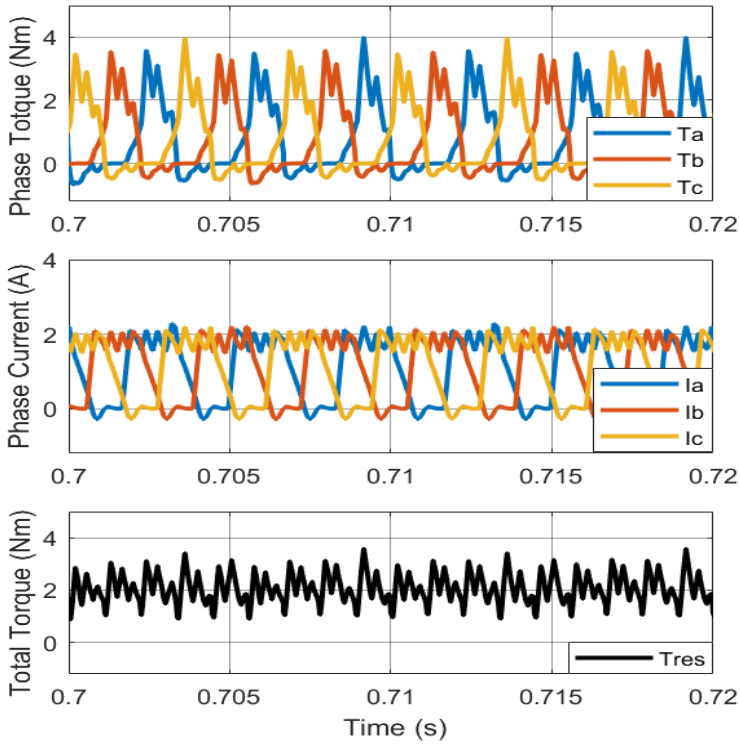

(a)

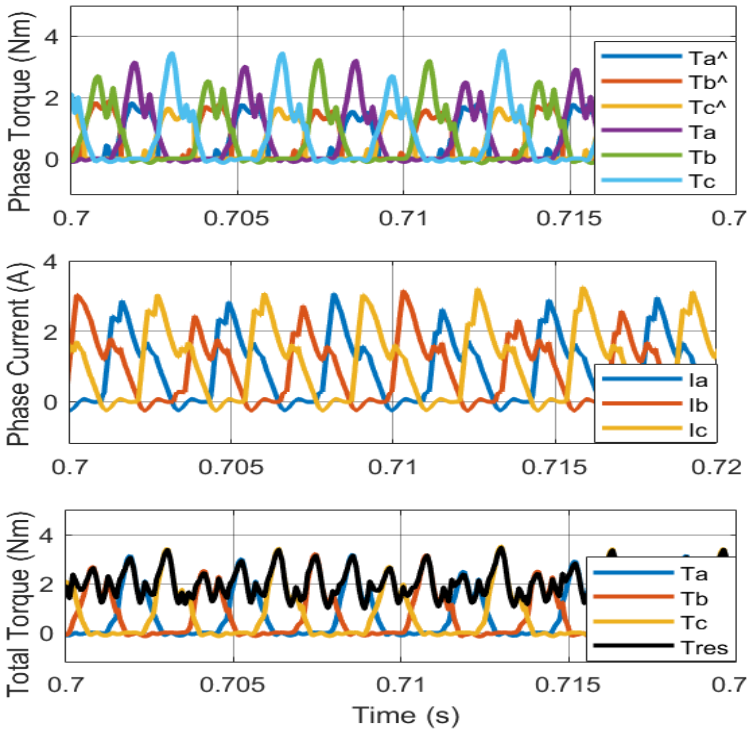

(b)

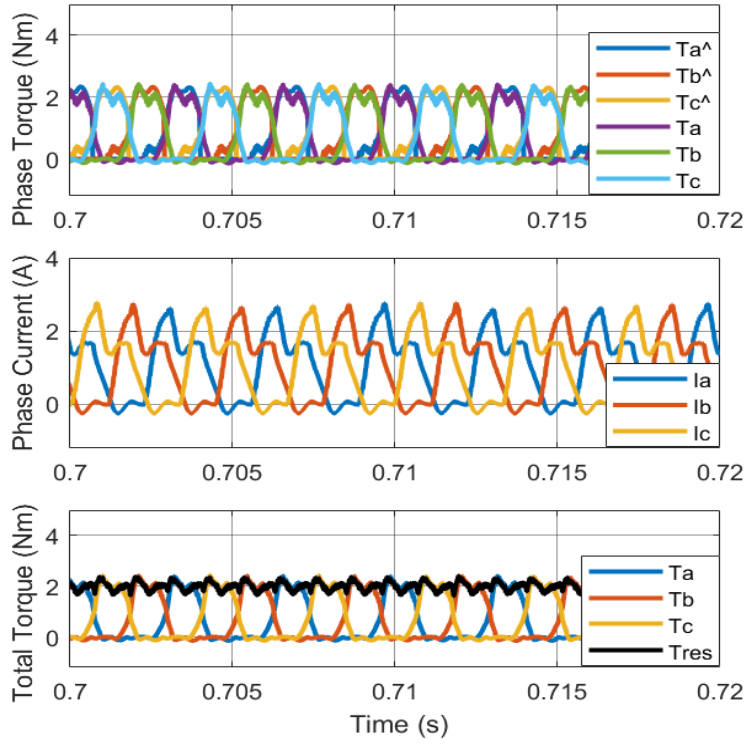

(c)

Figure 5.10: Phase current, phase torque and resultant torque of the methods at 900 rpm with 2Nm load torque (a) HCC (b) DITC (c) AQSM

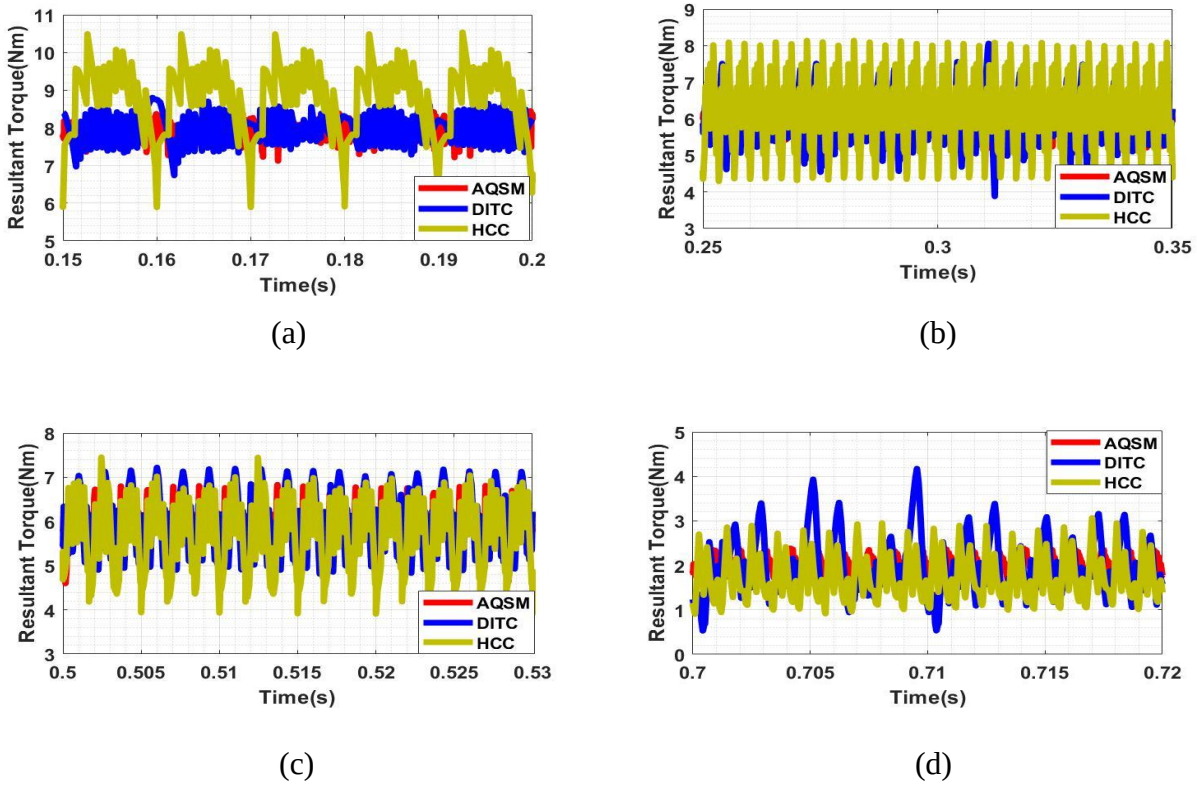

Figure 5.11: Comparison of Resultant Torque at (a) 100 rpm (b) 300 rpm (c) 600 rpm (d) 900 rpm

The tests represented at a different normal operational speed of the drive to show the relationship of the torque ripple with speed and the results are summarized in Table 5.3. As shown, the proposed AQSM based method offers superior torque ripple minimization over the tested range of speed followed by the DITC and then the HCC. It can also be noticed that all the compared methods show a decline in performance above the base speed (500 rpm) of the machine because of the effect of back EMF. Despite the increase in torque ripple because of the external load, the proposed control method can reduce it better over the tested range of speed. This demonstrates the higher robustness of the proposed control method to external disturbance. The torque ripple ratio of the results is calculated based on the following:

$$TRR = \frac{Maximum\ Torque - Minimum\ Torque}{Average\ Torque}$$

Table 5.3: Torque Ripple Ratio Across Speed

	Methods	100rpm	200rpm	300rpm	600rpm	900rpm
Torque Ripple Ratio (%)	**HCC**	54.0	52.7	60.2	61.4	65.6
	DITC	27.7	40.6	50.5	42.5	70.2
	AQSM	17.0	21.9	21.2	34.7	28.9

Furthermore, the generated average torque by the control methods at different speed demand is compared in Figure 5.12. The average torque produced by the compared methods to track the desired speed decrease as the reference speed increased. It is found that the proposed method generates a negligible less average torque to track the desired speeds of the SRM under the applied load because it was able to produce much smoother constant torque than the other methods.

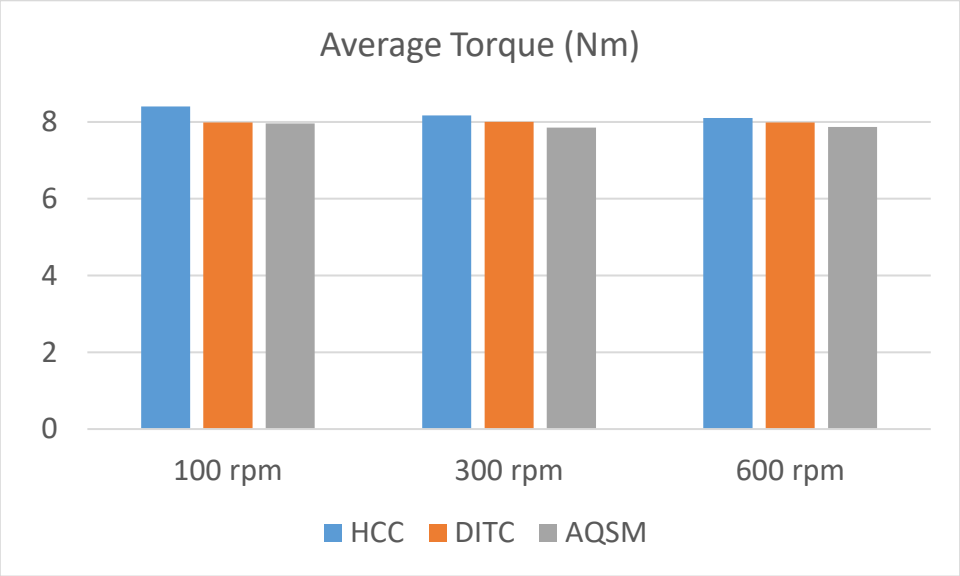

Figure 5.12 Comparison of Average Torque Across Speed

Figure 5.13 shows the comparison of control signals between the two torque controllers within the medium speed of the MASRM drive. The conventional DITC generates a discrete control signal of either maximum, zero or minimum voltage while the proposed DITC generates a continuous control signal within a predefined band to smoothly converge the error to zero. That is, the proposed controller can produce fewer oscillations in the control signal, hence reduce the current ripples that reduce the generated torque ripple of the drive.

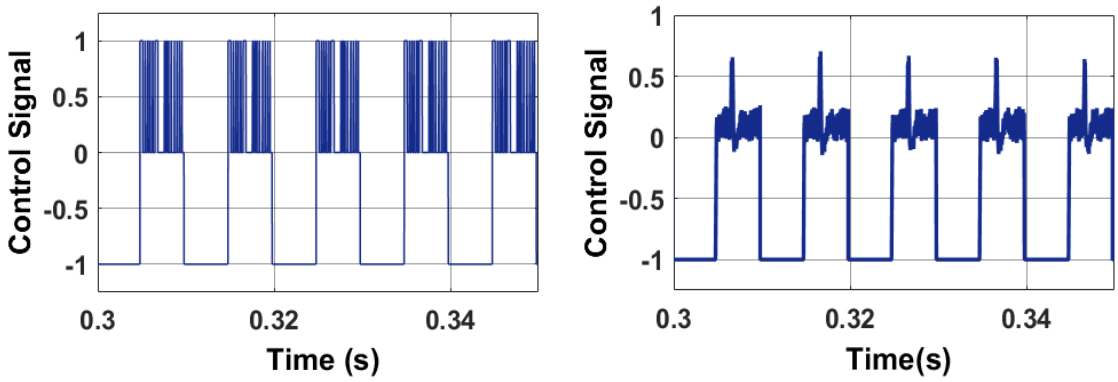

(a) (b)

Figure 5.13 Control signal of phase A at 300rpm (a) DITC method (b) Proposed method

5.7 Experimental Results of AQSM Control of MASRM

The HCC method generated a constant peak current of 5A to achieve the desired average torque without considering torque ripple minimization as shown in Figure 5.14. This phase current shape is typical of the HCC method. While in the DITC method, the phase currents are shaped to maintain the resultant torque close to the reference considering the reduction of torque ripples in the resultant torque. In addition, the action of the added current limiting control loop can be observed during the magnetization of the phases as it limits the current demanded by the DITC technique to properly regulate each phase torque. Thus, the DITC method can offer a better resultant torque characteristic if no current limiting is included, but the drive will need to be oversized to withstand the higher current peaks and higher switching frequency requirement of DITC. The selection of the control hysteresis band is limited, by the proposed 20 kHz switching frequency of the MASRM drive, to 0.4 Nm. This selection was done through manual trial. Though, if higher switching frequency would be allowed, a narrower hysteresis band and consequently smoother torque can be achieved. Also, the proposed AQSM based method shapes each phase current to regulate the resultant torque. Nevertheless, as explained in Section 5.4.3 it uses the $P\left[E_{T_m}(k)\right]$ and ε to limit the rate of change of the phase current and its magnitude in proportion to the size of $E_{T_m}(k)$. Thus, this maintains the individual phase currents of the MASRM drive within constraints without affecting the phase torque distribution and regulation that produces smooth resultant torque output.

Figures 5.15 and 5.16 show the measured phase current and resultant torque with the HCC, DITC, and proposed AQSM methods at speeds of 100 rpm and 600 rpm, respectively. Considering the test at 100 rpm, the proposed method offers much less torque ripple of 20.3%

compared to 49.6% and 67.5% of the DITC and HCC, respectively. Similarly, an improved torque ripple reduction is achieved by the proposed AQSM method at 600 rpm. Accordingly, the measured torque ripple for the AQSM is recorded to be 40.7% compared to 65.4% and 89.3% with the DITC and HCC, respectively.

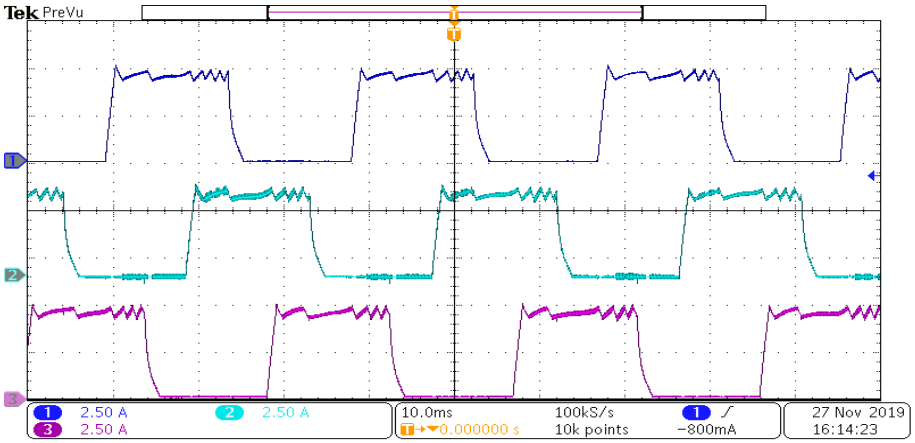

(a) HCC method (Ch1-3: 2.5 A/div and 10 ms/div)

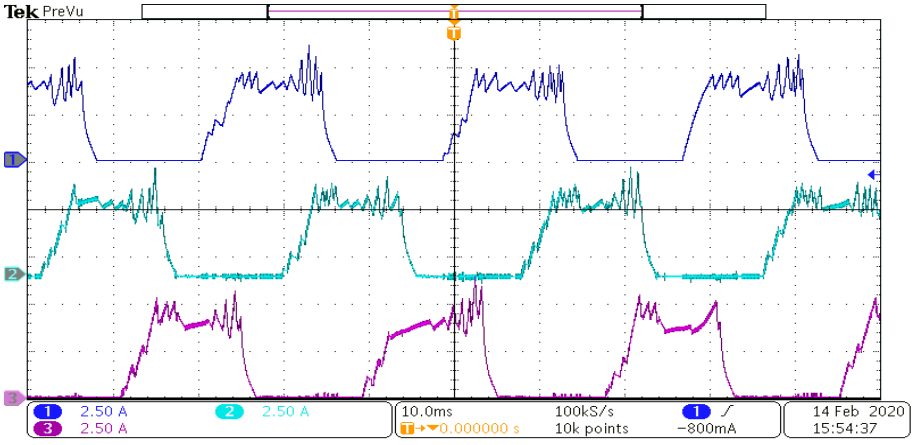

(b) DITC method (Ch1-3: 2.5 A/div and 10 ms/div)

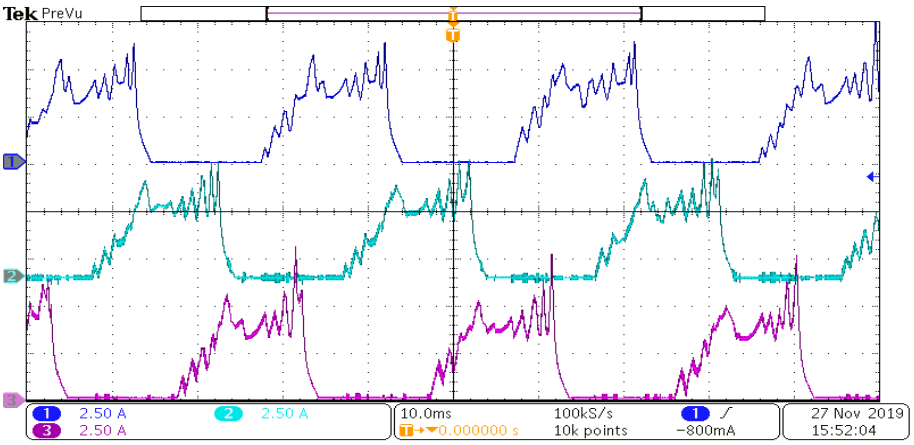

(c) Proposed AQSM method (Ch1-3: 2.5 A/div and 10 ms/div)

Figure 5.14: Experimental results showing the three-phase currents at 100 rpm and average torque of 8 Nm.

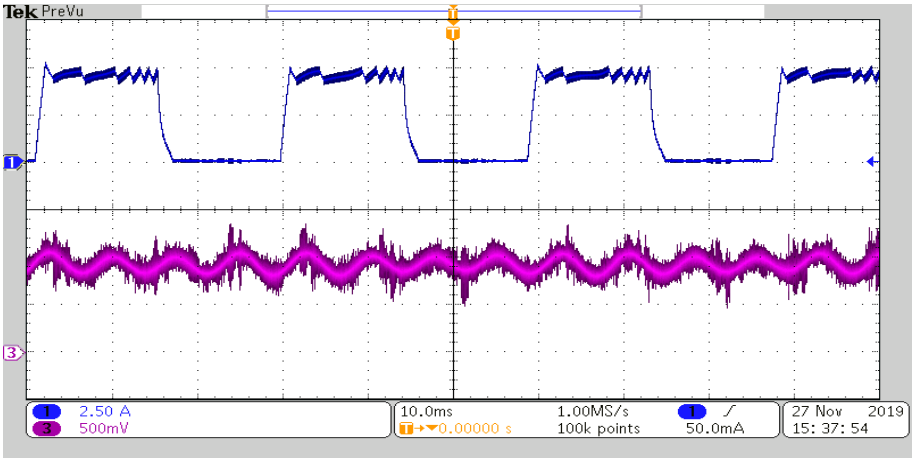

(a) HCC method (Ch1: 2.5 A/div and 10 ms/div; Ch 3: 5 Nm/div)

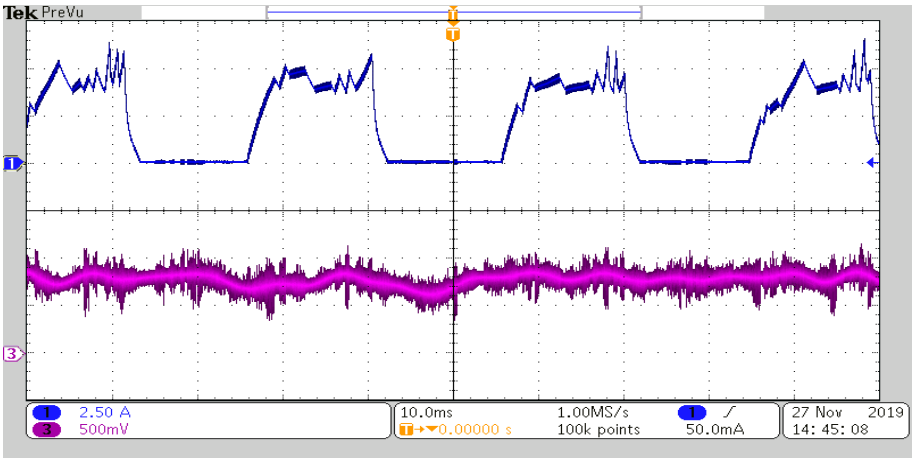

(b) DITC Method (Ch1: 2.5 A/div and 10 ms/div; Ch 3: 5 Nm/div)

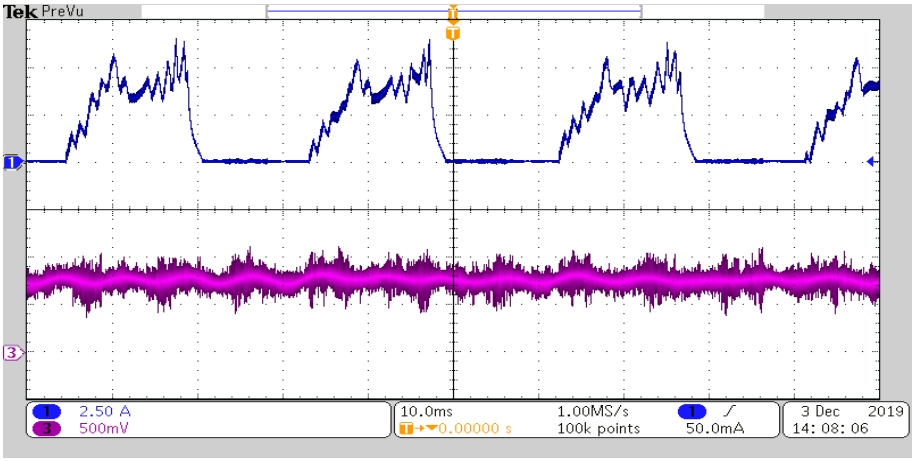

(c) AQSM method (Ch1: 2.5 A/div and 10 ms/div; Ch 3: 5 Nm/div)

Figure 5.15: Experimental results showing phase A current and resultant torque at 100 rpm with 8 Nm load torque.

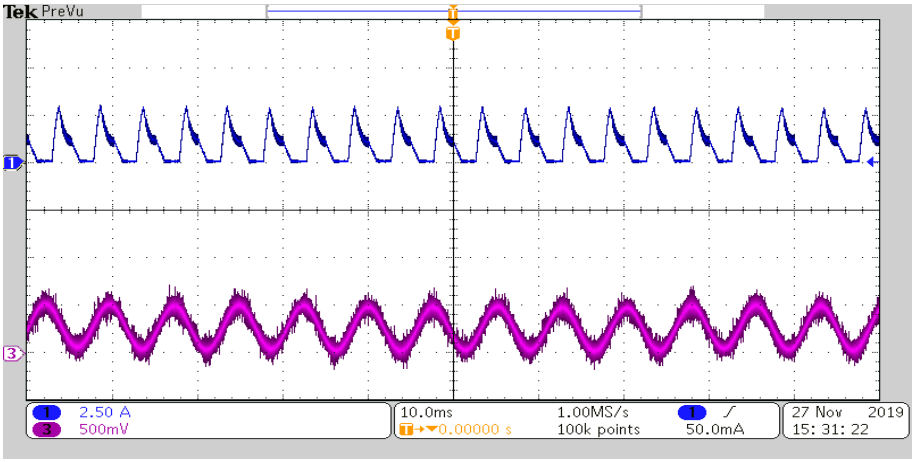

(a) HCC method (Ch1: 2.5 A/div and 10 ms/div; Ch 3: 5 Nm/div)

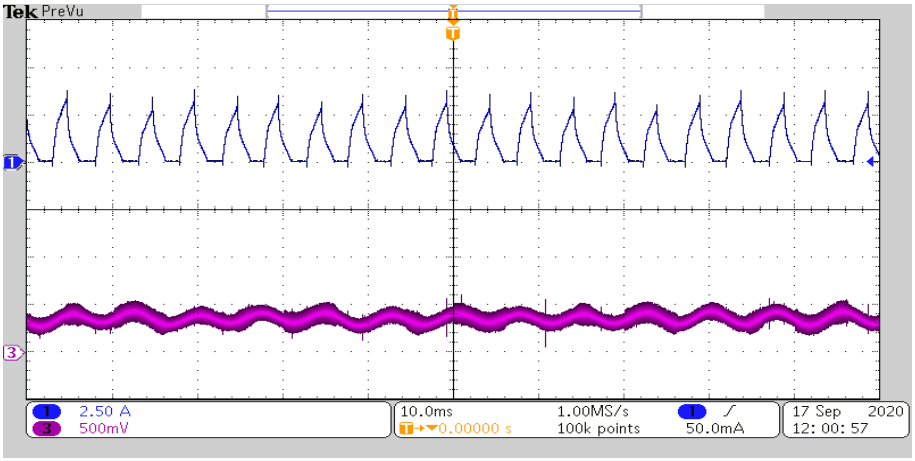

(b) DITC Method (Ch1: 2.5 A/div and 10 ms/div; Ch 3: 5 Nm/div)

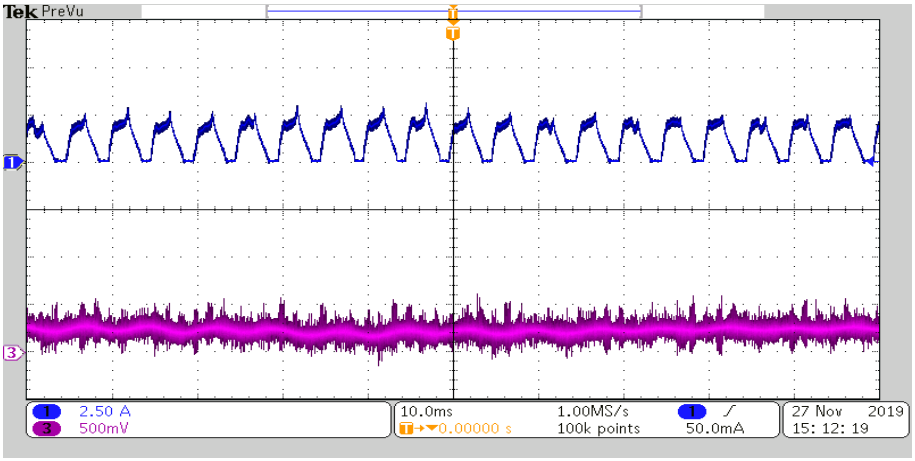

(c) AQSM method (Ch1: 2.5 A/div and 10 ms/div; Ch 3: 5 Nm/div)

Figure 5.16: Experimental results showing phase A current and resultant torque at 600 rpm with 4 Nm load torque.

Table 5.4 present the comparison between the three control methods for the torque characteristics across the range of speed of the MASRM drive. It can be observed that the proposed AQSM based method has better torque ripple reduction capability compared to the HCC and DITC methods across the MASRM drive range of operational speed. However, the torque ripple in the simulation results is less than that of the experimental results because the non-linear dynamics of the load and the mutual inductance and cross-saturation effects in the MASRM were approximated in the simulation.

Furthermore, the current that produces the torque during high-speed operation is limited by the high back EMF produced by the machine. Thus, all the considered control methods show higher torque ripple ratio during high-speed operation, which is noticeable in both the simulation and experimental results.

Table 5.4: Comparison of Torque Ripple Ratio

	Methods	**100rpm**	**200rpm**	**300rpm**	**600rpm**
Torque Ripple Ratio (%)	**HCC**	67.5	52.7	50.5	89.3
	DITC	49.6	41.6	42.4	65.4
	AQSM	20.3	25.9	23.9	40.7

5.8 Experimental Results of Reliability and Complexity analysis of MASRM control

An experimental measurement was run with the DITC and AQSM methods signals to analyse the real-time effect of the measurement noise and errors on the control methods. For safety reason, extra noise and errors were not injected into the system as it is done in the simulation instead, the experiments were done with and without terminal measurement filtering to test the effect of the measurement noise. The experiments in the previous section (section 5.7) were carried out on the MASRM drive test rig without filtering out the measured phase current for both the HCC and AQSM control methods but for a fair comparison with regards to torque ripple minimization, the DITC required measurement filtration. Figure 5.17 shows the effect of not filtering the phase current measurement on the DITC.

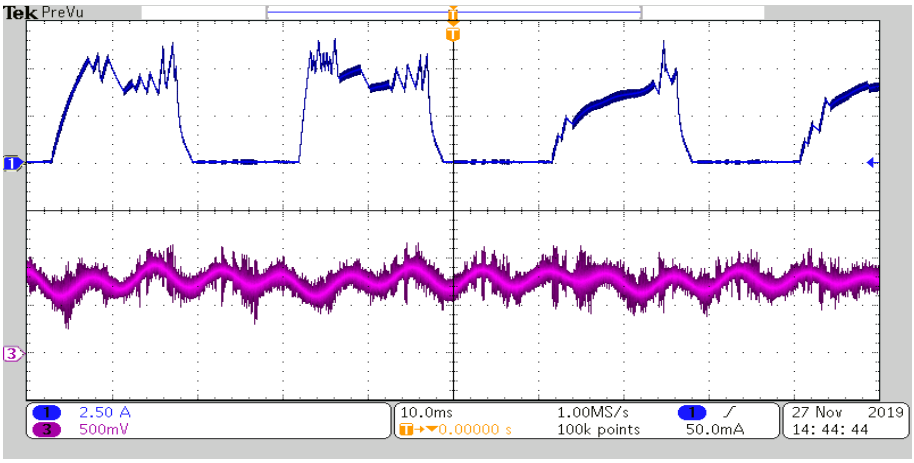

(a) DITC Method (Ch1: 2.5 A/div and 10 ms/div; Ch 3: 5 Nm/div)

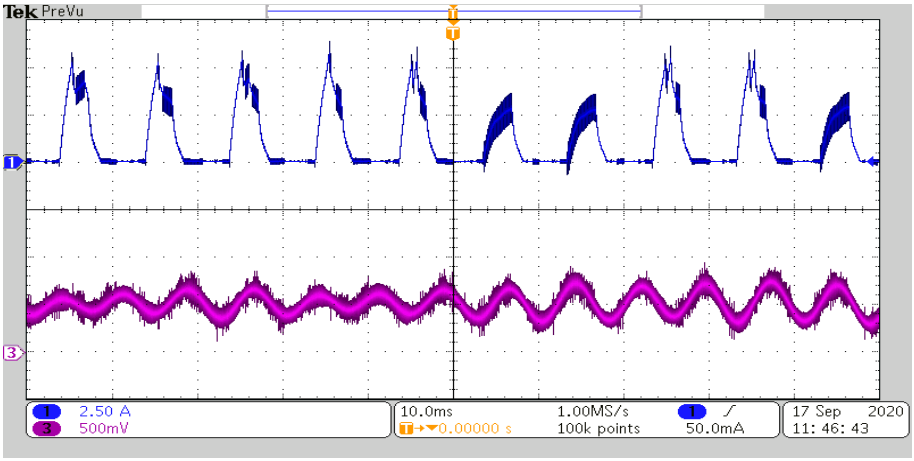

(b) DITC Method (Ch1: 2.5 A/div and 10 ms/div; Ch 3: 5 Nm/div)

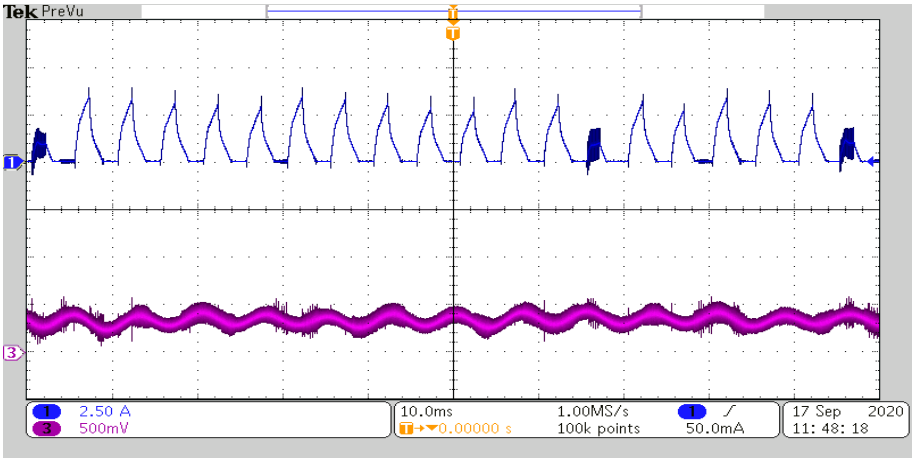

(c) DITC Method (Ch1: 2.5 A/div and 10 ms/div; Ch 3: 5 Nm/div)

Figure 5.17: Experimental results of DITC method without measurement filter showing phase A current and resultant torque at (a)100 rpm (b)300 rpm (c) 600 rpm.

By comparing the resultant torque with and without measurement uncertainties of the DITC method with the MASRM running at different speed is presented above. The effect of the error can be observed to affect the performance of the DITC method across the speed of the drive when observing Figure 5.14 to Figure 5.16. Thus, a reliable control system should have a reasonable accuracy under a certain level of uncertainties. The results obtained for the three methods show that the HCC and AQSM methods has better robustness to measurement error because the measured feedback did not show significant distortion with no filtering. While the DITC showing significant effects on its performance without filtering the feedback signals.

5.9 Summary

Considering the limitations of general torque control technique such as high switching frequency requirement, generation of current ripple during phase magnetization due to hysteresis type switching and high current demand near aligned and unaligned rotor position, a novel improved torque control based on an adaptive type QSM method is proposed. The adaptive QSM control regulates the machine's torque error to zero while maintaining the control signal and output torque within desired constraints. The proposed control law can reduce the resultant torque ripple, the losses and thermal stress on the power devices, and computational cost of the control process. A PWM based switching is proposed instead of the conventional hysteresis switching because it is flexible to handle the required higher degree of freedom of the proposed torque regulator. An experimental test rig has been setup in the lab to test the performance of the control algorithms developed above. Simulation and experimental

results verified that the proposed control method can significantly reduce the torque ripple over the speed range of the MASRM compared to conventional HCC and DITC methods.

CHAPTER 6

SENSORLESS CONTROL AND MODIFIED CONVERTER TOPOLOGY

Magnet-assisted switched reluctance machines have been considered for electric drive applications because of its low cost and robustness. Nevertheless, the power electronics and transducers normally required to operate the drive, increase its cost, size, and weight, and it also reduces its running reliability and robustness. Therefore, the number of switches, diodes, and sensors involved are needed to be reduced by improving the power converter topology and its control strategy.

A new sensorless drive (without direct speed or position sensor) of MASRM using a single current sensor based Resistor-Dump (R-Dump) converter is proposed in this study to reduce the power components and transducers compared with the traditionally use converters like an asymmetric half-bridge converter. The sensorless control method is developed based on a new sliding mode observer (SMO) that is defined to only use a single current measurement and an inductance model to estimate the rotor position of the MASRM.

6.1 Introduction

MASRM has advantages of its low-cost, fault-tolerance, high torque density and wide speed range of operation. Nevertheless, its drive needs accurate and rapid information of machine rotor position to work effectively due to its principle of operation. Conventionally, a separate rotor position transducer is employed to detect the rotor position of the MASRM though, it normally adds extra size, weight, and cost to the drive. Furthermore, rotor position transducers (sensors) often reduce the reliability of the drive as they add additional physical connections and can be vulnerable to environmental factors. Hence, an encoderless method can be used to estimate SRM's rotor position using the measured machine terminal current and voltage [165, 166]. Nonetheless, these measured feedback signals are often affected by measurement noise and errors during the acquisition process. Hence, the efficacy of the estimation method depends on the robustness of the estimation technique to these measurement uncertainties.

Normally, estimation of rotor position in SRM drives is based on the relationship between the machine's phase current, phase flux-linkage and rotor position. Yet, it is impractical to directly measure the flux-linkage, thus, it is conventionally estimated by integrating the voltage across an excited phase which requires measurement of phase current and phase voltage. However, the accuracy of this estimation technique can be affected by several error components presented in Table 2.1 in chapter 2

Additionally, the power electronics involved in the implementation of the MASRM drive increases its size, weight, and cost and reduces its running reliability as mentioned earlier. Commonly, a voltage sensor and current sensors for each phase are used to estimate the MASRM rotor position.

In this study, the use of a single current sensor and single voltage sensor with a modified version of the standard asymmetrical converter of MASRM drive is investigated. Although this reduces the number of current sensors, nevertheless, the power devices count, and ratings remain the same as with the traditional asymmetrical converter.

The reliability, weight, volume, and power density of the sensorless MASRM drive can be further significantly improved by employing a converter topology with a reduced number of switches, and diodes, in addition to the reduced count of transducers involved.

In this chapter, a single switch per phase R- Dump converter configuration of SRM drive is modified to employ a single current sensor. A new sliding mode observer (SMO) based sensorless control is developed for both the proposed R-Dump converter and single current sensor asymmetrical converter for analytical comparison. Figure 6.1 presents the structure of the SRM drive simulated to evaluate the performance of the considered converters.

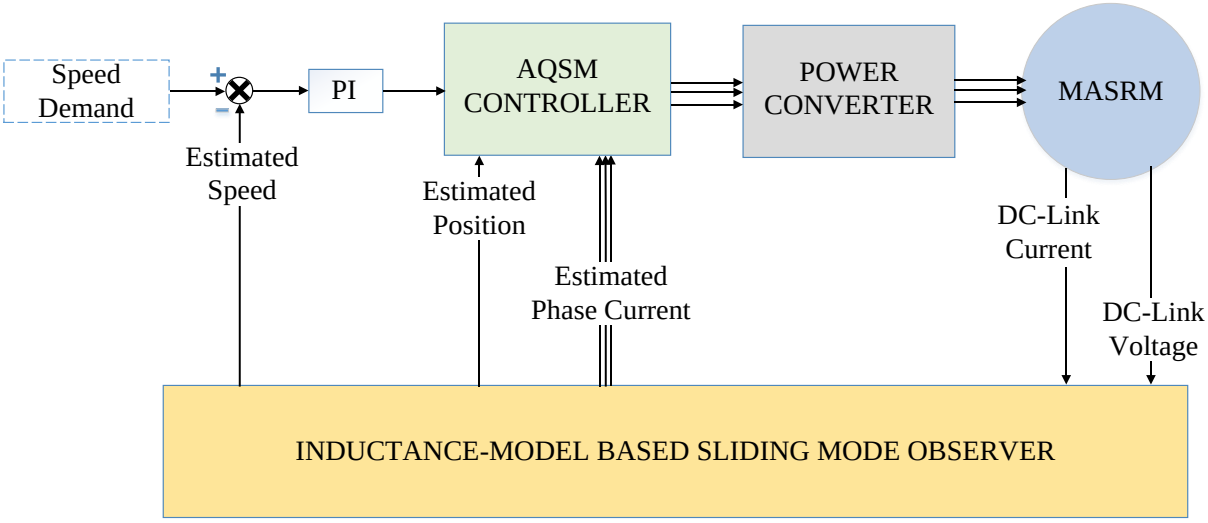

Figure 6.1: Structure of the proposed sensorless variable-speed MASRM drive

6.2 Single Current Sensor R-Dump Converter

Figure 6.2 show the conventional AHBC topology, has main advantages of control flexibility and good efficiency over a wide range of speed because the phases in the machine can be operated independently with each having three operation states of on, off and freewheeling. The main demerit of this converter is that it requires a high count of power devices per phase. It needs 2 switches, 2 free-wheeling diodes and 1 current sensor and/or 1 voltage sensor per phase to operate, which increases the drive's cost, size, weight, and rate of failure (reducing its reliability).

Normally, the phase currents of SRM are individually controlled to effectively generate the desired resultant output torque. Each of the phase currents is often controlled by using either hysteresis control, voltage PWM control or current PWM control. As detailed in Chapter 5, a modified version of the second is employed in the torque control proposed in this study. Most control methods are implemented using the measured instantaneous values of the SRM phase currents, and separate current sensors are often used for each phase in the conventional converters to implement the current or torque control. These added sensors come with the disadvantages mentioned above.

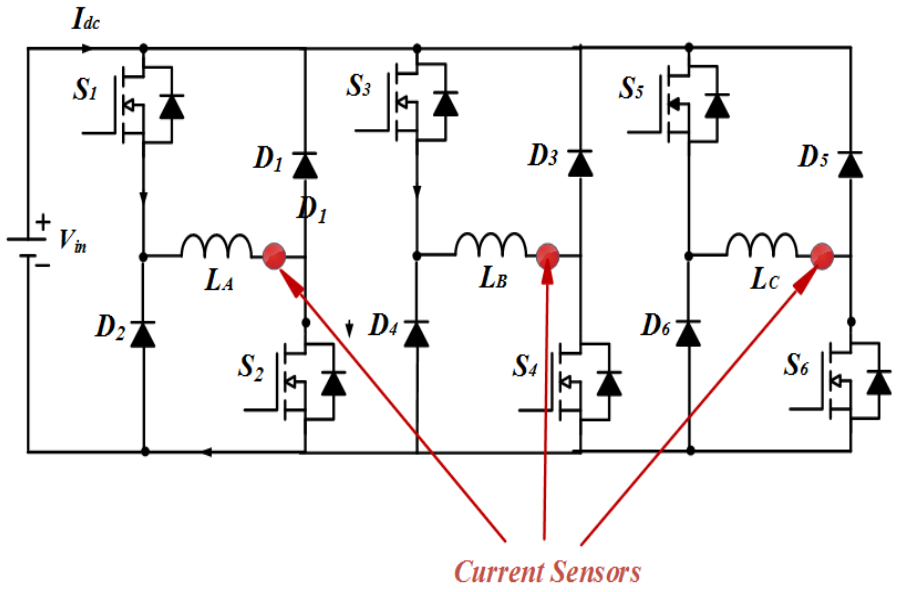

Figure 6.2: Circuit diagram of traditional AHBC Converter

To overcome these limitations, a phase current reconstruction method is proposed in [230] to reduce the number of current sensors by using only the DC-LINK current sensor measurement, rewiring the conventional AHBC and injecting double high-frequency pulses into the lower

switches of the conducting phases. That is, the proposed method uses only one current sensor measuring the dc-link current to implement a hysteresis current control with no additional circuit elements. Since a DC-link current is the sum of all phase currents of the SRM, hence, this new AHBC configuration allows the decomposition of the DC-link current into the phase currents.

An R- Dump converter topology for an SRM converter is designed to have a minimal number of power devices compared to its counterparts. It employs only 1 switch, 1 diode, 1 current sensor and/or 1 voltage sensor per phase. Still, it requires additional passive components of a resistor R and a capacitor C. Normally, the reduced components count can lower the cost, size and weight of the power converter and improve its reliability.

Figure 6.3(a) shows the single sensor R-dump converter proposed for the control of the MASRM drive. Its working principle is like that of the AHBC except during the turn-off operation. If a phase switch is turned ‘off’, the phase current will freewheel through the phase diode. Hence, the magnetic energy stored in the phase winding will be charging the capacitor C through the DC supply voltage and will also be dissipating in the resistor R. hence, compared to other converters with higher count of devices like the AHBC, the efficiency of the R-Dump is lower. This study focuses more on the investigation of sensorless torque control of the R-Dump and AHBC converters with only one current sensor and therefore full efficiency comparison between the two converters is beyond the scope of this thesis.

Figure 6.3(a) depicts the current excitation profile of MASRM drive using the single sensor based R-Dump Converter. Where $\theta 1, \theta 2, \theta 3, \theta 4,$ and $\theta 5$ are the turn-on angle of phase A, turn-off angle of phase C, turn-on angle of phase B, turn-off angle phase A, and ending angle of phase A, respectively. It can be observed that by neglecting the demagnetization current of all the phases, the dc-link current is equal to the sum the overlapping phase currents at Region I and III, and it is only equal to the current of phase A at Region II and only equals to the phase current of phase B at Region IV. Furthermore, it can be seen from Figure 6.4(b) that the single current sensor is positioned at a unique point to be able to measure the dc-link current without the effect of the demagnetization current of any of the phases.

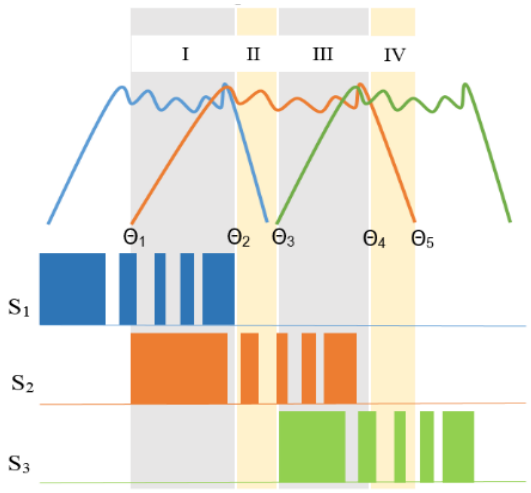

(a)

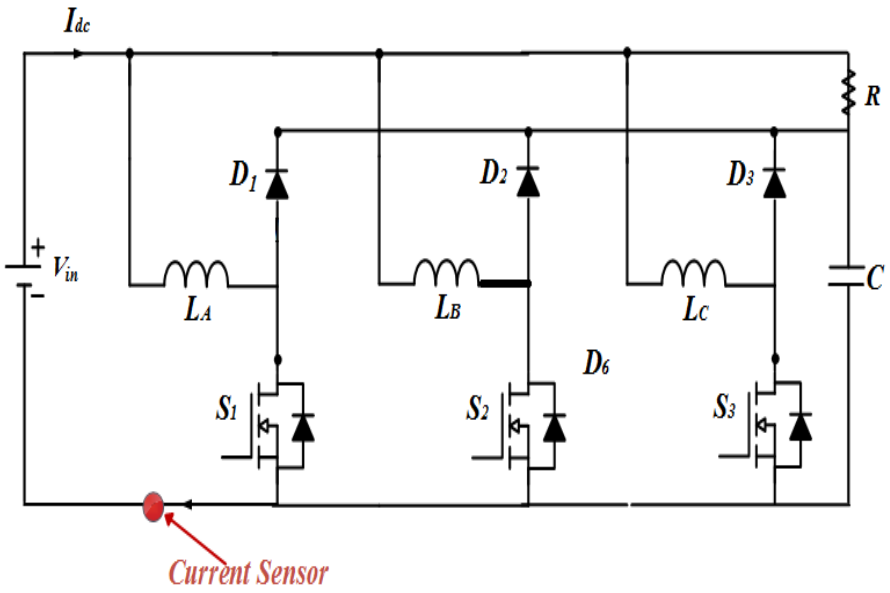

(b)

Figure 6.3: Single sensor R-dump converter (a) Excitation Profile (b) Circuit diagram

Therefore, the dc-link current with zero demagnetization current that is the same as the sum of the phase currents at a particular sampling instance k, can be defined as in Table 6.1 and mathematically expressed as:

$$i_{dc}(k) = \begin{cases} i_C(k) + i_a(k), & \theta_1 < \theta \leq \theta_2 \\ i_a(k), & \theta_2 < \theta \leq \theta_3 \\ i_b(k) + i_a(k), & \theta_3 < \theta \leq \theta_4 \\ i_b(k), & \theta_4 < \theta \leq \theta_5 \end{cases} \tag{6.1}$$

Table 6.1: Relationship Between the Switching States and DC-Link Current

S_1	S_2	S_3	i_{dc}
1	0	0	i_a
1	1	0	$i_a + i_b$
0	1	0	i_b
0	1	1	$i_b + i_c$
0	0	1	i_c

6.3 Sliding Mode Observer Using Single Current Sensor

Estimation of MASRM rotor position is developed in this section using a sliding mode observer. Traditional SMO uses the errors between each measured and estimated phase currents. Whilst, in this study, an SMO that employs only the error between the measured DC-link current and estimated DC-link current to predict the motor drive parameters is proposed. The proposed estimation method has the following merits:

- The phase current reconstruction method using the SMO does not require any signal injection to any of the phase switches to reconstruct the machine's parameter. This gives it the advantage of not having any torque drag due to signal injection.
- Significant reduction in size, weight, and cost of the MASRM drive because of absence of encoder and reduced current sensors
- Significant improvement in reliability and robustness of the MASRM drive because of reduced complexity and number of transducers.

6.3.1 Sliding Mode Observers

The SMO-based approach delivers a robust estimation of position and speed in comparison with the other rotor position estimation technique. It can exhibit a high degree of robustness in the face of model uncertainty, parameter variation, load torque disturbance, and initial rotor position error [224]. Other approaches like the lookup-table-based approach are highly dependent on the accuracy of the static characteristics of the machine. The error in flux estimation or model uncertainty will easily lead to error in position estimation. In addition, the speed of the machine in the lookup-table-based approach is obtained by differentiating its

angular position, which can lead to instability problems during four-quadrant operation in the presence of errors in position estimation. Alternatively, the inductance-based model assists the SMO to be observable at the zero-speed crossing, enabling the SMO to simultaneously predict both the rotor position and speed [231].

6.3.2 MASRM differential equation

A real-time model of the MASRM system is needed to define a sliding mode observer for the position estimation of the drive. The sliding mode observer is designed based on the following differential equations of the MASRM as derived in Chapter 3.

A standard format of the MASRM differential equations can be presented as:

$$\frac{di_j}{dt} = \frac{V_{bus} \cdot d_j - V_{loss}(i_j) - i_j \frac{\partial L_j(\theta,i)}{\partial \theta} \cdot \omega}{L_j(\theta,i) + i_j \frac{\partial L_{j(\theta,i)}}{\partial i_j}} = \frac{X(\theta,i,\omega)}{Y(\theta,i)} \tag{6.2}$$

where

$$\left.\begin{array}{c} \omega = \frac{d\theta}{dt} \\ \frac{\partial L_j(\theta,i)}{\partial \theta} = -\sum_{n=1}^{m} A_{k,j}(i) n N_r \sin(nN_r\theta) \\ \frac{\partial L_j(\theta,i)}{\partial i_j} = \sum_{n=0}^{m} \frac{\partial A_{k,j}(i)}{\partial i_j} \cos(nN_r\theta) \\ L(\theta,i) = \sum_{n=0}^{m} A_n(i) \cdot \cos(nN_r\theta + \varphi_n) . \end{array}\right\} \tag{6.3}$$

The torque-speed equation (electromechanical equations) can be expressed as:

$$J\frac{d\omega}{dt} = \sum_{j=1}^{m} T_{e\,j} - T_L \tag{6.4}$$

where $T_{e\,j}$ and T_L are phase torque and load torque, respectively.

The resultant torque can be obtained by the summing up the individual phase torques as expressed below:

$$T_e = \sum_{j=1}^{m} \frac{\partial W_{c_j}}{\partial \theta} = \quad \sum_{j=1}^{m} \frac{\partial \int L_j(\theta,i) i_j di}{\partial \theta} \tag{6.5}$$

Therefore, the angular acceleration of the machine can be expressed as:

$$\frac{d\omega}{dt} = \frac{\sum_{j=1}^{m} T_{ej} - T_L}{J} = Z(\theta, i) \tag{6.6}$$

The mechanical equation can be expressed as:

$$\frac{d\theta}{dt} = \omega \tag{6.7}$$

6.3.3 Definition of traditional Sliding Mode Observer

A sliding mode observer for the estimation of the rotor position of an SRM is generally defined based on the sign of an error variable derived from the dynamics of the system. The error variable E is often based on the difference between the measured and estimated phase current or phase flux of the machine as expressed in (6.8) and (6.9). It is used to stabilize the error dynamics of the estimation [223, 224, 231].

$$E_i = \sum_{j=1}^{N} (\bar{\imath}_j - i_j) \tag{6.8}$$

$$E_i = \sum_{j=1}^{N} (\overline{\Psi}_j - \Psi_j) \tag{6.9}$$

According to the system differential equations derived from the inductance model of the MASRM, a traditional second-order sliding mode observer for rotor position and speed estimation can be defined by the following expressions:

$$\dot{\bar{\theta}} = \bar{\omega} + K_\theta \, sgn(E_i) \tag{6.10}$$

$$\dot{\bar{\omega}} = Z(\bar{\theta}, \bar{\imath}) + K_\omega \, sgn(E_i) \tag{6.11}$$

where $\bar{\omega}, \bar{\theta}$, and $\bar{\imath}$, are the estimations of ω,θ, and i. $Z(\bar{\theta}, \bar{\imath})$ is the estimated angular acceleration. E_i is an error function based on measured and estimated variables that are used to stabilize the error dynamics of the estimation process. $sgn()$ returns the sign of the expression sent to it. The following error function is used for the implementation of the traditional SMO on the MASRM:

$$E_i = \sum_{j=1}^{N} (\bar{\imath}_j - i_j) \tag{6.12}$$

Then, the following estimation errors are defined to describe the observer error dynamics:

$$E_\theta = \theta - \bar{\theta} \tag{6.13}$$

$$E_\omega = \omega - \bar{\omega} \tag{6.14}$$

Differentiating (6.13) and (6.14) yields (6.15) and (6.16), respectively.

$$\dot{E}_\theta = \dot{\theta} - \dot{\bar{\theta}} \tag{6.15}$$

$$\dot{E}_\omega = \dot{\omega} - \dot{\bar{\omega}} \tag{6.16}$$

By substituting (6.10) and (6.11) in (6.15) and (6.16), respectively we get:

$$\dot{E}_\theta = \dot{\theta} - \{\bar{\omega} + K_\theta \, sgn(E_i)\} \tag{6.17}$$

$$\dot{E}_\omega = \dot{\omega} - Z(\bar{\theta}, \bar{\imath}) + K_\omega \, sgn(E_i) \tag{6.18}$$

Equation (6.17) and (6.18) can also be represented as:

$$\dot{E}_\theta = E_\omega - K_\theta \, sgn(E_i) \tag{6.19}$$

$$\dot{E}_\omega = Z(\theta, i) - [Z(\bar{\theta}, \bar{\imath}) + K_\omega \, sgn(E_i)] \tag{6.20}$$

Since the gain K_ω is often selected to be large enough, then $Z(\theta, i) - Z(\bar{\theta}, \bar{\imath})$ in the speed error equation (6.20) can be approximated as:

$$\dot{E}_\omega = -K_\omega \, sgn(E_i) \tag{6.21}$$

From (6.19), it can be seen that if the error function E_i is selected to have the same sign as E_θ, and the observer gain K_θ is selected to satisfy the following inequality:

$$K_\theta > |E_\omega| \tag{6.22}$$

then $E_\theta$will always have a sign that is different from that of $\dot{E}_\theta$ and then the sliding surface $E_\theta = 0$ will be reached in finite time.

From the analysis above, it can be concluded that the error function E_i, which compares the measured phase current variable with its corresponding estimated value, need to have the same sign as E_θ. Therefore, whenever the sliding surface is reached, the estimation error dynamics decrees to zero i.e $\dot{E}_\theta = 0$ which also leads to $\dot{E}_\omega$ exponentially decaying to zero.

6.3.4 Definition of Proposed Sliding Mode Observer

In this study, a new error variable is proposed for the SMO to be used in the position estimation of MASRM with the proposed single sensor R-Dump converter. The proposed error compares the measured and estimated DC-Link current as shown in (6.23). The estimated value of i_{dc} is calculated from the expression for current reconstruction in (6.1) and Table 6.1, while the phase currents of phase A, phase B, and phase C are obtained from the MASRM dynamics presented in (6.2).

$$E_{dc} = (\bar{\imath}_{dc} - i_{dc}) \tag{6.23}$$

The new estimation of the rotor position and angular speed can be obtained from the SMO dynamics in (6.10) and (6.11) and then expressed as follows:

$$\dot{\bar{\theta}} = \bar{\omega} + K_{\theta}\, sgn(E_{dc}) \tag{6.24}$$

$$\dot{\bar{\omega}} = Z(\bar{\theta}, \bar{\imath}) + K_{\omega}\, sgn(E_{dc}) \tag{6.25}$$

where $\bar{\omega}, \bar{\theta}, \bar{\imath}$, are the estimations of ω,θ, i, and $Z(\bar{\theta}, \bar{\imath})$ is the estimated angular acceleration and the function $sgn()$ returns the sign of its operand, as it is in the conventional per phase error calculation.

6.4 Results and Discussion of sensorless control of MASRM

The sliding mode observers defined above has been developed in MATLAB/Simulink. The actual machine's representation model and the estimation model were created using the measurement data from the motor and Fourier series based model, respectively. With a practical system, the current and voltage measurements are often corrupted by noise and uncertainties. To test the developed observer under the effect of measurement error and noise, sensor scaling, and offset errors and measurement noise were added to the actual measurements.

However, it is difficult to quantify each error component in the instantaneous measurements of the machine's feedback signal because their causal factors are system dependent and time-varying. Therefore, an error signal with random amplitude and frequency can be assumed to represent the total measured current and voltage error for analysis.

Preferably, the effect of both current and voltage measurement together with the estimation-model uncertainties should be considered when analysing the error involved in both the position and speed estimation. The effects of each phase voltage and phase current error in the rotor position and speed estimation are represented by a resultant error of 10% in the phase voltage measurement and 10% in phase current measurement. A white noise with a 10% amplitude and 20 kHz sampling time is used in the simulation to represent the errors.

6.4.1 Results Analysis of Traditional SMO sensorless Control

The traditional SMO is employed on a traditional AHBC. Figure 6.4 and Figure 6.5 depict the phase current waveforms and the phase voltage waveforms respectively, both with and without measurement error at 500 rpm. The effect of the error on the measured phase voltage and phase current signals can be observed to cause a significant change. This change can be employed to analyze the accuracy of the SMO under the efferent of measurement noise and error.

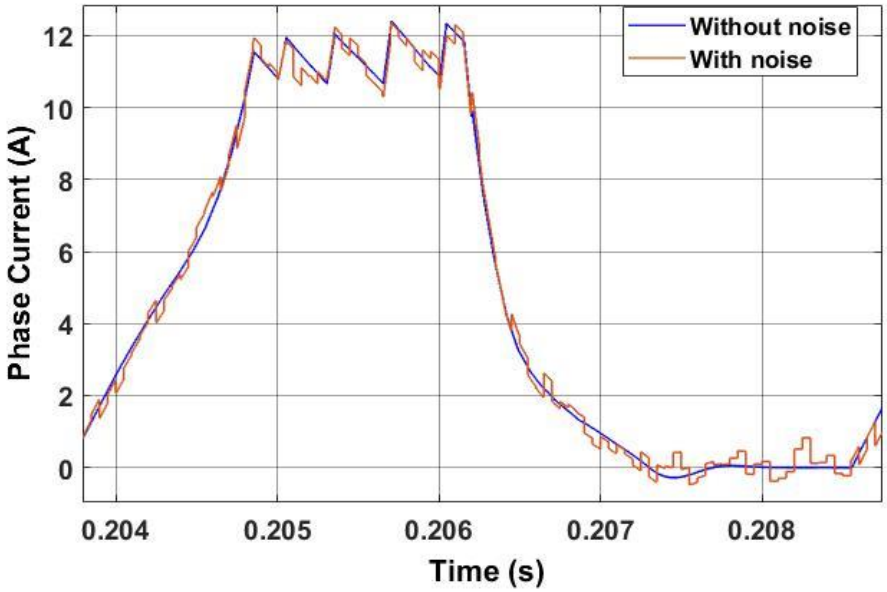

Figure 6.4: MASRM phase current with and without measurement error comparison

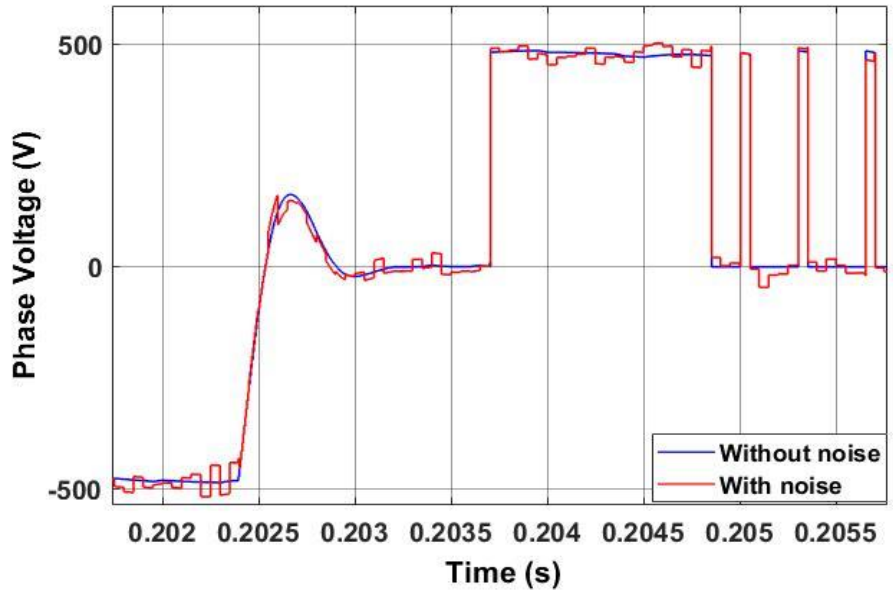

Figure 6.5: SRM phase voltage with and without measurement error comparison.

Furthermore, it is difficult to obtain a perfect dynamic model of the machine. Hence, the model is generally not ideal due to the inherent high non-linearity and tine varying properties of MASRMs. Therefore, a good rotor position estimation method should have reasonable robustness to uncertainties. Hence, a small deviation of the feedback signals from its true value due to the measurement error and noise, together with the model uncertainty should only decrease its accuracy by a small and reasonable amount.

Figure 6.7 shows the comparison of the actual and estimated phase current at 500 rpm. The difference between these phase currents is used to calculate the sliding surface of the SMO. It can be easily seen that the phase currents are not exactly equal because of the measurement error and model uncertainties.

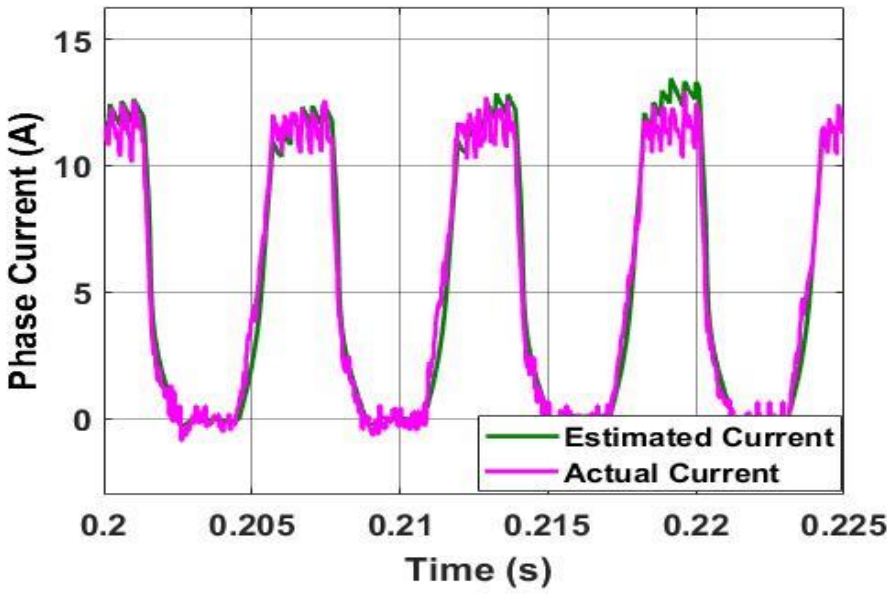

Figure 6.7: Comparison of actual and estimated phase current with the random error signal.

The waveform of the comparisons between actual and estimated rotor position and speed of the MASRM with the traditional SMO, running at a steady speed of 500 rpm is presented in Figure 6.8. It can be observed that the results show an acceptable accuracy in the estimation of both rotor position and speed.

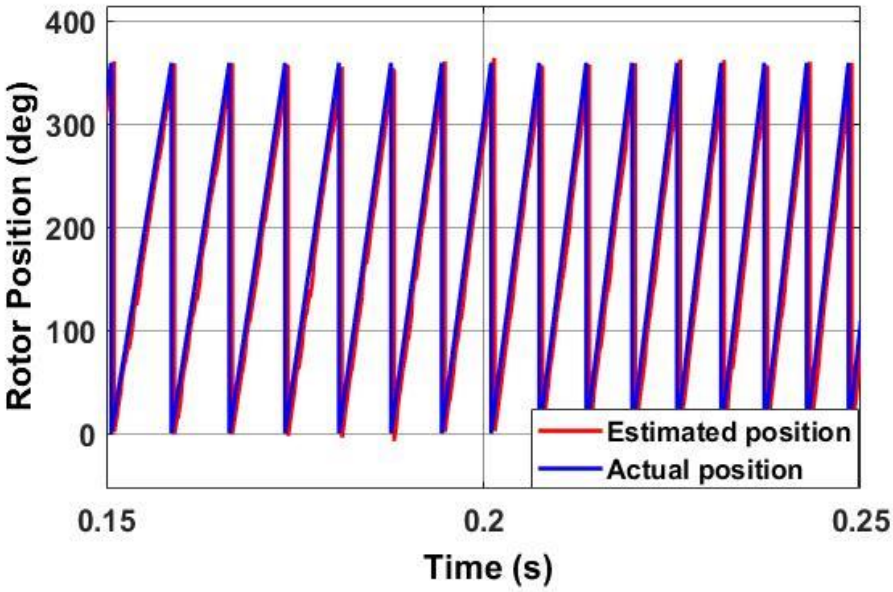

(a)

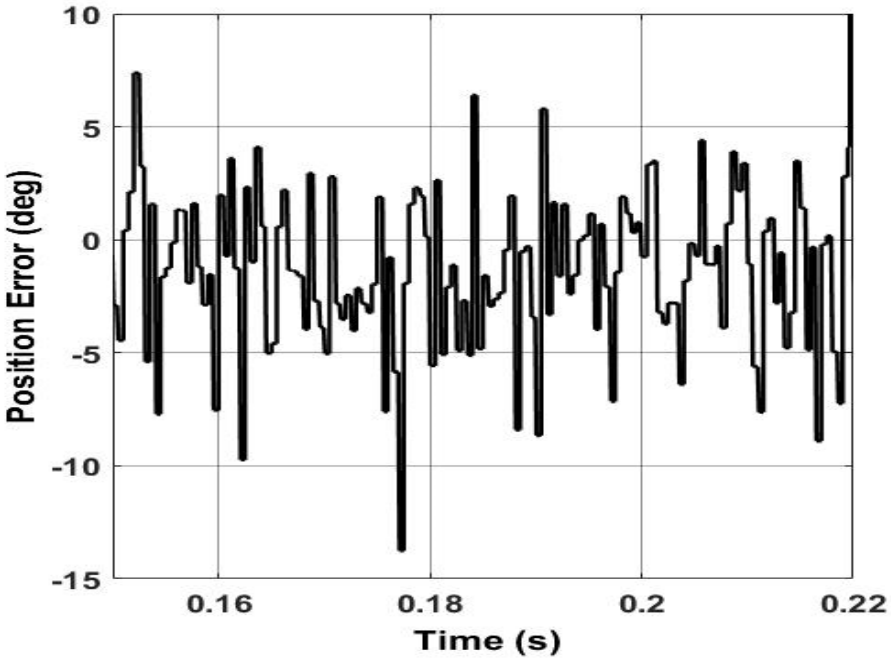

(b)

Figure 6.8. Actual and SMO estimation at 500rpm (a) rotor position (b) Position estimation error

Moreover, a very low-speed result of the position estimation is shown in Figure 6.9. The observer estimated position has a large error at near zero speed. This is because regular operating electrical signals are not available within this region. Hence, a larger error from the estimation-model calculation is produced which affects the rate of convergence of the SMO. In addition, the noise effect is also more significant when compared to the available measured feedback signals. Therefore, a simple technique that excites and aligns the MASRM drive at start-up is developed.

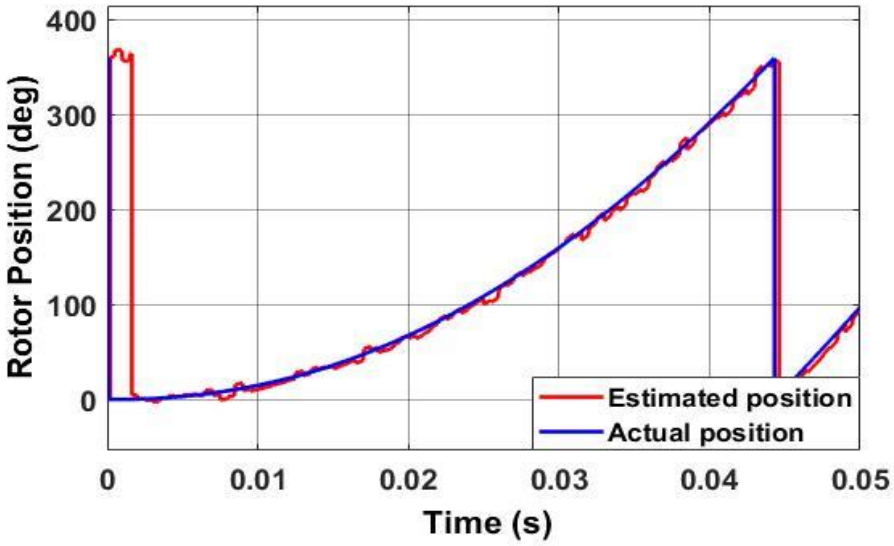

(a)

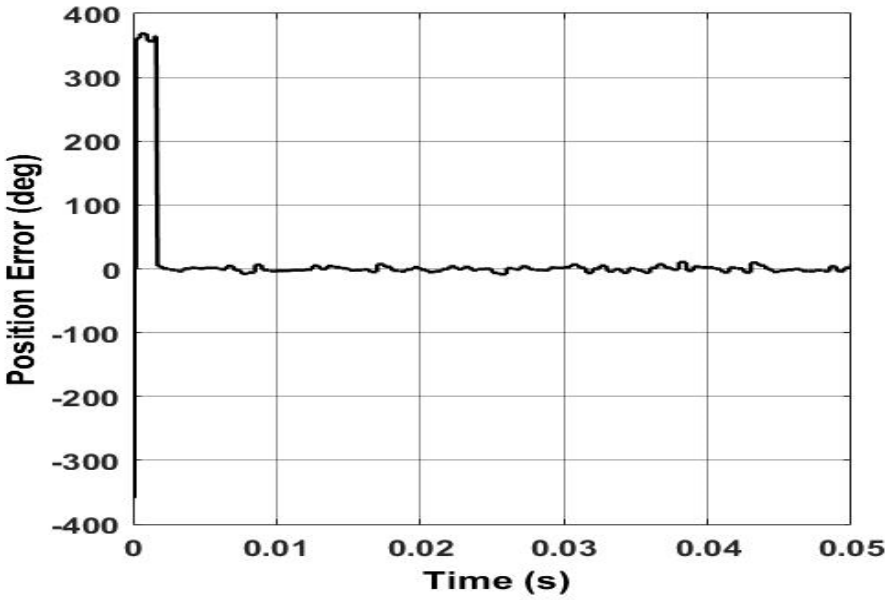

(b)

Figure 6.9: Actual and SMO estimation at low speed (a) rotor position (b) Position error

Table 6.2 summarized the performance of the traditional SMO at several speeds. It shows the absolute values of the average errors. The SMO depicted a good performance in spite the model uncertainties and the errors in feedback signals across a wide range of speed, but it shows poor performance in the estimation of rotor position speed at a standstill and near-zero speeds. A signal injection method is implemented in this region. The phase to be energized is determined by injecting an equal amount of voltage to each phase and comparing their generated maximum current. Nevertheless, the accuracy of the SMO started to decrease above the base speed of the SRM as can be seen from the average error at 900 rpm.

Table 6.2: Average Position and Speed Estimation Error Using SMO

Reference Speed	**Position average error (deg).**
10 rpm (Chopping mode)	241.85
300 rpm (Chopping mode)	2.62
600 rpm (Chopping mode)	3.83
900 rpm (Single pulse mode)	7.46

6.4.2 Results Analysis of Single Sensor Sensorless Control

A MATLAB/Simulink model of the asymmetric half-bridge converter and the single sensor R-Dump converter are developed and analyzed in this section, together with a model of 3-phase

MASRM and the AQSM based torque controller. Additionally, the proposed SMO for the single sensor application employed is based on the one developed in Section 6.4.4.

Figure 6.10 shows the comparison of the SMO based estimated rotor position for the AHBC and the single sensor R-Dump converter. It can be seen from Figure 6.10(a) that the measured and estimated DC-Link current are similar, therefore, the Proposed SMO can produce a good estimation of the rotor position. The SMO only deals with the error dynamics of the DC-Link current in the proposed method which can converge faster and have better robustness than when it deals with the summation of error dynamics of the individual phase currents as in the traditional SMO method. Nevertheless, the estimated rotor position produced by the conventional SMO technique with AHBC presented in Figure 6.10(b) is also good but less accurate compared to the proposed single current sensor SMO with the R-dump.

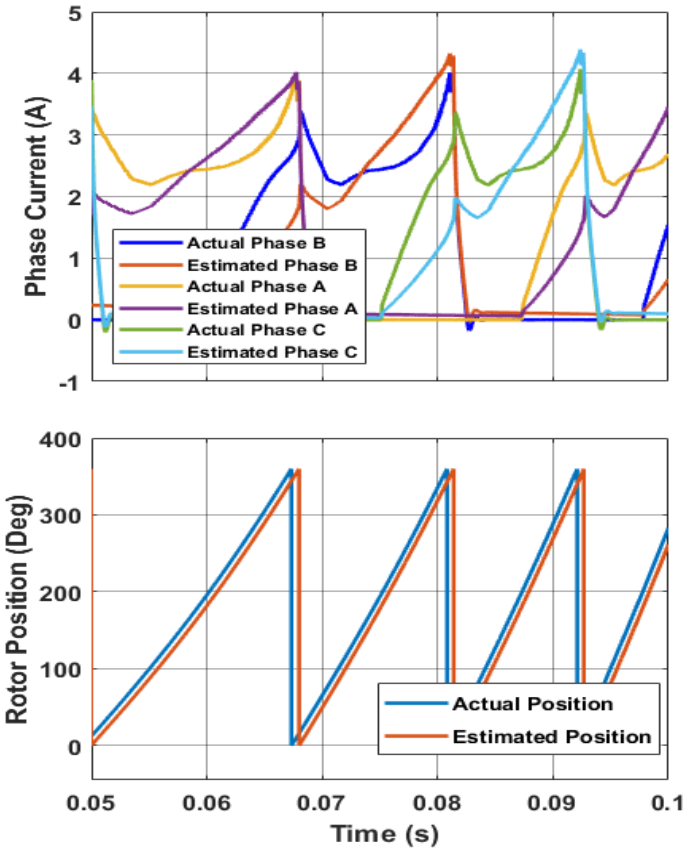

(a)

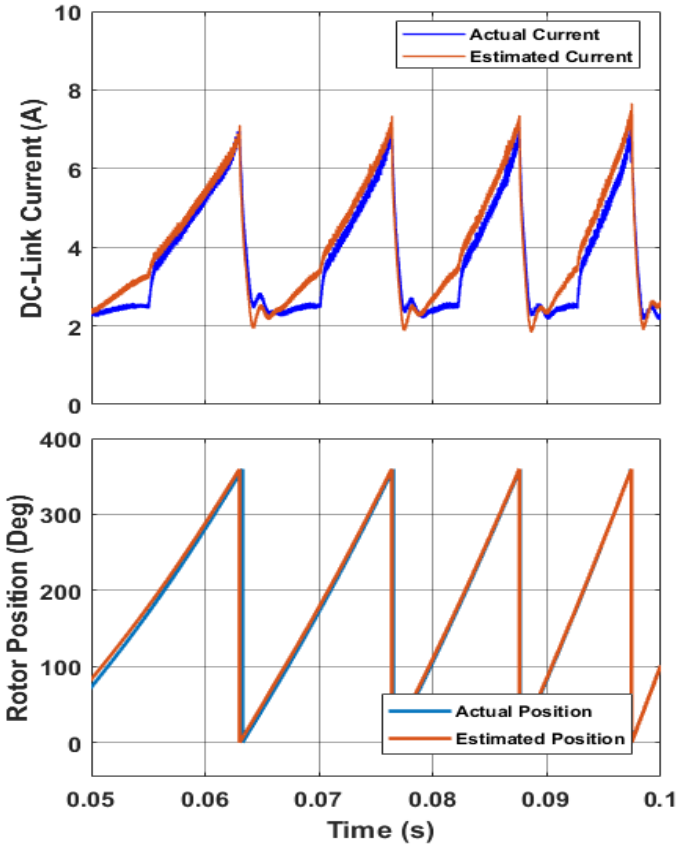

(b)

Figure 6.10: Estimated current and rotor position. (a) With AHBC. (b) With Single sensor R-Dump

The asymmetric half-bridge converter and the single sensor R-Dump converter (R-Dump-SS) is tested on the MASRM drive with the proposed torque control. Figure 6.11 depicts the simulation results of the sensorless systems both at 100rpm and 4Nm torque reference. Figure 6.11(a) shows the current and torque waveforms of the sensorless system with AHBC while Figure 6.11(b) shows the current and torque waveforms of the sensorless system with R-Dump-SS. Comparing the two figures, it can be noticed that the AHBC based system and the R-Dump-SS based system generate different current profiles. Yet, the R-Dump-SS switching principle causes more chattering in phase currents, hence, in the generated resultant torque. This is because the R-Dump converter uses only one switch per phase, therefore, it only has two modes of switching: the turn-on (Magnetization) and turn-off (demagnetization) without the freewheeling mode as in the AHBC. This means the R-Dump operates in hard chopping mode hence its switching losses will increase compared to the AHBC that can operate with soft chopping mode.

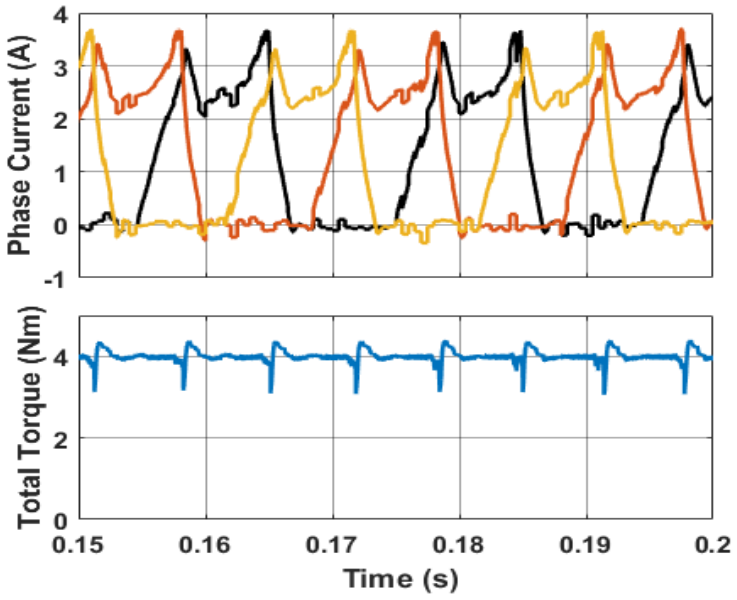

(a)

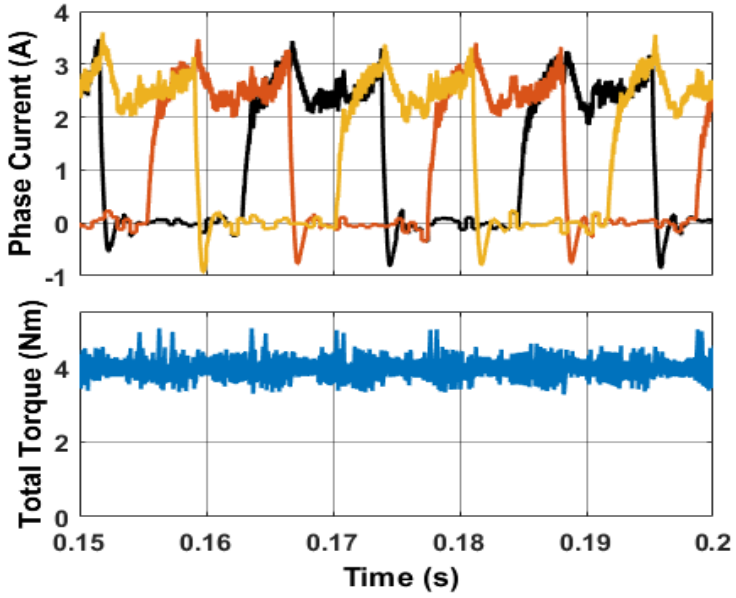

(b)

Figure 6.11: Phase currents and resultant torque at 100 rpm. (a) With AHBC (b) With R-Dump-SS

Figure 6.12 (a) and (b) shows the phase current and resultant torque of the compared drives (AHBC with conventional SMO and R-Dump with modified SMO) at 600 rpm. It is noticeable that both drives produced similar results with regards to the generated torque ripple. The increased torque ripple at this speed is because of the back EMF because 600 rpm is within the field weakening region of the test MASRM. The comparison of the performance of the drives is presented in Table 6.3. The proposed R-Dump-SS topology, the single sensor SMO position estimation method, and the AQSM torque control, can significantly reduce the size, weight and

cost of the MASRM drive with improved reliability at the price of a small increase in torque ripple and decrease in efficiency.

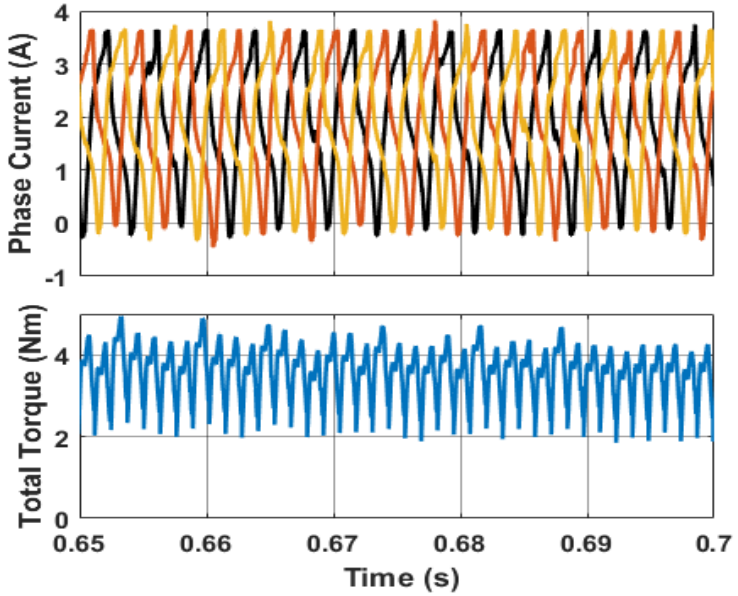

(a)

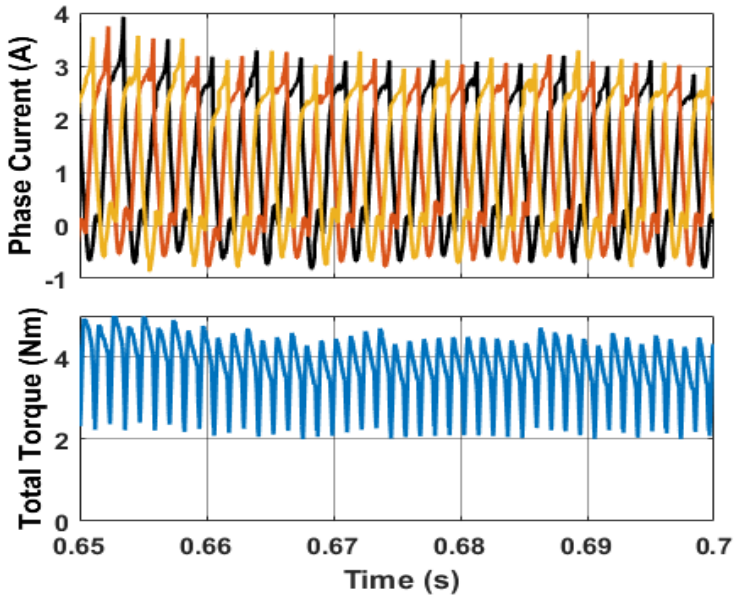

(b)

Figure 6.12: Measured Phase currents and resultant torque at 600 rpm. (a) With AHBC (b) With R-Dump-SS

Table 6.3 Performance comparison

Parameters	**SMO using AHBC**	**SMO using R-Dump-SS**
Average Estimated Current Error (A)	1.55	0.26
Average Estimated Position Error (Deg)	3.40	1.75
Normalized Peak to Peak Torque ripple (%)	30.68	38.45

6.5 Summary

The traditional electric drive needed to operate MASRM often reduces the drives reliability and increases its cost and volume. So, sensorless torque control of MASRM drive using a Resistor-Dump converter with a single current sensor is proposed in this study. The proposed drive has minimal power component and transducer count compared to commonly use power converters like the asymmetric half-bridge converter. The proposed sensorless control method utilizes a single current measurement and a modified sliding mode observer to estimate the rotor position of the MASRM instead of using individual current measurements for each phase. The proposed sensorless electric drive can improve the system reliability, and reduced the number of components, with non-significant compromise in torque characteristics and efficiency.

CHAPTER 7

CONCLUSIONS AND FUTURE WORK

The impact of the breakthroughs in electrical/mechatronics technology is increasing the rate of change in electrical drive systems. This change is driven forward by research and development in power conversion and drive control techniques in terms of system dynamics and design packaging. In many drive systems, the conventional combustion, hydraulic and pneumatic actuated system are replaced by electrical drives. Moreover, a reliable, fault-tolerant, and efficient operation of the electric drives in almost all the areas of application is highly desired. This project investigated the torque ripple minimization, complexity, reliability, and size of SRM drives. The main findings of this research are summarised in this chapter and suggested future work is also presented.

7.1 Summary

Switched reluctance machines have the inherent advantages of suitability for harsh environments, fault-tolerance, low cost, and ability to operate over a wide range of speed. These characteristics make SRM a good choice for many actuation systems. Nonetheless, it has limitations such as torque ripple caused by saturation, nonlinear torque characteristics and current commutation, low torque density compared to permanent magnet machines, and it suffers from high acoustic noise due to the inhomogeneous radial flux density distribution in the airgap and the torque generation mechanics. Advancement in modern technology can currently favour the wide adoption of SRMs despite its inherent limitations. Therefore, the principal aim of this research is the design, development and, implementation of torque control for a unique switched reluctance motor drive with multi-objective of achieving zero toque error, minimal torque ripple, high reliability and robustness, and lower size, weight, and cost of implementation.

In order to achieve this aim, commonly used control systems were identified from literature review including current hysteresis control, direct torque control and direct instantaneous torque control methods, which were used to obtain desired torque characteristics like optimal toque density and minimized torque ripple. These control methods were simulated and used as benchmark in this study. A test rig comprising an MASRM driven by an asymmetric converter is constructed to analyse, test and validate the proposed torque control method through the comparison of its performance with that of direct instantaneous torque control, and current hysteresis control methods. The characteristic modelling and analysis for the behaviour of MASRM has been done using experimental data and mathematical formulation, which were

then used to develop a simulation model of the overall 3- phase MASRM drive in MATLAB/Simulink. Since the machine used and the multi-objective control proposed in this research are unique, the relative algorithms on torque control, torque-ripple minimization, and sensorless control are different from those proposed by other researchers.

Encoder-based and sensorless torque control techniques have been investigated and the main findings are summarised for these two cases in the next two sections, respectively.

7.2 Encoder Based Torque Control

A model of the 3-phase magnet assisted switched reluctance machine drive is developed in MATLAB/Simulink based on its magnetic characteristics and presented in the form of phase voltage equations and torque equations. The MASRM model is developed from the experimental data that represent the relationship between the flux-current-rotor position and the torque-current-rotor position. The model is used for both torque control development and analysis. Another model is developed for a sliding mode-based rotor position estimation of the MASRM, which is based on a Fourier series approximation and the experimental data.

Reliability is of great importance in almost all applications in which switched reluctance machines are employed. Thus, the overall reliability of the control system should be ensured. Therefore, the relationship between, reliability, complexity, and performance of several widely used SRM drive control methods were investigated (using theoretical and analytical methods) based on their applications on the proposed MASRM drive. The investigation of the relationship between the complexity and reliability of MASRM control methods is carried out based on a matric of information flow complexity within the control techniques. The results obtained depicted that HCC method shows the highest robustness to measurement error followed by DITC method then DTC method, but the HCC has poor torque ripple reduction capability compared to the two torque control methods. Torque control methods such as DITC and DTC can provide an improved torque ripple reduction. Nevertheless, the DTC was found to have significantly less robustness to measurement noise and errors, followed by the DITC then the HCC. This is because the DTC has higher structural complexity increased the dependency of its accuracy to the accuracy of the feedback signal.

A new adaptive quasi sliding mode torque control for the MASRM drive is developed based on the findings from the complexity and reliability studies. It is designed to be a simple and

intuitive control technique that regulates the machine's torque error to zero while maintaining the switching frequency and the phase currents within desired constraints, despite the steeper mid, and more saturated align and unaligned inductance profile of the MASRM.

DTC and DITC are the popular torque control methods used in minimizing torque ripple in SRM drives. However, these torque control methods, compared to the conventional hysteresis current control method, require the use of power devices with a higher rating of about 150% to achieve the torque ripple reduction. Thus, these requirements leads to added extra cost of implementation, conduction loss, and stress on the drive's semiconductors and machine winding. To overcome these limitations, the proposed AQSM controller is a torque characteristics regulator with included magnitude and rate of change constraints on the control action. Thus, it overcomes the limitations common to torque control methods such as high switching frequency requirement, and high current demand near aligned and unaligned rotor position. Furthermore, a PWM based power device switching method is proposed for the controller instead of the conventional hysteresis switching, to handle the increased degree of freedom of the proposed torque regulator.

Injecting 10% error signal to phase current measurement of the MASRM with the HCC method caused 4% and 8% increase in peak to peak torque at low speed and based speed, respectively. For the DITC method, the same injected error caused 12% and 3% increase in peak to peak torque at low speed and based speed, respectively. Besides, in the DTC method, the same error signal produced 257% and 216% increase in peak to peak torque at low speed and based speed, respectively, which is significantly larger compared to the HCC and DITC method. This is because the DTC algorithm depends on both phase-current and phase-voltage measurements and with the error signal added to each, the higher number of sub-modules in the DTC algorithm including the flux and torque estimations produced erroneous values, hence, the zone selector can select a wrong switching sequence which can cause torque spikes as depicted.

In addition, as the information flow complexity of the three methods is calculated based on their module system structures to determine the differences in complexity between the control methods. The results obtained show that the HCC. DITC, DTC, and AQSM have information flow complexity of 158, 508, 613 and 458, respectively It can be observed that the complexity of the control methods is proportional to the number of sub-modules involved in the system. This method of analysis helped in the design of the AQSM controller considering the importance of reducing complexity and failure-rate of control algorithms by finding

dispensable functions/sub-modules. Therefore, minimizing computational time of the AQSM and improving its reliability.

An experimental setup and results for the proposed torque controller based on a new Adaptive Quasi Sliding Mode Control method for MASRM drive were presented. The experimental results confirmed that the proposed torque control method has the advantage of providing good torque characteristics without having the limitations of most SRM torque control methods such as high switching frequency requirement, and high phase current demand.

By testing the MASRM drive at low speed (100 rpm), the proposed method offers much less torque ripple of 20.3% compared to 49.6% and 67.5% of the DITC and HCC, respectively. Also, a better torque ripple reduction is achieved by the proposed AQSM method at speed of 600rpm (above the base speed of the drive) with the measured torque ripple for the AQSM recorded to be 40.7% compared to 65.4% and 89.3% with the DITC and HCC, respectively.

The results obtained showed that the AQSM methods show the better robustness to measurement error while the DITC method shows significant performance degradation. In addition, the simulation and experimental results verified that the proposed AQSM control method can significantly reduce the torque ripple of the MASRM drive across its range of speed, compared to the HCC method and the DITC method. Therefore, the proposed adaptive quasi sliding mode torque control method enables the reduction of losses and thermal effects on the power devices and their over-rating. In addition, it also enables the reduction in computational cost and sensitivity to measurement errors because it requires no online dynamic-model computation of the machine and no extra current limiter control loop, hence reducing the digital processing cost.

7.3 Sensorless Torque Control

The common power converter needed to operate an SRM drive increases its cost and volume, and also reduces its running reliability. Therefore, sensorless torque control of MASRM drive using an asymmetric half-bridge converter and Resistor-Dump converter with a single current sensor is studied in this research work. The proposed drive use single sensor Resistor-Dump converter has minimal power components compared to mostly use converters like an asymmetric half-bridge converter. It utilizes a single current measurement to estimate the rotor

position of the SRM instead of using individual current measurements for each phase and also one switch and one diode per phase.

By comparing the simulated results, the following performance of the SMO using AHBC and the Single sensor SMO with R-Dump converter was observed. The average estimated current error in the traditional SMO with AHBC and the proposed single sensor SMO with R-Dump is 1.55A and 0.26A, respectively. Furthermore, the average estimated position error in the traditional SMO with AHBC and the proposed single sensor SMO with R-Dump is 3.40deg and 1.75deg, respectively. In addition, the normalized peak to peak torque ripple in the traditional SMO with AHBC and the proposed single sensor SMO with R-Dump is 1.55A and 0.26A, respectively. The results show that the proposed converter topology, torque control, and position estimation methods can improve the system reliability, reduce the size and cost of SRM drives however the R-dump converter reduces the drive efficiency.

7.4 Future Work

This research work covers most of the problems related to the development and implementation of a switched reluctance motor based electrical drive system. However, there still some aspects of this particular research project that can be improved in the future. There are also many areas of contributions related to SRM/MASRM drives that need more investigation and research work in the future. The main aspect of this project that need more investigation in the future are:

- The sensorless control method developed in Chapter 6 needs to be implemented and verified on experimental test rig across the full speed range of the MASRM. Due to time limitation, only the experimental work of the proposed torque controller with rotor position measurement has been carried out.
- The proposed low-count power device converter based MASRM drive needs to be implemented and integrated with the proposed sensorless torque control method for experimental verification.
- The performance evaluation of the proposed torque control for very low speed applications like electro-mechanical braking system and ultra-high-speed applications like electric dryers should be carried out as the MASRM used in this study is designed for fault tolerant nose-wheel aerospace application.

Broader applications of SRMs are mainly limited by the large torque ripple, high acoustic noise, mediocre power density, and low efficiency over its entire range of operation. Within the general area of SRM/MASRM drives, there are many areas that need more investigations including:

- Further investigation on employment of low device count converters with less efficiency reduction that can leverage the proposed single current sensor based sensorless control is to be carried out.
- More investigation on control system reliability and robustness assessment, and development of more accurate measures in addition to information flow complexity is to be carried out.
- Assessment of employing wide band gap semiconductors with high switching frequency and soft switching to increase power density of SRM/MASRM drives is needed be carried out.
- Efficient and reliable methods for torque ripple reduction in SRM/MASRM under converter fault conditions including open- and short-circuit faults should be investigated by utilizing fewer power devices.
- Integration of online condition monitoring for predicting faults in SRM/MASRM drives for safety critical applications needs to be investigated.

REFERENCES

[1] M. Krishnamurthy, C. S. Edrington, A. Emadi, P. Asadi, M. Ehsani, and B. Fahimi, "Making the case for applications of switched reluctance motor technology in automotive products," *IEEE Transactions on power electronics,* vol. 21, no. 3, pp. 659-675, 2006.

[2] A. Mitra and A. Emadi, "On the suitability of large switched reluctance machines for propulsion applications," in *2012 IEEE Transportation Electrification Conference and Expo (ITEC)*, 2012: IEEE, pp. 1-5.

[3] K. M. Rahman, B. Fahimi, G. Suresh, A. V. Rajarathnam, and M. Ehsani, "Advantages of switched reluctance motor applications to EV and HEV: Design and control issues," *IEEE transactions on industry applications,* vol. 36, no. 1, pp. 111-121, 2000.

[4] A. Emadi, *Handbook of automotive power electronics and motor drives*. CRC press, 2017.

[5] L. Maharjan, D. He, N. Arbab, and B. Fahimi, "Low-Cost Drive for Switched Reluctance Machine Using Piezoelectric Actuators," *IEEE Journal of Emerging and Selected Topics in Power Electronics,* vol. 7, no. 4, pp. 2232-2242, 2018.

[6] Q. Sun, J. Wu, C. Gan, and J. Guo, "Modular full-bridge converter for three-phase switched reluctance motors with integrated fault-tolerance capability," *IEEE Transactions on Power Electronics,* vol. 34, no. 3, pp. 2622-2634, 2018.

[7] X. Deng, B. Mecrow, H. Wu, R. Martin, and Y. Gai, "Cost-Effective and High-Efficiency Variable-Speed Switched Reluctance Drives With Ring-Connected Winding Configuration," *IEEE Transactions on Energy Conversion,* vol. 34, no. 1, pp. 120-129, 2018.

[8] J. Cai, Z. Liu, and Y. Zeng, "Aligned position estimation based fault-tolerant sensorless control strategy for SRM drives," *IEEE Transactions on Power Electronics,* vol. 34, no. 8, pp. 7754-7762, 2018.

[9] J. B. Bartolo, M. Degano, J. Espina, and C. Gerada, "Design and initial testing of a high-speed 45-kW switched reluctance drive for aerospace application," *IEEE Transactions on Industrial Electronics,* vol. 64, no. 2, pp. 988-997, 2016.

[10] W. Lee, S. Li, D. Han, B. Sarlioglu, T. A. Minav, and M. Pietola, "A review of integrated motor drive and wide-bandgap power electronics for high-performance electro-hydrostatic actuators," *IEEE transactions on transportation electrification,* vol. 4, no. 3, pp. 684-693, 2018.

[11] S. McDonald, G. Atkinson, R. Martin, and S. Ullah, "Magnetically biased inductor for an aerospace switched reluctance drive," in *2015 IEEE International Electric Machines & Drives Conference (IEMDC)*, 2015: IEEE, pp. 1272-1278.

[12] B. Fahimi, A. Emadi, and R. B. Sepe, "A switched reluctance machine-based starter/alternator for more electric cars," *IEEE Transactions on Energy Conversion,* vol. 19, no. 1, pp. 116-124, 2004.

[13] D. A. Torrey, "Switched reluctance generators and their control," *IEEE Transactions on industrial electronics,* vol. 49, no. 1, pp. 3-14, 2002.

[14] Y. Tang and J. A. Kline, "Modeling and design optimization of switched reluctance machine by boundary element analysis and simulation," *IEEE transactions on energy conversion,* vol. 11, no. 4, pp. 673-680, 1996.

[15] C. Gan, J. Wu, Q. Sun, W. Kong, H. Li, and Y. Hu, "A review on machine topologies and control techniques for low-noise switched reluctance motors in electric vehicle applications," *IEEE Access,* vol. 6, pp. 31430-31443, 2018.
[16] K. Tomczewski and K. Wrobel, "Improved C-dump converter for switched reluctance motor drives," *IET power electronics,* vol. 7, no. 10, pp. 2628-2635, 2014.
[17] Y. Hu, T. Wang, and W. Ding, "Performance evaluation on a novel power converter with minimum number of switches for a six-phase switched reluctance motor," *IEEE Transactions on Industrial Electronics,* vol. 66, no. 3, pp. 1693-1702, 2018.
[18] S. Ullah, S. P. McDonald, R. Martin, M. Benarous, and G. J. Atkinson, "A permanent magnet assist, segmented rotor, switched reluctance drive for fault tolerant aerospace applications," *IEEE Transactions on Industry Applications,* vol. 55, no. 1, pp. 298-305, 2018.
[19] E. F. Farahani, M. A. J. Kondelaji, and M. Mirsalim, "A new exterior-rotor multiple teeth switched reluctance motor with embedded permanent magnets for torque enhancement," *IEEE Transactions on Magnetics,* vol. 56, no. 2, pp. 1-5, 2020.
[20] J. Cho, J. Hur, and C. Lee, "Control scheme of a novel permanent-magnet-assisted switched reluctance machine," in *2013 International Conference on Electrical Machines and Systems (ICEMS)*, 2013: IEEE, pp. 615-621.
[21] B. Fahimi, "On the suitability of switched reluctance drives for starter/generator application," in *Vehicular Technology Conference. IEEE 55th Vehicular Technology Conference. VTC Spring 2002 (Cat. No. 02CH37367)*, 2002, vol. 4: IEEE, pp. 2070-2075.
[22] C.-L. Tseng, S.-Y. Wang, S.-C. Chien, and C.-Y. Chang, "Development of a self-tuning TSK-fuzzy speed control strategy for switched reluctance motor," *IEEE Transactions on Power Electronics,* vol. 27, no. 4, pp. 2141-2152, 2011.
[23] J. Chai and C. Liaw, "Reduction of speed ripple and vibration for switched reluctance motor drive via intelligent current profiling," *IET Electric Power Applications,* vol. 4, no. 5, pp. 380-396, 2010.
[24] J. Ye, B. Bilgin, and A. Emadi, "An offline torque sharing function for torque ripple reduction in switched reluctance motor drives," *IEEE Transactions on energy conversion,* vol. 30, no. 2, pp. 726-735, 2015.
[25] P. K. Reddy, D. Ronanki, and P. Parthiban, "Direct torque and flux control of switched reluctance motor with enhanced torque per ampere ratio and torque ripple reduction," *Electronics Letters,* vol. 55, no. 8, pp. 477-478, 2019.
[26] J. Furqani, M. Kawa, C. A. Wiguna, N. Kawata, K. Kiyota, and A. Chiba, "Current Reference Selection for Acoustic Noise Reduction in Two Switched Reluctance Motors by Flattening Radial Force Sum," *IEEE Transactions on Industry Applications,* vol. 55, no. 4, pp. 3617-3629, 2019.
[27] M. L. M. Kimpara *et al.*, "Active Cancellation of Vibration in Switched Reluctance Motor Using Mechanical Impulse Response Method," *IEEE Transactions on Energy Conversion,* vol. 34, no. 3, pp. 1358-1368, 2019.
[28] B. Anvari, H. A. Toliyat, and B. Fahimi, "Simultaneous optimization of geometry and firing angles for in-wheel switched reluctance motor drive," *IEEE Transactions on Transportation Electrification,* vol. 4, no. 1, pp. 322-329, 2017.
[29] C. Mademlis and I. Kioskeridis, "Performance optimization in switched reluctance motor drives with online commutation angle control," *IEEE Transactions on Energy Conversion,* vol. 18, no. 3, pp. 448-457, 2003.

[30] X. Xue *et al.*, "Optimal control method of motoring operation for SRM drives in electric vehicles," *IEEE Transactions on vehicular technology*, vol. 59, no. 3, pp. 1191-1204, 2010.
[31] H. Li, B. Bilgin, and A. Emadi, "An improved torque sharing function for torque ripple reduction in switched reluctance machines," *IEEE Transactions on Power Electronics*, vol. 34, no. 2, pp. 1635-1644, 2018.
[32] X. Xue, K. Cheng, and S. Ho, "Optimization and evaluation of torque-sharing functions for torque ripple minimization in switched reluctance motor drives," *IEEE transactions on power electronics*, vol. 24, no. 9, pp. 2076-2090, 2009.
[33] X. Deng, B. Mecrow, H. Wu, and R. Martin, "Design and development of low torque ripple variable-speed drive system with six-phase switched reluctance motors," *IEEE Transactions on Energy Conversion*, vol. 33, no. 1, pp. 420-429, 2017.
[34] X. Zhang and G. H. B. Foo, "Overmodulation of constant-switching-frequency-based DTC for reluctance synchronous motors incorporating field-weakening operation," *IEEE Transactions on Industrial Electronics*, vol. 66, no. 1, pp. 37-47, 2018.
[35] X. Zhao, A. Xu, and W. Zhang, "Research on DTC system with variable flux for switched reluctance motor," *CES Transactions on Electrical Machines and Systems*, vol. 1, no. 2, pp. 199-206, 2017.
[36] X. Ai-de, Z. Xianchao, H. Kunlun, and C. Yuzhao, "Torque-ripple reduction of SRM using optimised voltage vector in DTC," *IET Electrical Systems in Transportation*, vol. 8, no. 1, pp. 35-43, 2018.
[37] A. Klein-Hessling, A. Hofmann, and R. W. De Doncker, "Direct instantaneous torque and force control: a control approach for switched reluctance machines," *IET Electric Power Applications*, vol. 11, no. 5, pp. 935-943, 2017.
[38] H. Zeng, H. Chen, and J. Shi, "Direct instantaneous torque control with wide operating range for switched reluctance motors," *IET Electric Power Applications*, vol. 9, no. 9, pp. 578-585, 2015.
[39] N. Dankadai, M. Elgendy, S. McDonald, D. Atkinson, and G. Atkinson, "Investigation of Reliability and Complexity of Torque Control for Switched Reluctance Drives," in *2019 IEEE Conference on Power Electronics and Renewable Energy (CPERE)*, 2019: IEEE, pp. 485-490.
[40] S. Yao and W. Zhang, "A simple strategy for parameters identification of SRM direct instantaneous torque control," *IEEE Transactions on Power Electronics*, vol. 33, no. 4, pp. 3622-3630, 2017.
[41] D. Shah, M. Hilairet, and I. Bahri, "Enhanced direct instantaneous torque control of switched reluctance machine with phase current limitation," in *IECON 2013-39th Annual Conference of the IEEE Industrial Electronics Society*, 2013: IEEE, pp. 2780-2785.
[42] P. Dubravka, P. Rafajdus, P. Makys, and L. Szabo, "Control techniques for torque ripple minimization in switched reluctance drives under faults," in *2016 International Symposium on Power Electronics, Electrical Drives, Automation and Motion (SPEEDAM)*, 2016: IEEE, pp. 625-632.
[43] I. Ralev, F. Qi, B. Burkhart, A. Klein-Hessling, and R. W. De Doncker, "Impact of smooth torque control on the efficiency of a high-speed automotive switched reluctance drive," *IEEE Transactions on industry applications*, vol. 53, no. 6, pp. 5509-5517, 2017.
[44] U. Jakobsen, K. Lu, P. O. Rasmussen, D.-H. Lee, and J.-W. Ahn, "Sensorless control of low-cost single-phase hybrid switched reluctance motor drive," *IEEE Transactions on Industry Applications*, vol. 51, no. 3, pp. 2381-2387, 2014.

[45] C. Gan, J. Wu, Y. Hu, S. Yang, W. Cao, and J. L. Kirtley, "Online sensorless position estimation for switched reluctance motors using one current sensor," *IEEE Transactions on Power Electronics,* vol. 31, no. 10, pp. 7248-7263, 2015.
[46] C. J. Bateman, B. C. Mecrow, A. C. Clothier, P. P. Acarnley, and N. D. Tuftnell, "Sensorless operation of an ultra-high-speed switched reluctance machine," *IEEE Transactions on Industry Applications,* vol. 46, no. 6, pp. 2329-2337, 2010.
[47] M. Ehsani and B. Fahimi, "Elimination of position sensors in switched reluctance motor drives: state of the art and future trends," *IEEE Transactions on industrial electronics,* vol. 49, no. 1, pp. 40-47, 2002.
[48] H. Gao, F. R. Salmasi, and M. Ehsani, "Inductance model-based sensorless control of the switched reluctance motor drive at low speed," *IEEE Transactions on power electronics,* vol. 19, no. 6, pp. 1568-1573, 2004.
[49] S. Li, S. Zhang, T. G. Habetler, and R. G. Harley, "Modeling, Design Optimization, and Applications of Switched Reluctance Machines—A Review," *IEEE Transactions on Industry Applications,* vol. 55, no. 3, pp. 2660-2681, 2019.
[50] G.-Z. Cao, N. Chen, S.-D. Huang, S.-S. Xiao, and J. He, "Nonlinear modeling of the flux linkage in 2-D plane for the planar switched reluctance motor," *IEEE Transactions on Magnetics,* vol. 54, no. 11, pp. 1-5, 2018.
[51] A. Nirgude, M. Murali, N. Chaithanya, S. Kulkarni, V. Bhole, and S. R. Patel, "Nonlinear mathematical modeling and simulation of Switched Reluctance Motor," in *2016 IEEE International Conference on Power Electronics, Drives and Energy Systems (PEDES)*, 2016: IEEE, pp. 1-6.
[52] F. J. Perez-Cebolla, A. Martinez-Iturbe, B. Martín-del-Brío, C. Bernal, and A. Bono-Nuez, "Nonlinear lumped-circuit model for switched reluctance motors exhibiting core losses," *IEEE Transactions on Industrial Electronics,* vol. 63, no. 6, pp. 3433-3445, 2016.
[53] J. Dang, J. R. Mayor, S. A. Semidey, R. Harley, T. Habetler, and J. Restrepo, "Practical considerations for the design and construction of a high speed SRM with a flux-bridge rotor," in *2014 IEEE Energy Conversion Congress and Exposition (ECCE)*, 2014: IEEE, pp. 3842-3849.
[54] C. Lu, P. Zhou, D. Lin, B. He, and D. Sun, "Multiply Connected 3-D Transient Problem With Rigid Motion Associated With $\mbi T\hbox {-}\mmb\Omega $ Formulation," *IEEE transactions on magnetics,* vol. 50, no. 2, pp. 449-452, 2014.
[55] S. J. Salon, *Finite element analysis of electrical machines*. Kluwer academic publishers Boston, 1995.
[56] P. Zhou, B. He, C. Lu, D. Lin, and N. Chen, "Transient simulation of electrical machines using time decomposition method," in *2017 IEEE International Electric Machines and Drives Conference (IEMDC)*, 2017: IEEE, pp. 1-6.
[57] A. G. Jack, J. W. Finch, and J. P. Wright, "Adaptive mesh generation applied to switched-reluctance motor design," *IEEE transactions on industry applications,* vol. 28, no. 2, pp. 370-375, 1992.
[58] M. B. Fauchez, "Magnetic analysis of a switched reluctance motor using a boundary element-finite element coupling method," *IEEE Transactions on Magnetics,* vol. 24, no. 1, pp. 475-478, 1988.
[59] T. C. O'Connell and P. T. Krein, "A time-harmonic three-dimensional vector boundary element model for electromechanical devices," *IEEE Transactions on Energy Conversion,* vol. 25, no. 3, pp. 606-618, 2010.

[60] A. D. Brovont, "Exploring the boundary element method for optimization-based machine design," in *2017 IEEE International Electric Machines and Drives Conference (IEMDC)*, 2017: IEEE, pp. 1-7.
[61] D. M. Araujo, J.-L. Coulomb, O. Chadebec, and L. Rondot, "A hybrid boundary element method-reluctance network method for open boundary 3-D nonlinear problems," *IEEE transactions on magnetics*, vol. 50, no. 2, pp. 77-80, 2014.
[62] W. Yao, J.-M. Jin, and P. T. Krein, "A highly efficient domain decomposition method applied to 3-D finite-element analysis of electromechanical and electric machine problems," *IEEE Transactions on Energy Conversion*, vol. 27, no. 4, pp. 1078-1086, 2012.
[63] D. Lin, P. Zhou, Q. Chen, N. Lambert, and Z. Cendes, "The effects of steel lamination core losses on 3D transient magnetic fields," *IEEE Transactions on Magnetics*, vol. 46, no. 8, pp. 3539-3542, 2010.
[64] S. Song, M. Zhang, and L. Ge, "A new fast method for obtaining flux-linkage characteristics of SRM," *IEEE Transactions on Industrial Electronics*, vol. 62, no. 7, pp. 4105-4117, 2015.
[65] Z. Lin, D. S. Reay, and B. Zhou, "Experimental measurement of switched reluctance motor non-linear characteristics," in *IECON 2013-39th Annual Conference of the IEEE Industrial Electronics Society*, 2013: IEEE, pp. 2827-2832.
[66] Z. Zhang, S. Rao, and X. Zhang, "Performance prediction of switched reluctance motor using improved generalized regression neural networks for design optimization," *CES Transactions on Electrical Machines and Systems*, vol. 2, no. 4, pp. 371-376, 2018.
[67] Y. Li, Q. Ma, and P. Xu, "Improved general modelling method of SRMs based on normalised flux linkage," *IET Electric Power Applications*, vol. 14, no. 2, pp. 316-324, 2019.
[68] S. Song, L. Ge, and M. Zhang, "Data-reconstruction-based modeling of SRM with few flux-linkage samples from torque-balanced measurement," *IEEE Transactions on Energy Conversion*, vol. 31, no. 2, pp. 424-435, 2016.
[69] X.-D. Xue, K. Cheng, and S. Ho, "Simulation of switched reluctance motor drives using two-dimensional bicubic spline," *IEEE Transactions on Energy Conversion*, vol. 17, no. 4, pp. 471-477, 2002.
[70] X. Xue, K. Cheng, and S. Ho, "A position stepping method for predicting performances of switched reluctance motor drives," *IEEE transactions on energy conversion*, vol. 22, no. 4, pp. 839-847, 2007.
[71] J. Stephenson and J. Corda, "Computation of torque and current in doubly salient reluctance motors from nonlinear magnetisation data," in *Proceedings of the Institution of Electrical Engineers*, 1979, vol. 126, no. 5: IET, pp. 393-396.
[72] D. Pulle, "New data base for switched reluctance drive simulation," in *IEE Proceedings B (Electric Power Applications)*, 1991, vol. 138, no. 6: IET, pp. 331-337.
[73] L. Shen, J. Wu, S. Yang, and X. Huang, "Fast flux linkage measurement for switched reluctance motors excluding rotor clamping devices and position sensors," *IEEE Transactions on Instrumentation and Measurement*, vol. 62, no. 1, pp. 185-191, 2012.
[74] S. Song, M. Zhang, and L. Ge, "A new decoupled analytical modeling method for switched reluctance machine," *IEEE Transactions on Magnetics*, vol. 51, no. 3, pp. 1-4, 2015.
[75] A. Khalil and I. Husain, "A fourier series generalized geometry-based analytical model of switched reluctance machines," *IEEE transactions on industry applications*, vol. 43, no. 3, pp. 673-684, 2007.

[76] H.-P. Chi, R.-L. Lin, and J.-F. Chen, "Simplified flux-linkage model for switched-reluctance motors," *IEE Proceedings-Electric Power Applications,* vol. 152, no. 3, pp. 577-583, 2005.
[77] W. Cai and F. Yi, "An integrated multiport power converter with small capacitance requirement for switched reluctance motor drive," *IEEE transactions on power electronics,* vol. 31, no. 4, pp. 3016-3026, 2015.
[78] K. Chau, "Switched reluctance motor drives," 2015.
[79] J. Mukhopadhyay, S. Choudhuri, and S. Sengupta, "Drive strategies for switched reluctance motor-A review," 2015.
[80] C. Zhang, K. Wang, S. Zhang, X. Zhu, and L. Quan, "Analysis of variable voltage gain power converter for switched reluctance motor," *IEEE Transactions on Applied Superconductivity,* vol. 26, no. 7, pp. 1-5, 2016.
[81] C. Gan, J. Wu, Y. Hu, S. Yang, W. Cao, and J. M. Guerrero, "New integrated multilevel converter for switched reluctance motor drives in plug-in hybrid electric vehicles with flexible energy conversion," *IEEE Transactions on Power Electronics,* vol. 32, no. 5, pp. 3754-3766, 2016.
[82] K. Chau, *Electric vehicle machines and drives: design, analysis and application*. John Wiley & Sons, 2015.
[83] O. Ellabban and H. Abu-Rub, "Switched reluctance motor converter topologies: A review," in *2014 IEEE International Conference on Industrial Technology (ICIT)*, 2014: IEEE, pp. 840-846.
[84] I. Husain, "Minimization of torque ripple in SRM drives," *IEEE transactions on Industrial Electronics,* vol. 49, no. 1, pp. 28-39, 2002.
[85] N. Yan, X. Cao, and Z. Deng, "Direct torque control for switched reluctance motor to obtain high torque–ampere ratio," *IEEE Transactions on Industrial Electronics,* vol. 66, no. 7, pp. 5144-5152, 2018.
[86] Z. Zhu, B. Lee, L. Huang, and W. Chu, "Contribution of current harmonics to average torque and torque ripple in switched reluctance machines," *IEEE Transactions on Magnetics,* vol. 53, no. 3, pp. 1-9, 2016.
[87] X. Cao, J. Zhou, C. Liu, and Z. Deng, "Advanced control method for a single-winding bearingless switched reluctance motor to reduce torque ripple and radial displacement," *IEEE Transactions on energy conversion,* vol. 32, no. 4, pp. 1533-1543, 2017.
[88] H. Sahraoui, H. Zeroug, and H. Toliyat, "Switched reluctance motor design using neural-network method with static finite-element simulation," *IEEE Transactions on magnetics,* vol. 43, no. 12, pp. 4089-4095, 2007.
[89] J.-H. Choi, S. Kim, J.-M. Shin, J. Lee, and S.-T. Kim, "The multi-object optimization of switched reluctance motor," in *Sixth International Conference on Electrical Machines and Systems, 2003. ICEMS 2003.*, 2003, vol. 1: IEEE, pp. 195-198.
[90] F. Sahin, H. B. Ertan, and K. Leblebicioglu, "Optimum geometry for torque ripple minimization of switched reluctance motors," *IEEE Transactions on Energy Conversion,* vol. 15, no. 1, pp. 30-39, 2000.
[91] J. W. Lee, H. S. Kim, B. I. Kwon, and B. T. Kim, "New rotor shape design for minimum torque ripple of SRM using FEM," *IEEE transactions on magnetics,* vol. 40, no. 2, pp. 754-757, 2004.
[92] G. Li, J. Ojeda, S. Hlioui, E. Hoang, M. Lecrivain, and M. Gabsi, "Modification in rotor pole geometry of mutually coupled switched reluctance machine for torque ripple mitigating," *IEEE Transactions on Magnetics,* vol. 48, no. 6, pp. 2025-2034, 2011.

[93] Y. K. Choi, H. S. Yoon, and C. S. Koh, "Pole-shape optimization of a switched-reluctance motor for torque ripple reduction," *IEEE transactions on magnetics,* vol. 43, no. 4, pp. 1797-1800, 2007.
[94] D.-H. Lee, T. H. Pham, and J.-W. Ahn, "Design and operation characteristics of four-two pole high-speed SRM for torque ripple reduction," *IEEE Transactions on Industrial Electronics,* vol. 60, no. 9, pp. 3637-3643, 2012.
[95] P. C. Desai, M. Krishnamurthy, N. Schofield, and A. Emadi, "Novel switched reluctance machine configuration with higher number of rotor poles than stator poles: Concept to implementation," *IEEE Transactions on industrial electronics,* vol. 57, no. 2, pp. 649-659, 2009.
[96] D. P. Tormey and D. A. Torrey, "A comprehensive design procedure for low torque-ripple variable-reluctance motor drives," in *Conference Record of the 1991 IEEE Industry Applications Society Annual Meeting*, 1991: IEEE, pp. 244-251.
[97] R. Mikail, I. Husain, Y. Sozer, M. S. Islam, and T. Sebastian, "Torque-ripple minimization of switched reluctance machines through current profiling," *IEEE Transactions on Industry Applications,* vol. 49, no. 3, pp. 1258-1267, 2013.
[98] R. Mikail, I. Husain, M. S. Islam, Y. Sozer, and T. Sebastian, "Four-quadrant torque ripple minimization of switched reluctance machine through current profiling with mitigation of rotor eccentricity problem and sensor errors," *IEEE Transactions on Industry Applications,* vol. 51, no. 3, pp. 2097-2104, 2014.
[99] Z. Zhu, X. Liu, and Z. Pan, "Analytical model for predicting maximum reduction levels of vibration and noise in switched reluctance machine by active vibration cancellation," *IEEE Transactions on Energy Conversion,* vol. 26, no. 1, pp. 36-45, 2010.
[100] C. Pollock and C.-Y. Wu, "Acoustic noise cancellation techniques for switched reluctance drives," *IEEE transactions on industry applications,* vol. 33, no. 2, pp. 477-484, 1997.
[101] M. Anwar and O. Husain, "Radial force calculation and acoustic noise prediction in switched reluctance machines," *IEEE Transactions on Industry Applications,* vol. 36, no. 6, pp. 1589-1597, 2000.
[102] S. M. Castano, B. Bilgin, E. Fairall, and A. Emadi, "Acoustic noise analysis of a high-speed high-power switched reluctance machine: Frame effects," *IEEE Transactions on Energy Conversion,* vol. 31, no. 1, pp. 69-77, 2015.
[103] C. Gan, J. Wu, M. Shen, S. Yang, Y. Hu, and W. Cao, "Investigation of skewing effects on the vibration reduction of three-phase switched reluctance motors," *IEEE Transactions on Magnetics,* vol. 51, no. 9, pp. 1-9, 2015.
[104] A. H. Isfahani and B. Fahimi, "Comparison of mechanical vibration between a double-stator switched reluctance machine and a conventional switched reluctance machine," *IEEE Transactions on Magnetics,* vol. 50, no. 2, pp. 293-296, 2014.
[105] K. Kiyota, T. Kakishima, A. Chiba, and M. A. Rahman, "Cylindrical rotor design for acoustic noise and windage loss reduction in switched reluctance motor for HEV applications," *IEEE Transactions on Industry Applications,* vol. 52, no. 1, pp. 154-162, 2015.
[106] H.-Y. Yang, Y.-C. Lim, and H.-C. Kim, "Acoustic noise/vibration reduction of a single-phase SRM using skewed stator and rotor," *IEEE Transactions on Industrial Electronics,* vol. 60, no. 10, pp. 4292-4300, 2012.
[107] W. Cai, P. Pillay, Z. Tang, and A. M. Omekanda, "Low-vibration design of switched reluctance motors for automotive applications using modal analysis," *IEEE Transactions on Industry Applications,* vol. 39, no. 4, pp. 971-977, 2003.

[108] J.-P. Hong, K.-H. Ha, and J. Lee, "Stator pole and yoke design for vibration reduction of switched reluctance motor," *IEEE Transactions on Magnetics,* vol. 38, no. 2, pp. 929-932, 2002.
[109] P. O. Rasmussen, J. H. Andreasen, and J. M. Pijanowski, "Structural stator spacers-a solution for noise reduction of switched reluctance motors," *IEEE Transactions on Industry Applications,* vol. 40, no. 2, pp. 574-581, 2004.
[110] M. Anwar, I. Husain, and A. V. Radun, "A comprehensive design methodology for switched reluctance machines," *IEEE transactions on industry applications,* vol. 37, no. 6, pp. 1684-1692, 2001.
[111] X. Guo, R. Zhong, M. Zhang, D. Ding, and W. Sun, "Resonance Reduction by Optimal Switch Angle Selection in Switched Reluctance Motor," *IEEE Transactions on Industrial Electronics,* vol. 67, no. 3, pp. 1867-1877, 2019.
[112] M. Kawa, K. Kiyota, J. Furqani, and A. Chiba, "Acoustic noise reduction of a high-efficiency switched reluctance motor for hybrid electric vehicles with novel current waveform," *IEEE Transactions on Industry Applications,* vol. 55, no. 3, pp. 2519-2528, 2018.
[113] S. Shin, N. Kawagoe, T. Kosaka, and N. Matsui, "Study on commutation control method for reducing noise and vibration in SRM," *IEEE Transactions on Industry Applications,* vol. 54, no. 5, pp. 4415-4424, 2018.
[114] Z. Zhang, A. M. Bazzi, and J. D. Monte, "A novel PWM-control-based strategy for noise reduction in switched reluctance motors," in *2018 IEEE Transportation Electrification Conference and Expo (ITEC)*, 2018: IEEE, pp. 1017-1022.
[115] Y. Murakami and N. Hoshi, "Vibration and acoustic noise reduction of switched reluctance motor with back electromotive force control," in *2017 19th European Conference on Power Electronics and Applications (EPE'17 ECCE Europe)*, 2017: IEEE, pp. P. 1-P. 10.
[116] J. Furqani, C. A. Wiguna, A. Chiba, O. Gundogmus, M. Elamin, and Y. Sozer, "Analytical and Experimental Verification of Novel Current Waveforms for Noise Reduction in Switched Reluctance Motor," in *2019 IEEE International Electric Machines & Drives Conference (IEMDC)*, 2019: IEEE, pp. 576-583.
[117] J. Furqani, M. Kawa, K. Kiyota, and A. Chiba, "Current waveform for noise reduction of a switched reluctance motor under magnetically saturated condition," *IEEE Transactions on Industry Applications,* vol. 54, no. 1, pp. 213-222, 2017.
[118] H. Makino, T. Kosaka, and N. Matsui, "Digital PWM-control-based active vibration cancellation for switched reluctance motors," *IEEE Transactions on Industry Applications,* vol. 51, no. 6, pp. 4521-4530, 2015.
[119] X. Mininger, E. Lefeuvre, M. Gabsi, C. Richard, and D. Guyomar, "Semiactive and active piezoelectric vibration controls for switched reluctance machine," *IEEE Transactions on Energy conversion,* vol. 23, no. 1, pp. 78-85, 2008.
[120] S. A. Long, Z. Zhu, and D. Howe, "Effectiveness of active noise and vibration cancellation for switched reluctance machines operating under alternative control strategies," *IEEE Transactions on Energy Conversion,* vol. 20, no. 4, pp. 792-801, 2005.
[121] A. Chiba *et al.*, "Torque density and efficiency improvements of a switched reluctance motor without rare-earth material for hybrid vehicles," *IEEE Transactions on Industry Applications,* vol. 47, no. 3, pp. 1240-1246, 2011.
[122] M. Hasegawa, N. Tanaka, A. Chiba, and T. Fukao, "The operation analysis and efficiency improvement of switched reluctance motors with high silicon steel," in

Proceedings of the Power Conversion Conference-Osaka 2002 (Cat. No. 02TH8579), 2002, vol. 3: IEEE, pp. 981-986.

[123] H. Hayashi, K. Nakamura, A. Chiba, T. Fukao, K. Tungpimolrut, and D. G. Dorrell, "Efficiency improvements of switched reluctance motors with high-quality iron steel and enhanced conductor slot fill," *IEEE Transactions on Energy Conversion,* vol. 24, no. 4, pp. 819-825, 2009.

[124] S. H. Won, J. Choi, and J. Lee, "Windage loss reduction of high-speed SRM using rotor magnetic saturation," *IEEE Transactions on Magnetics,* vol. 44, no. 11, pp. 4147-4150, 2008.

[125] V. P. Vujičić, "Minimization of torque ripple and copper losses in switched reluctance drive," *IEEE transactions on power electronics,* vol. 27, no. 1, pp. 388-399, 2012.

[126] I. Kioskeridis and C. Mademlis, "Optimal efficiency control of switched reluctance generators," *IEEE Transactions on power electronics,* vol. 21, no. 4, pp. 1062-1071, 2006.

[127] K. M. Rahman and S. E. Schulz, "High-performance fully digital switched reluctance motor controller for vehicle propulsion," *IEEE Transactions on Industry Applications,* vol. 38, no. 4, pp. 1062-1071, 2002.

[128] K. Ha, C. Lee, J. Kim, R. Krishnan, and S.-G. Oh, "Design and development of low-cost and high-efficiency variable-speed drive system with switched reluctance motor," *IEEE Transactions on Industry Applications,* vol. 43, no. 3, pp. 703-713, 2007.

[129] W. Ding and S. Li, "Maximum ratio of torque to copper loss control for hybrid excited flux-switching machine in whole speed range," *IEEE Transactions on Industrial Electronics,* vol. 66, no. 2, pp. 932-943, 2018.

[130] B. Mirzaeian, M. Moallem, V. Tahani, and C. Lucas, "Multiobjective optimization method based on a genetic algorithm for switched reluctance motor design," *IEEE Transactions on Magnetics,* vol. 38, no. 3, pp. 1524-1527, 2002.

[131] M. Sugiura, Y. Ishihara, H. Ishikawa, and H. Naitoh, "Improvement of efficiency by stepped-skewing rotor for switched reluctance motors," in *2014 International Power Electronics Conference (IPEC-Hiroshima 2014-ECCE ASIA)*, 2014: IEEE, pp. 1135-1140.

[132] J. Faiz and J. W. Finch, "Aspects of design optimisation for switched reluctance motors," *IEEE Transactions on Energy conversion,* vol. 8, no. 4, pp. 704-713, 1993.

[133] X. Song, Y. Park, J. Li, and J. Lee, "Optimization of switched reluctance motor for efficiency improvement using response surface model and kriging model," in *2011 Fourth International Joint Conference on Computational Sciences and Optimization*, 2011: IEEE, pp. 259-260.

[134] I. S. Manolas, A. G. Kladas, and S. N. Manias, "Finite-element-based estimator for high-performance switched reluctance machine drives," *IEEE transactions on magnetics*, vol. 45, no. 3, pp. 1266-1269, 2009.

[135] G. Li, K. Zhang, Z. Zhu, and G. Jewell, "Comparative studies of torque performance improvement for different doubly salient synchronous reluctance machines by current harmonic injection," *IEEE Transactions on Energy Conversion,* vol. 34, no. 2, pp. 1094-1104, 2018.

[136] A. V. Radun, "High-power density switched reluctance motor drive for aerospace applications," *IEEE Transactions on Industry Applications,* vol. 28, no. 1, pp. 113-119, 1992.

[137] S. Brisset and P. Brochet, "Optimization of switched reluctance motors using deterministic methods with static and dynamic finite element simulations," *IEEE Transactions on Magnetics,* vol. 34, no. 5, pp. 2853-2856, 1998.

[138] N. Vattikuti, V. Rallabandi, and B. Fernandes, "A novel high torque and low weight segmented switched reluctance motor," in *2008 IEEE Power Electronics Specialists Conference*, 2008: IEEE, pp. 1223-1228.
[139] K. Tungpimolrut, S. Kachapornkul, P. Jitkreeyarn, P. Somsiri, N. Chayopitak, and C. Akira, "Torque improvement of three-phases full bridge converter based switched reluctance motor with DC assisted winding," in *2012 15th International Conference on Electrical Machines and Systems (ICEMS)*, 2012: IEEE, pp. 1-5.
[140] K. M. Rahman and S. E. Schulz, "Design of high-efficiency and high-torque-density switched reluctance motor for vehicle propulsion," *IEEE Transactions on Industry Applications*, vol. 38, no. 6, pp. 1500-1507, 2002.
[141] B. C. Mecrow, E. A. El-Kharashi, J. W. Finch, and A. G. Jack, "Preliminary performance evaluation of switched reluctance motors with segmental rotors," *IEEE Transactions on Energy Conversion*, vol. 19, no. 4, pp. 679-686, 2004.
[142] A. Labak and N. C. Kar, "A novel five-phase pancake shaped switched reluctance motor for hybrid electric vehicles," in *2009 IEEE Vehicle Power and Propulsion Conference*, 2009: IEEE, pp. 494-499.
[143] K. Kiyota and A. Chiba, "Design of switched reluctance motor competitive to 60-kW IPMSM in third-generation hybrid electric vehicle," *IEEE Transactions on Industry Applications*, vol. 48, no. 6, pp. 2303-2309, 2012.
[144] E. Afjei, A. Siadatan, and H. Torkaman, "Magnetic modeling, prototyping, and comparative study of a quintuple-set switched reluctance motor," *IEEE Transactions on Magnetics*, vol. 51, no. 8, pp. 1-7, 2015.
[145] E. Bostanci, M. Moallem, A. Parsapour, and B. Fahimi, "Opportunities and challenges of switched reluctance motor drives for electric propulsion: A comparative study," *IEEE transactions on transportation electrification*, vol. 3, no. 1, pp. 58-75, 2017.
[146] J. Zhu, K. W. E. Cheng, and X. Xue, "Design and analysis of a new enhanced torque hybrid switched reluctance motor," *IEEE Transactions on Energy Conversion*, vol. 33, no. 4, pp. 1965-1977, 2018.
[147] L. Ge, B. Burkhart, and R. W. De Doncker, "Fast iron loss and thermal prediction method for power density and efficiency improvement in switched reluctance machines," *IEEE Transactions on Industrial Electronics*, vol. 67, no. 6, pp. 4463-4473, 2019.
[148] A. Liu, J. Lou, and S. Yu, "Influence of Exciting Field on Electromagnetic Torque of Novel Switched Reluctance Motor," *IEEE Transactions on Magnetics*, vol. 55, no. 7, pp. 1-7, 2019.
[149] Q. Sun, J. Wu, C. Gan, C. Shi, and J. Guo, "DSSRM design with multiple pole arcs optimization for high torque and low torque ripple applications," *IEEE Access*, vol. 6, pp. 27166-27175, 2018.
[150] H. Kim, C. Nerse, J. Lee, and S. Wang, "Multidisciplinary analysis and multiobjective design optimization of a switched reluctance motor for improving sound quality," *IEEE Access*, vol. 7, pp. 66020-66027, 2019.
[151] W. Yan *et al.*, "Design and multi-objective optimisation of switched reluctance machine with iron loss," *IET Electric Power Applications*, vol. 13, no. 4, pp. 435-444, 2019.
[152] J. G. Amorós, P. Andrada, B. Blanque, and M. Marin-Genesca, "Influence of design parameters in the optimization of linear switched reluctance motor under thermal constraints," *IEEE Transactions on Industrial Electronics*, vol. 65, no. 2, pp. 1875-1883, 2017.

[153] E. Öksüztepe, "In-wheel switched reluctance motor design for electric vehicles by using a pareto-based multiobjective differential evolution algorithm," *IEEE Transactions on Vehicular Technology*, vol. 66, no. 6, pp. 4706-4715, 2016.
[154] S. Zhang, S. Li, J. Dang, R. G. Harley, and T. G. Habetler, "Multi-objective design and optimization of generalized switched reluctance machines with particle swarm intelligence," in *2016 IEEE Energy Conversion Congress and Exposition (ECCE)*, 2016: IEEE, pp. 1-7.
[155] C. Ma, L. Qu, R. Mitra, P. Pramod, and R. Islam, "Vibration and torque ripple reduction of switched reluctance motors through current profile optimization," in *2016 IEEE Applied Power Electronics Conference and Exposition (APEC)*, 2016: IEEE, pp. 3279-3285.
[156] C. Ma and L. Qu, "Multiobjective optimization of switched reluctance motors based on design of experiments and particle swarm optimization," *IEEE Transactions on Energy Conversion*, vol. 30, no. 3, pp. 1144-1153, 2015.
[157] S. Smaka, S. Konjicija, S. Masic, and M. Cosovic, "Multi-objective design optimization of 8/14 switched reluctance motor," in *2013 International Electric Machines & Drives Conference*, 2013: IEEE, pp. 468-475.
[158] Z. Ren, D. Zhang, and C.-S. Koh, "Multi-objective worst-case scenario robust optimal design of switched reluctance motor incorporated with FEM and Kriging," in *2013 International Conference on Electrical Machines and Systems (ICEMS)*, 2013: IEEE, pp. 716-719.
[159] X. Xue, K. W. E. Cheng, T. W. Ng, and N. C. Cheung, "Multi-objective optimization design of in-wheel switched reluctance motors in electric vehicles," *IEEE Transactions on industrial electronics*, vol. 57, no. 9, pp. 2980-2987, 2010.
[160] D. Ilea, M. M. Radulescu, F. Gillon, and P. Brochet, "Multi-objective optimization of a switched reluctance motor for light electric traction applications," in *2010 IEEE Vehicle Power and Propulsion Conference*, 2010: IEEE, pp. 1-6.
[161] X. Huang, Z. Lin, and X. Xiao, "Four-quadrant force control with minimal ripple for linear switched reluctance machines," *CES Transactions on Electrical Machines and Systems*, vol. 4, no. 1, pp. 27-34, 2020.
[162] A. D. Callegaro, B. Bilgin, and A. Emadi, "Radial force shaping for acoustic noise reduction in switched reluctance machines," *IEEE Transactions on Power Electronics*, vol. 34, no. 10, pp. 9866-9878, 2019.
[163] M. M. Borujeni, A. Rashidi, and S. M. S. Nejad, "Optimal four quadrant speed control of switched reluctance motor with torque ripple reduction based on EM-MOPSO," in *The 6th Power Electronics, Drive Systems & Technologies Conference (PEDSTC2015)*, 2015: IEEE, pp. 310-315.
[164] W. Peng, J. J. Gyselinck, J.-W. Ahn, and D.-H. Lee, "Minimal current sensing strategy for switched reluctance machine control with enhanced fault-detection capability," *IEEE Transactions on Industry Applications*, vol. 55, no. 4, pp. 3725-3735, 2019.
[165] A. Kawamura, "Survey of position sensorless switched reluctance motor control," in *Proceedings of IECON'94-20th Annual Conference of IEEE Industrial Electronics*, 1994, vol. 3: IEEE, pp. 1595-1598.
[166] B. Fahimi, G. Suresh, and M. Ehsani, "Review of sensorless control methods in switched reluctance motor drives," in *Conference Record of the 2000 IEEE Industry Applications Conference. Thirty-Fifth IAS Annual Meeting and World Conference on Industrial Applications of Electrical Energy (Cat. No. 00CH37129)*, 2000, vol. 3: IEEE, pp. 1850-1857.

[167] A. D. Cheok and Z. Wang, "DSP-based automated error-reducing flux-linkage-measurement method for switched reluctance motors," *IEEE Transactions on Instrumentation and Measurement*, vol. 56, no. 6, pp. 2245-2253, 2007.
[168] Y. Liang and H. Chen, "Circuit-based flux linkage measurement method with the automated resistance correction for SRM sensorless position control," *IET Electric Power Applications*, vol. 12, no. 9, pp. 1396-1406, 2018.
[169] F. Peng, J. Ye, and A. Emadi, "Position sensorless control of switched reluctance motor based on numerical method," in *2016 IEEE Energy Conversion Congress and Exposition (ECCE)*, 2016: IEEE, pp. 1-8.
[170] W. Wei, Q. Wang, and R. Nie, "Sensorless control of double-sided linear switched reluctance motor based on simplified flux linkage method," *CES Transactions on Electrical machines and Systems*, vol. 1, no. 3, pp. 246-253, 2017.
[171] R. Zhong, Y. Wang, and Y. Xu, "Position sensorless control of switched reluctance motors based on improved neural network," *IET Electric Power Applications*, vol. 6, no. 2, pp. 111-121, 2012.
[172] S. Rehman and D. G. Taylor, "Issues in position estimation of SR motors," in *PESC Record. 27th Annual IEEE Power Electronics Specialists Conference*, 1996, vol. 1: IEEE, pp. 337-343.
[173] A. D. Cheok and N. Ertugrul, "High robustness and reliability of fuzzy logic based position estimation for sensorless switched reluctance motor drives," *IEEE transactions on power electronics*, vol. 15, no. 2, pp. 319-334, 2000.
[174] N. Zabihi and R. Gouws, "A review on switched reluctance machines for electric vehicles," in *2016 IEEE 25th International Symposium on Industrial Electronics (ISIE)*, 2016: IEEE, pp. 799-804.
[175] A. Chiba and K. Kiyota, "Review of research and development of switched reluctance motor for hybrid electrical vehicle," in *2015 IEEE Workshop on Electrical Machines Design, Control and Diagnosis (WEMDCD)*, 2015: IEEE, pp. 127-131.
[176] B. Burkhart, A. Klein-Hessling, I. Ralev, C. P. Weiss, and R. W. De Doncker, "Technology, research and applications of switched reluctance drives," *CPSS Transactions on Power Electronics and Applications*, vol. 2, no. 1, pp. 12-27, 2017.
[177] J. Rosero, J. Ortega, E. Aldabas, and L. Romeral, "Moving towards a more electric aircraft," *IEEE Aerospace and Electronic Systems Magazine*, vol. 22, no. 3, pp. 3-9, 2007.
[178] N. Dankadai, S. Mcdonald, M. Elgendy, D. Atkinson, S. Ullah, and G. Atkinson, "Direct instantaneous torque control of switched reluctance motor for aerospace applications," in *2018 53rd International Universities Power Engineering Conference (UPEC)*, 2018: IEEE, pp. 1-6.
[179] B. Sarlioglu and C. T. Morris, "More electric aircraft: Review, challenges, and opportunities for commercial transport aircraft," *IEEE transactions on Transportation Electrification*, vol. 1, no. 1, pp. 54-64, 2015.
[180] J. S. Cloyd, "A status of the United States Air Force's more electric aircraft initiative," in *IECEC-97 Proceedings of the Thirty-Second Intersociety Energy Conversion Engineering Conference (Cat. No. 97CH6203)*, 1997, vol. 1: IEEE, pp. 681-686.
[181] W. Cao, B. C. Mecrow, G. J. Atkinson, J. W. Bennett, and D. J. Atkinson, "Overview of electric motor technologies used for more electric aircraft (MEA)," *IEEE transactions on industrial electronics*, vol. 59, no. 9, pp. 3523-3531, 2011.
[182] A. Boglietti, A. Cavagnino, A. Tenconi, S. Vaschetto, and P. di Torino, "The safety critical electric machines and drives in the more electric aircraft: A survey," in *2009 35th Annual Conference of IEEE Industrial Electronics*, 2009: IEEE, pp. 2587-2594.

[183] R. Naayagi, "A review of more electric aircraft technology," in *2013 international conference on energy efficient technologies for sustainability*, 2013: IEEE, pp. 750-753.
[184] R. Krishnan, D. Blanding, A. Bhanot, A. Staley, and N. Lobo, "High reliability SRM drive system for aerospace applications," in *IECON'03. 29th Annual Conference of the IEEE Industrial Electronics Society (IEEE Cat. No. 03CH37468)*, 2003, vol. 2: IEEE, pp. 1110-1115.
[185] R. Cardenas, W. Ray, and G. Asher, "Switched reluctance generators for wind energy applications," in *Proceedings of PESC'95-Power Electronics Specialist Conference*, 1995, vol. 1: IEEE, pp. 559-564.
[186] R. Cardenas, R. Pena, M. Perez, J. Clare, G. Asher, and P. Wheeler, "Control of a switched reluctance generator for variable-speed wind energy applications," *IEEE transactions on Energy conversion*, vol. 20, no. 4, pp. 781-791, 2005.
[187] E. Echenique, J. Dixon, R. Cárdenas, and R. Peña, "Sensorless control for a switched reluctance wind generator, based on current slopes and neural networks," *IEEE Transactions on Industrial Electronics*, vol. 56, no. 3, pp. 817-825, 2008.
[188] Y. Bao, K. Cheng, X. Xue, J. Chan, Z. Zhang, and J. Lin, "Research on a novel switched reluctance generator for wind power generation," in *2011 4th International Conference on Power Electronics Systems and Applications*, 2011: IEEE, pp. 1-6.
[189] X. Xue, K. Cheng, Y. Bao, and J. Leung, "Design consideration of C-core switched reluctance generators for wind energy," in *2011 4th International Conference on Power Electronics Systems and Applications*, 2011: IEEE, pp. 1-6.
[190] S. Méndez, A. Martínez, W. Millán, C. E. Montaño, and F. Pérez-Cebolla, "Design, characterization, and validation of a 1-kW AC self-excited switched reluctance generator," *IEEE Transactions on Industrial Electronics*, vol. 61, no. 2, pp. 846-855, 2013.
[191] C. Zwyssig, J. W. Kolar, and S. D. Round, "Megaspeed drive systems: Pushing beyond 1 million r/min," *IEEE/ASME Transactions on mechatronics*, vol. 14, no. 5, pp. 564-574, 2009.
[192] N. Bianchi, S. Bolognani, and F. Luise, "Potentials and limits of high-speed PM motors," *IEEE Transactions on Industry Applications*, vol. 40, no. 6, pp. 1570-1578, 2004.
[193] M. A. Rahman, A. Chiba, and T. Fukao, "Super high speed electrical machines-summary," in *IEEE Power Engineering Society General Meeting, 2004.*, 2004: IEEE, pp. 1272-1275.
[194] M. A. Awadallah and B. Venkatesh, "Energy storage in flywheels: An overview," *Canadian Journal of Electrical and Computer Engineering*, vol. 38, no. 2, pp. 183-193, 2015.
[195] W. Gruber, T. Hinterdorfer, H. Sima, A. Schulz, and J. Wassermann, "Comparison of different motor-generator sets for long term storage flywheels," in *2014 International Symposium on Power Electronics, Electrical Drives, Automation and Motion*, 2014: IEEE, pp. 161-166.
[196] S. Ullah, "A magnet assisted segmental rotor switched reluctance machine suitable for fault tolerant aerospace applications," Newcastle University, 2016.
[197] R. Krishnan, *Switched reluctance motor drives: modeling, simulation, analysis, design, and applications*. CRC press, 2017.
[198] S. S. Ahmad and G. Narayanan, "Linearized modeling of switched reluctance motor for closed-loop current control," *IEEE Transactions on Industry Applications*, vol. 52, no. 4, pp. 3146-3158, 2016.

[199] A. Anuchin, D. Grishchuk, A. Zharkov, Y. Prudnikova, and L. Gosteva, "Real-time model of switched reluctance drive for educational purposes," in *2016 57th International Scientific Conference on Power and Electrical Engineering of Riga Technical University (RTUCON)*, 2016: IEEE, pp. 1-5.

[200] P. Chancharoensook, "Direct instantaneous torque control of a four-phase switched reluctance motor," in *2009 International Conference on Power Electronics and Drive Systems (PEDS)*, 2009: IEEE, pp. 770-777.

[201] B. Fahimi, G. Suresh, J. Mahdavi, and M. Ehsami, "A new approach to model switched reluctance motor drive application to dynamic performance prediction, control and design," in *PESC 98 Record. 29th Annual IEEE Power Electronics Specialists Conference (Cat. No. 98CH36196)*, 1998, vol. 2: IEEE, pp. 2097-2102.

[202] W. Lu, A. Keyhani, and A. Fardoun, "Neural network-based modeling and parameter identification of switched reluctance motors," *IEEE transactions on energy conversion*, vol. 18, no. 2, pp. 284-290, 2003.

[203] I. Mosoń, K. Iwan, and J. Nieznański, "Circuit-oriented model of the switched reluctance motor for drive systems simulation, 28th IECON Conf., 5-8 Nov. 2002," *Sevilla, Spain*, pp. 497-501.

[204] N. J. Nagel and R. D. Lorenz, "Modeling of a saturated switched reluctance motor using an operating point analysis and the unsaturated torque equation," *IEEE transactions on industry applications*, vol. 36, no. 3, pp. 714-722, 2000.

[205] B. C. Mecrow, C. Weiner, and A. C. Clothier, "The modeling of switched reluctance machines with magnetically coupled windings," *IEEE Transactions on Industry Applications*, vol. 37, no. 6, pp. 1675-1683, 2001.

[206] S. Mir, I. Husain, and M. E. Elbuluk, "Switched reluctance motor modeling with on-line parameter identification," *IEEE Transactions on Industry Applications*, vol. 34, no. 4, pp. 776-783, 1998.

[207] N. Dankadai, M. Elgendy, S. Mcdonald, D. Atkinson, and G. Atkinson, "Assessment of Sliding Mode Observer in Sensorless Control of Switched Reluctance Motors," in *2019 IEEE 13th International Conference on Power Electronics and Drive Systems (PEDS)*, 2019: IEEE, pp. 1-6.

[208] S. J. Fedigan and C. P. Cole, "A variable-speed sensorless drive system for switched reluctance motors," *Texas Instruments Application Report*, 1999.

[209] A. Xu, W. Zhang, and P. Ren, "Comparison of torque ripple reduction for switched reluctance motor based on DTC and DITC," in *2018 13th IEEE Conference on Industrial Electronics and Applications (ICIEA)*, 2018: IEEE, pp. 1727-1732.

[210] S. Pratapgiri, "Comparative analysis of hysteresis current control and direct instantaneous torque control of switched reluctance motor," in *2016 International Conference on Electrical, Electronics, and Optimization Techniques (ICEEOT)*, 2016: IEEE, pp. 2856-2860.

[211] M. R. Lyu, "Software reliability: to use or not to use?," in *Proceedings of 1994 IEEE International Symposium on Software Reliability Engineering*, 1994: IEEE, pp. 66-73.

[212] A. Yadav and R. Khan, "Bridging the gap between design constructs and reliability factors," *Executive Committee*, p. 201029, 2010.

[213] N. Sharygina, J. C. Browne, and R. P. Kurshan, "A formal object-oriented analysis for software reliability: Design for verification," in *International Conference on Fundamental Approaches to Software Engineering*, 2001: Springer, pp. 318-332.

[214] K. Goseva-Popstojanova and K. S. Trivedi, "Failure correlation in software reliability models," *IEEE Transactions on Reliability*, vol. 49, no. 1, pp. 37-48, 2000.

[215] S. Henry and D. Kafura, "Software structure metrics based on information flow," *IEEE transactions on Software Engineering*, no. 5, pp. 510-518, 1981.
[216] N. Fenton and J. Bieman, *Software metrics: a rigorous and practical approach*. CRC press, 2014.
[217] S. M. Henry, "Information flow metrics for the evaluation of operating systems' structure," 1979.
[218] Y. Shi and S. Xu, "A new method for measurement and reduction of software complexity," *Tsinghua Science and Technology*, vol. 12, no. S1, pp. 212-216, 2007.
[219] Y. Chu and S. Xu, "Exploration of complexity in software reliability," *Tsinghua Science and Technology*, vol. 12, no. S1, pp. 266-269, 2007.
[220] L. Belady and C. Evangelisti, "System partitioning and measuring," *IBM Res. Rep. RC7560*, vol. 1979, pp. 120-131, 1979.
[221] C. Gan, J. Wu, Q. Sun, S. Yang, Y. Hu, and L. Jin, "Low-cost direct instantaneous torque control for switched reluctance motors with bus current detection under soft-chopping mode," *IET Power Electronics*, vol. 9, no. 3, pp. 482-490, 2016.
[222] J. Liang, D.-H. Lee, and J.-W. Ahn, "Direct instantaneous torque control of switched reluctance machines using 4-level converters," *IET electric power applications*, vol. 3, no. 4, pp. 313-323, 2009.
[223] W. Shang, S. Zhao, Y. Shen, and Z. Qi, "A sliding mode flux-linkage controller with integral compensation for switched reluctance motor," *IEEE Transactions on Magnetics*, vol. 45, no. 9, pp. 3322-3328, 2009.
[224] J. Ye, P. Malysz, and A. Emadi, "A fixed-switching-frequency integral sliding mode current controller for switched reluctance motor drives," *IEEE Journal of Emerging and Selected Topics in Power Electronics*, vol. 3, no. 2, pp. 381-394, 2014.
[225] P. Leśniewski, "Discrete time reaching law based sliding mode control: a survey," in *2018 22nd International Conference on System Theory, Control and Computing (ICSTCC)*, 2018: IEEE, pp. 734-739.
[226] W. Gao, Y. Wang, and A. Homaifa, "Discrete-time variable structure control systems," *IEEE transactions on Industrial Electronics*, vol. 42, no. 2, pp. 117-122, 1995.
[227] A. Bartoszewicz, "Discrete-time quasi-sliding-mode control strategies," *IEEE Transactions on Industrial Electronics*, vol. 45, no. 4, pp. 633-637, 1998.
[228] A. Bartoszewicz and P. Leśniewski, "New switching and nonswitching type reaching laws for SMC of discrete time systems," *IEEE Transactions on Control Systems Technology*, vol. 24, no. 2, pp. 670-677, 2015.
[229] S. Wang, Z. Hu, and X. Cui, "Research on Novel Direct Instantaneous Torque Control Strategy for Switched Reluctance Motor," *IEEE Access*, vol. 8, pp. 66910-66916, 2020.
[230] C. Gan, J. Wu, S. Yang, and Y. Hu, "Phase current reconstruction of switched reluctance motors from dc-link current under double high-frequency pulses injection," *IEEE Transactions on Industrial Electronics*, vol. 62, no. 5, pp. 3265-3276, 2014.
[231] M. S. Islam, I. Husain, R. J. Veillette, and C. Batur, "Design and performance analysis of sliding-mode observers for sensorless operation of switched reluctance motors," *IEEE Transactions on Control systems technology*, vol. 11, no. 3, pp. 383-389, 2003.

APPENDIX A

Matlab code for curve fitting inductance profile of MASRM

The Matlab code for curve fitting inductance profile of MASRM is presented below. It is used to curve fit the coefficients $A_n(i)$ in the Fourier series can be obtained using the inductances at different specific rotor positions which is a function of phase current. It is also used to plot the curve fitted profile of these four coefficients that were generated as polynomial functions from inductance profiles of the MASRM are shown in Figure 3.7.

```
fontSize = 16;

syms theta I;

R = 3.8;

% Generate the sample data.

L0Deg_0 =   [1.97E-01   1.97E-01    1.97E-01    1.96E-01    1.95E-01    1.94E-
01    1.93E-01    1.82E-01    1.70E-01    1.53E-01    1.30E-01    1.05E-01
8.26E-02    6.66E-02    5.38E-02    4.33E-02]

L60Deg_15 =      [1.60E-01    1.60E-01     1.60E-01     1.53E-01     1.49E-01
1.41E-01    1.27E-01    1.15E-01    1.05E-01    9.69E-02    8.83E-02    7.82E-
02    6.75E-02    5.80E-02    4.93E-02    4.25E-02]

L120Deg_30 =     [6.99E-02    7.03E-02     7.03E-02     6.98E-02     6.93E-02
6.82E-02    6.70E-02    6.58E-02    6.44E-02    6.25E-02    6.00E-02    5.62E-
02    5.16E-02    4.66E-02    4.25E-02    3.94E-02]

L180Deg_45 =     [5.35E-02    5.39E-02     5.38E-02     5.37E-02     5.35E-02
5.33E-02    5.31E-02    5.28E-02    5.25E-02    5.19E-02    5.06E-02    4.84E-
02    4.52E-02    4.21E-02    3.96E-02    3.77E-02]

I0  =      [0.182639967,     0.365227376,      0.547814785,      0.73220149,
0.922446521,    1.112691553,    1.302936584,    1.577271496,    1.902881759,
2.355756891,     3.035911306,     4.122815649,     5.65947248   7.559904104
10.02314627 13.27613252]

I60  =     [0.224676129,     0.449287602,      0.673899076,      0.937436669,
1.203483289,    1.532169144,    1.974508714,    2.493680382,    3.06951186,
3.711012078,       4.47900398,  5.51984341,  6.929009629,       8.675574577,
10.93409771,    13.54389958]

I120  =    [0.514501412,      1.02322177,  1.534986113,        2.060217267,
2.596502749,    3.162611928,    3.754577313,    4.372220898,    5.028334453,
```

```
5.750532817,    6.594983184,    7.674019074,    9.063082183,    10.79519327,
12.70343789,    14.61168251]

I180  =   [0.671768716,    1.334685501,      2.003500754,      2.680987804,
3.363012468,    4.050061539,    4.741893988,    5.443975614,    6.167352432,
6.932438872,     7.81505584,  8.920158858,     10.33592952,     11.97222547,
13.60852143,    15.24481738]



% Find the coefficients.

coeffsL0Deg_0 = polyfit(I0, L0Deg_0, 6);

x1 = linspace(0,15);

% y1 = 1./(1+x1);

 f1 = polyval(coeffsL0Deg_0,x1);

 plot(I0, L0Deg_0, 'ro', 'MarkerSize', 10);

 hold on

 plot(x1,f1,'r--')


% %

coeffsL60Deg_15 = polyfit(I60, L60Deg_15, 6);

 x1 = linspace(0,15);

% y1 = 1./(1+x1);

 f1 = polyval(coeffsL60Deg_15,x1);

 plot(I60, L60Deg_15, 'ro', 'MarkerSize', 10);

 hold on

 plot(x1,f1,'r--')


%

coeffsL120Deg_30 = polyfit(I120, L120Deg_30, 6);

 x1 = linspace(0,15);

% y1 = 1./(1+x1);

 f1 = polyval(coeffsL120Deg_30,x1);

 plot(I120, L120Deg_30, 'ro', 'MarkerSize', 10);
```

```
 hold on

 plot(x1,f1,'r--')


%

coeffsL180Deg_45 = polyfit(I180, L180Deg_45, 6);

x1 = linspace(0,15);

% y1 = 1./(1+x1);

 f1 = polyval(coeffsL180Deg_45,x1);

 plot(I180, L180Deg_45, 'ro', 'MarkerSize', 10);

 hold on

 plot(x1,f1,'r--')


set(gcf, 'units','normalized','outerposition',[0 0 1 1]);


% % % Four terms of the Inductance fourier series model

% Fourier series  coefficient (magnitude of the nth harmonic)

A0=1/3*(1/2*(coeffsL0Deg_0    +    coeffsL180Deg_45)+(coeffsL60Deg_15    +
coeffsL120Deg_30));

A1=1/3*(coeffsL0Deg_0    +    coeffsL60Deg_15    -    coeffsL120Deg_30    -
coeffsL180Deg_45);

A2=1/3*(coeffsL0Deg_0    -    coeffsL60Deg_15    -    coeffsL120Deg_30    +
coeffsL180Deg_45);

A3=1/3*(1/2*(coeffsL0Deg_0    -    coeffsL180Deg_45)-(coeffsL60Deg_15    -
coeffsL120Deg_30));


% iL = inv(L)

L0 = A0 + A1 +A2 +A3;

L15    =       A0    +    A1*cos(deg2rad(4*15))    +    A2*cos(deg2rad(8*15))
+A3*cos(deg2rad(12*15));

L30    =       A0    +    A1*cos(deg2rad(4*30))    +    A2*cos(deg2rad(8*30))
+A3*cos(deg2rad(12*30));

L45    =       A0    +    A1*cos(deg2rad(4*45))    +    A2*cos(deg2rad(8*45))
+A3*cos(deg2rad(12*45));
```

```
% % % % %

DelA0 = polyder(A0);

DelA1 = polyder(A1);

DelA2 = polyder(A2);

DelA3 = polyder(A3);


L_THETA_I = A0 + A1*cos(4*theta) + A2*cos(8*theta) + A3*cos(12*theta);

Del_L_theta = -A1*sin(4*theta) - A2*sin(8*theta) - A3*sin(12*theta);

Del_L_I    =    DelA0    +    DelA1*cos(4*theta)    +    DelA2*cos(8*theta)    +
DelA3*cos(12*theta);

% V = R*I + L_THETA_I*Del_I + I*(Del_L_theta*Del_theta +Del_L_I*Del_I)


IntA0_I = polyint([A0,0]);

IntA1_I = polyint([A1,0]);

IntA2_I = polyint([A2,0]);

IntA3_I = polyint([A3,0]);


T     =     -4*sin(4*theta)*IntA1_I     -     8*sin(8*theta)*IntA2_I     -
12*sin(12*theta)*IntA3_I;
```

APPENDIX B

General Control Board

This appendix describes the general control board used in this project which is based on the Texas Instrument F28377D microcontroller. The functions included on the board are shown in Figure B1.

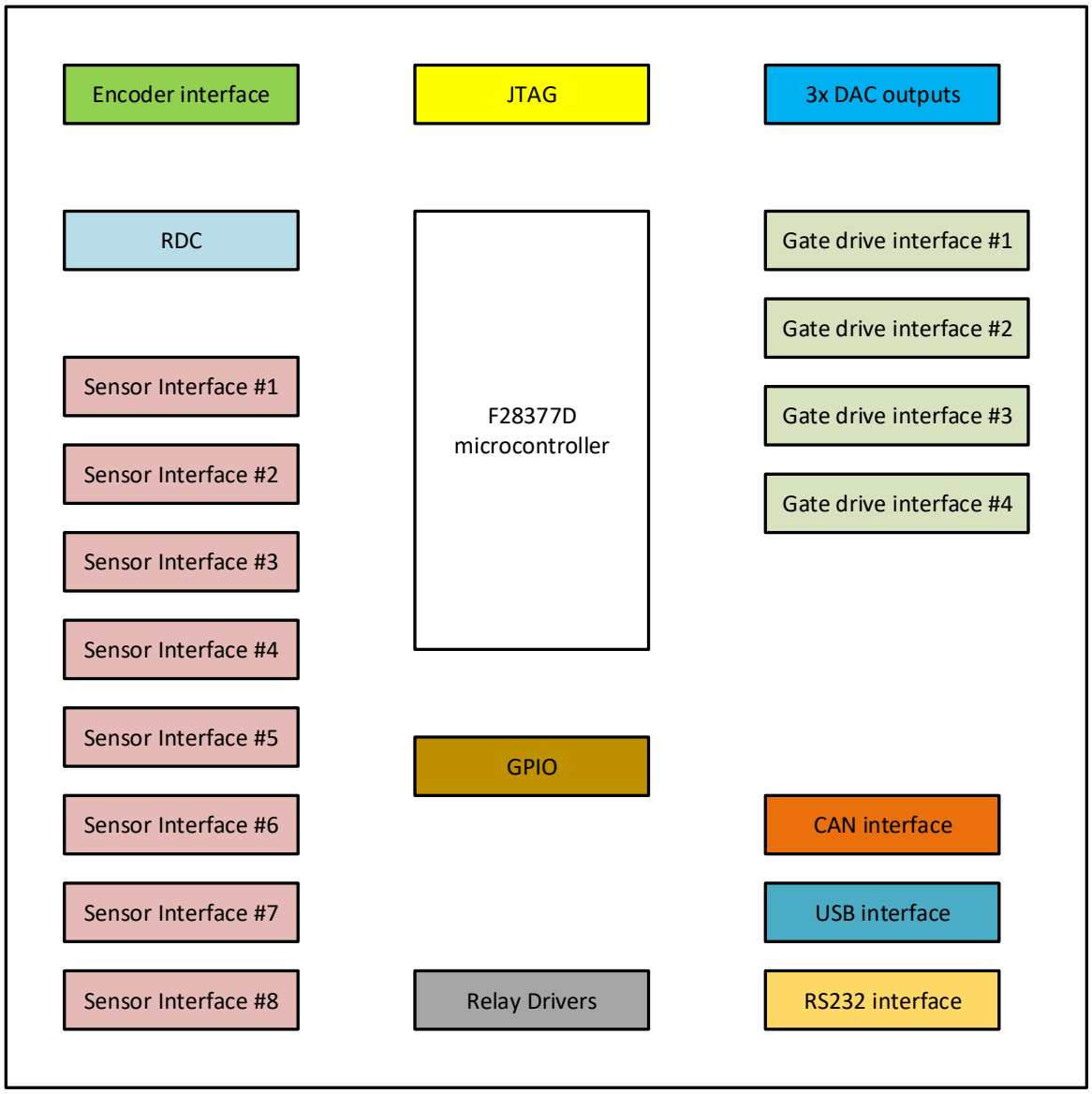

FigureB1: Sub-circuits for GCB

The simplified layout of the proposed multilayer gate drive board with indicative locations for the various major devices is provided in Figure B2.

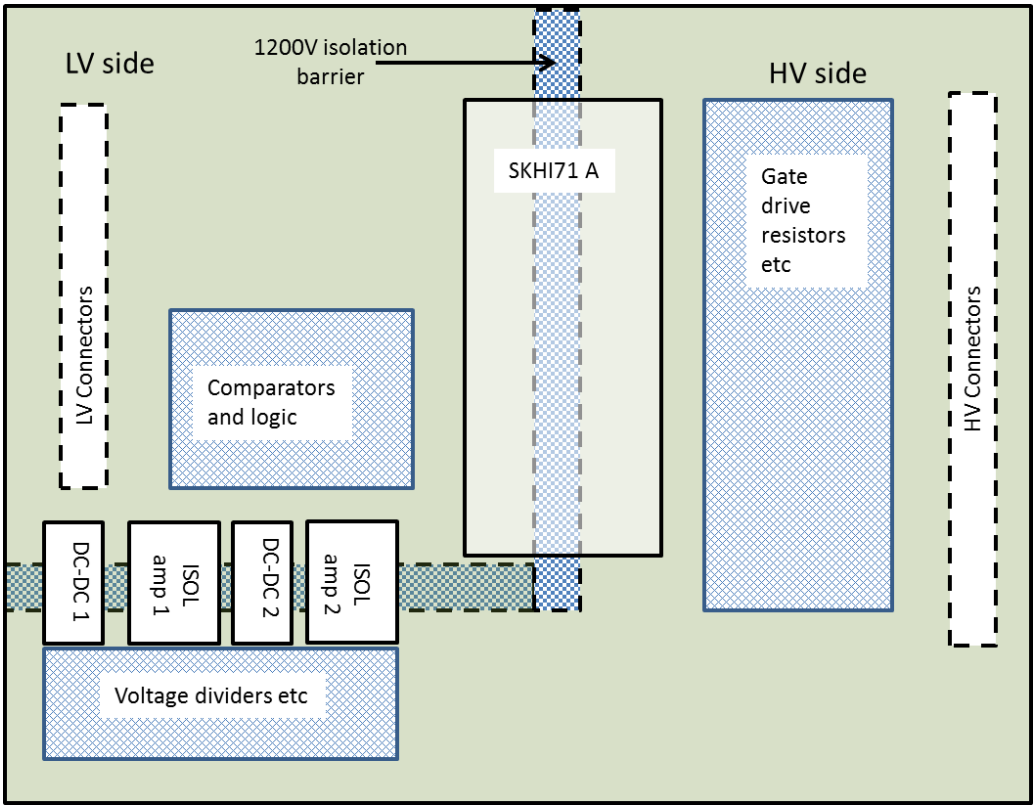

Figure B2: General layout of proposed gate drive PCB

The primary functions of proposed bespoke gate driver PCB board are as follows:

- Local adaptation of GCB power supplies for isolated signal processing (voltage sense and thermistor sense circuits)
- Take in gate drive signals from the GCB and deliver to IGBT's via the SKHI71 units
- Interface Gate driver (SKHI71) status and control back to the GCB
- Monitor the DC link voltage and provide an adjustable threshold for a hysteresis chopper signal to a dynamic braking chopper IGBT via the SKHI71 BRK device gate drive channel.
- Monitor the device thermistor and produce an analogue representation of temperature and an adjustable over temperature trip signal to the GCB.

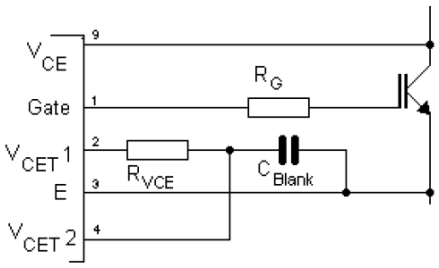

Figure 7.8: Gate output connections

Gate resistors

The IGBT's on the input bridge and the output bridge in the 24ACC12T4V10 Skiip unit are not the same. For the input devices (1-6) we required RG = 30 Ohm and for the output devices (7-12) we require 24 Ohm. In both cases this should give a rise time of around 35ns. Taking into account the anticipated losses and the need to provide flexibility for other device users, using two 0.4Watt resistors in parallel is recommended. i.e 2 X 62 Ohm 0.4W for devices 1-6 and 2 X 51 Ohm for devices 7-12.

Voltage detection and overvoltage trip

The DC link voltage sensing circuit comprises a 4.99MOhm resistor and a 10kOhm resistor chain. The isolation amplifier is rated for 0-2V input. Thus, this chain will work for a DC link up to 1000V (anything higher than this is protected by the zener across the input to the isolation amplifier). The output signal is fed through the isolation amplifier to a comparator and minimum pulse generator to trigger the BRK device. A second similar circuit fed from the same isolation amplifier is set to a higher voltage threshold to detect an overvoltage fault and disable the IGBT's

Temperature detection, analogue output and over temperature trip

The on-board thermistor unit within the SKIIP is isolated in case of internal failures linking the thermistor to an IGBT. Most of the circuit is similar to the DC link voltage sensing circuit above with the exception that an isolated voltage source is provided by the Gate drive board to create a voltage drop across the thermistor for sensing purposes.

APPENDIX C

software description of F28377D general control board

Appendix C gives the software description of F28377D general control board. Each project contains a number of source files most of which are unmodified or slightly modified versions of that available from TI example files. The majority of code written for this application is contained in the following source files.

Project: GCB_cpu01

run_cpu1.c (CPU1)

testCla1.cla (CPU1.CLA)

In project GCB_cpu01, CPU1.CLA is used for torque control and its code includes a AQMC. This AQSMC makes use of look-up tables for torque estimation, and conduction angle optimization. The setting up of these look-up tables is done by CPU1 code. The RAM used for the look-up tables is first made accessible to CPU1 during the set up and then access is transferred to CPU1.CLA.

Basically, the functions performed by the various processing elements are:

CPU1: GUI data exchange, data recording, peripheral interfacing

CPU1.CLA: torque control code, peripheral interfacing

In File: run_cpu1.c, A number of #define statements are included to set various parameters such as the converter switching frequency, dead-time etc.

A list of #pragma directives follow which associate several variables to the CPU1/CPU1.CLA message RAM and the CPU1.CLA data RAM blocks.

It was decided to pack flag bits into a single byte for transfer to and from the GUI. This makes more efficient use of the serial message payload. A union/struct type is defined for this and TXflagReg and RXflagReg are defined for transferring the flag bits in either direction.

After execution of various initialisation functions there is an endless loop. This loop flashes an LED on the GCB to confirm that code is running on CPU1. The variable LoopCount is updated inside the loop to act as a loop counter.

F28377D comparator trip logic for fault detection

The F28377D microcontroller contains on-chip hardware to allow the implementation of fast converter protection. A number of analogue input pins are connected to an analogue comparator system in addition to an ADC input. In this project, the comparator system is used to monitor the current sensors, voltage sensors and temperature sensors output which is used to trip-off the PWM outputs in the event of an over-value conditions.

Details of the comparator sub-systems can be seen in Figure C1. Each comparator sub-system contains two 12-bit digital to analogue converters DACs (DACH and DACL) which are used to hold the upper and lower pre-set threshold voltages corresponding to the upper and lower current trip levels. An optional digital filter is available to remove noise from the comparator outputs. In order to implement a bipolar overcurrent detection the pair of comparators are operated as a "window detector" requiring that the lower threshold comparator output is inverted before both outputs are OR'd together.

Considering Figure C1, it can be seen that individual comparator output signals (e.g. CMPSS6.CTRIPH and CMPSS6.CTRIPL) are fed into the EPWM X-bar sub-system. The EPWM X-bar subsystem is a flexible arrangement for connecting various trip signals to the EPWM sub-system. In this case, the output signals from 3 comparator sub-systems are fed as inputs to the EPWM X-bar sub-system. An option within the EPWM X-bar configuration is to OR together the two comparator signals to form one trip signal (e.g. TRIP4 for Comparator Subsystem 6). The other two comparator subsystems correspondingly produce TRIP5 and TRIP7.

In this project it is desired that any comparator trip condition causes all EPWM outputs to turn off. It is therefore necessary to feed all trip signals into each EPWM sub-system. Each EPWM sub-system contains a Digital Compare (DC) sub-system which propagates trip signals to the Trip Zone (TZ) sub-system. The DC sub-system is very flexible but is currently configured to simply OR the 3 trip signals together to form a common trip signal DCAH. As configured this signal directly drives DCAEVT1 which in turn directly drives DCAEVT1.force. To clear the

trip condition the flip-flop must be reset by software by setting the TZCLR[OSHT] bit. It is also possible to force a trip from software by setting the TZFRC[OSHT] bit.

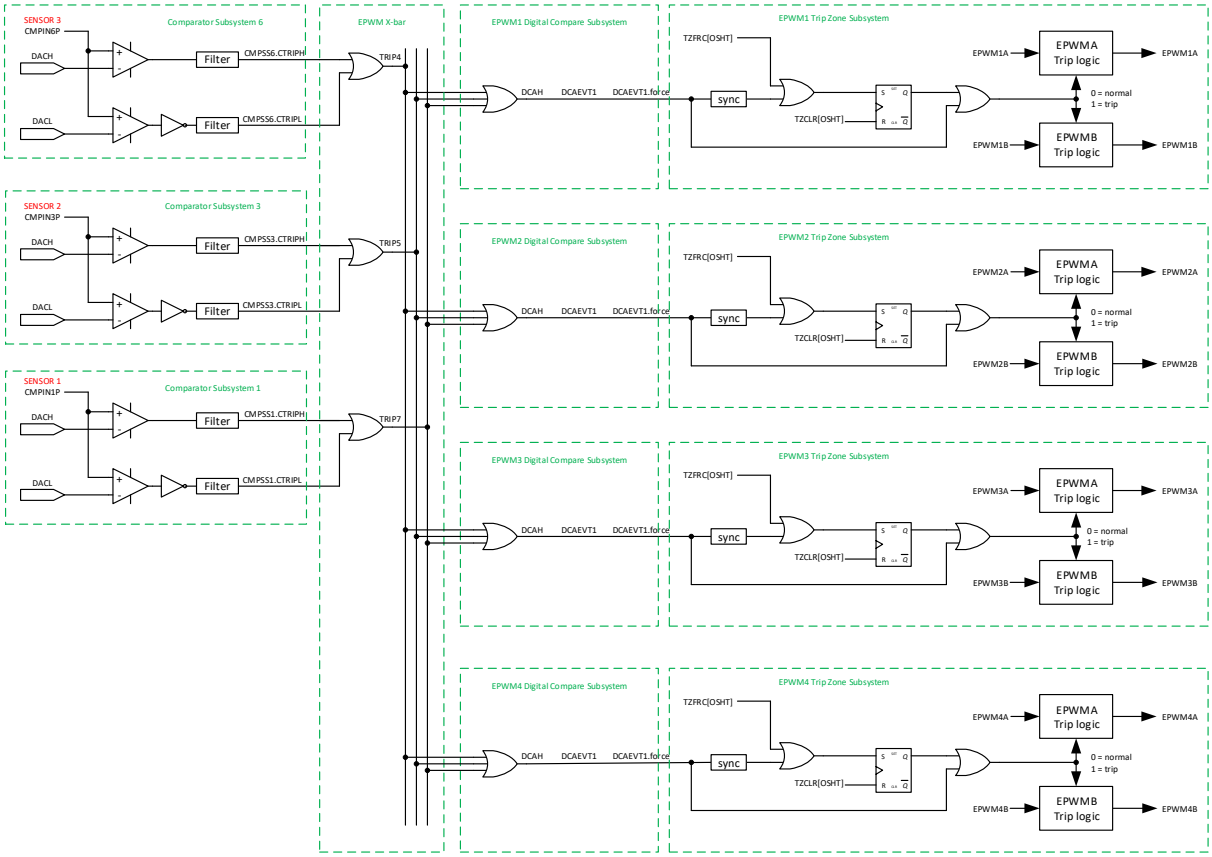

Figure C1: Comparator sub-systems of the F28377D microcontroller

GUI for interacting with MASRM drive

The graphical user interface (GUI) for interacting with the F28377D GCB target boards hence the MASRM drive in writing in MATLAB and it is shown in Figure C2. If necessary, refer to MATLAB's documentation on creating GUIs.

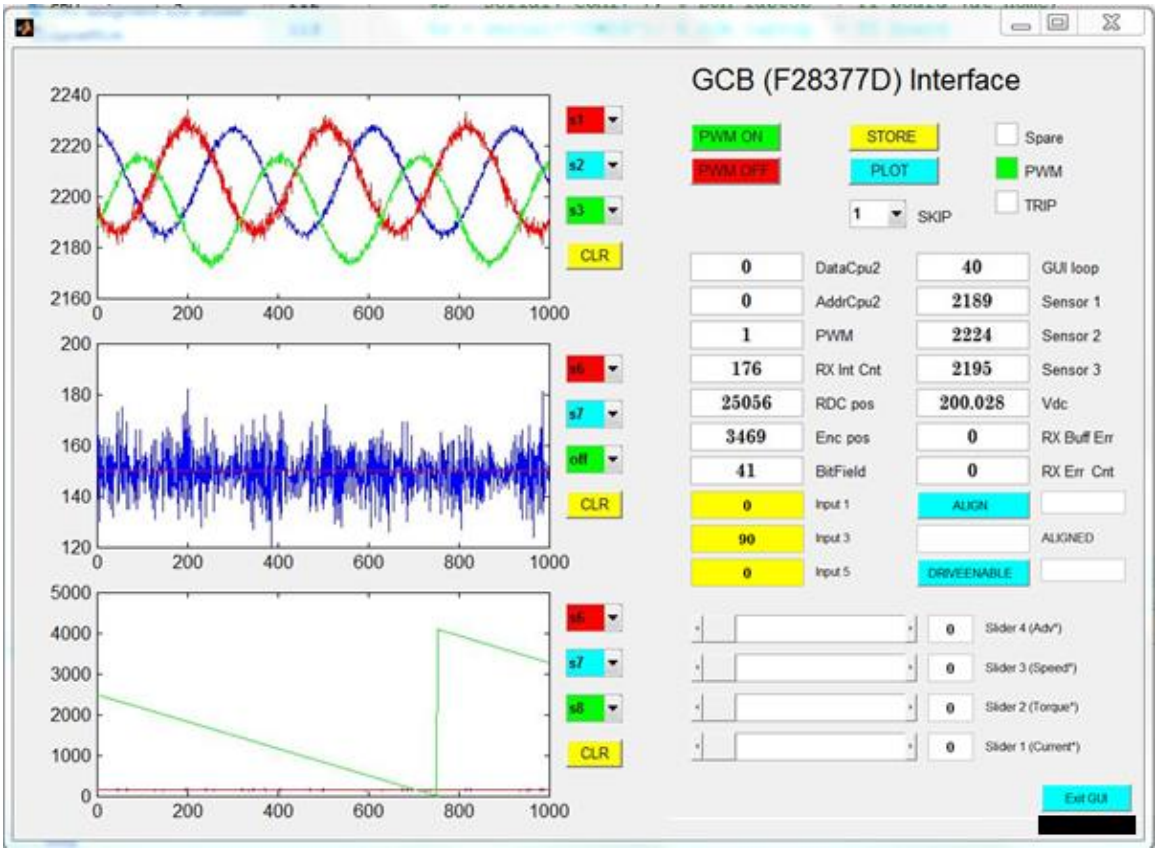

Figure C2: Example of GUI appearance